

University of Alberta

Library Release Form

Name of Author: Carlos A. Santamaria

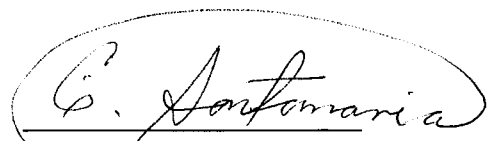
Title of Thesis: Circumferential Buckling of Polymer Pipes Under Earth
and Fluid Pressures

Degree: Master of Science

Year this Degree Granted: 2003

Permission is hereby granted to the University of Alberta Library to reproduce single copies of this thesis and to lend or sell such copies for private, scholarly or scientific research purposes only.

The author reserves all other publication and other rights in association with the copyright in the thesis, and except as herein before provided, neither the thesis nor any substantial portion thereof may be printed or otherwise reproduced in any material form whatever without the author's prior written permission.

A handwritten signature in cursive script that reads "C. Santamaria". The signature is enclosed within a hand-drawn oval shape.

6-4383 El Dorado

Panama, Panama

November 29

University of Alberta

Circumferential Buckling of Polymer Pipes Under Earth and Fluid
Pressures

by

Carlos A. Santamaria

A thesis submitted to the Faculty of Graduate Studies and Research in
partial fulfillment of the requirements for the degree of Master of Science

in

Geotechnical Engineering

Department of Civil & Environmental Engineering

Edmonton, Alberta

Spring 2003

University of Alberta

Faculty of Graduate Studies and Research

The undersigned certify that they have read, and recommend to the Faculty of Graduate Studies and Research for acceptance, a thesis entitled **Circumferential Buckling of Polymer Pipes Under Earth and Fluid Pressures** submitted by **Carlos A. Santamaria R.** in partial fulfillment of the requirements for the degree of Master of Science in **Geotechnical Engineering**.


Richard Brachman


Derek Martin


Dave Sego


Ken Fyfe

November 22, 2002
Date

To my family Miriam, Carlos & Andrea

Thanks

ABSTRACT

The ultimate limit state of circumferential buckling of plastic manholes or pipes under ground and fluid loads was previously unknown. A new test facility was constructed and experimental procedures were developed to test high-density polyethylene (HDPE) pipes under external ground and fluid pressures up to circumferential buckling failure.

Results from six experiments conducted with ground and fluid loads applied in the radial direction are reported. The observations and recorded data included applied earth and fluid pressures, radial deflections of the pipe and images of the buckled shape of the pipe. The results showed that as fluid pressures were increased, the effective stresses acting on the pipe decreased. Buckling of the pipe occurred essentially with only fluid pressures and very little soil support, even with very high magnitudes of effective stresses applied at the external boundaries of the soil.

ACKNOWLEDGEMENTS

My first words of gratitude are for my family. Thanks to my parents Miriam and Carlos for their support. They made possible the successful completion of this stage in my career.

I also want to express my special gratitude to my supervisor Dr. Richard Brachman. His support and encouragement during these two years of my life were essential to accomplish this work successfully.

Sincere words of appreciation are for Gerry Cyre and Steve Gamble. Their ideas and unfailing help during my experiments were invaluable. My appreciation is also extended to Christine Hereygers for her assistance whenever it was needed.

Finally, a special gratitude to the Canadian Foundation for the Innovation and the Natural Sciences and Engineering Research Council of Canada for providing the funding needed for this project.

TABLE OF CONTENTS

Chapter 1 – Introduction

1.1 Description of the problem.....	1
1.2 Current state of practice.....	2
1.3 Objectives and methodology.....	3
1.4 Organization of the thesis.....	4

Chapter 2 – Literature review

2.1 Introduction.....	9
2.2 Arching.....	9
2.2.1 Mechanism of arching.....	9
2.2.2 Neutral arching.....	10
2.2.3 Positive and negative arching.....	11
2.2.4 Arching solution.....	12
2.3 Pipe thrust.....	14
2.4 Review of circumferential buckling solutions.....	14
2.4.1 Buckling of unsupported pipes under uniform external pressure.....	15
2.4.2 Buckling of soil surrounded pipes.....	15
2.4.2.1 Linear multiwave theories.....	15
2.4.2.2 Single wave solutions.....	17
2.5 Applicability of the buckling solutions.....	19

2.5.1 Single wave and multiwave theories.....	19
2.5.2 Winkler model and elastic continuum.....	20
2.6 Evaluation of the current design formula for combined loads.....	21
2.7 Previous buckling tests with ground and fluid loads.....	22
2.8 Summary.....	23
 Chapter 3 – Test concept and development of the test cell	
3.1 Introduction.....	31
3.2 The test concept.....	31
3.3 Applied pressures.....	32
3.3.1 Earth loads.....	32
3.3.2 Fluid loads.....	33
3.4 Pipe end conditions.....	33
3.4.1 Unrestrained radial deformations.....	35
3.4.1.1 Seal configurations tested.....	35
3.4.2 Restrained radial deformations.....	37
3.4.3 Effect of restraints in the axial direction.....	38
3.4.4 Summary.....	39
3.5 Test cell description.....	39
3.6 Test cell design.....	40
3.6.1 Test cell internal diameter.....	40
3.6.2 Test cell internal vertical clearance.....	41

3.6.3 Pressure requirements based on available buckling solutions.....	41
3.7 Summary.....	42
Chapter 4 – Methodology	
4.1 Introduction.....	53
4.2 Materials used.....	53
4.2.1 Pipe specimens.....	53
4.2.2 Geotextile.....	54
4.2.3 Gravel backfill.....	54
4.2.4 Sand.....	54
4.2.5 Rubber bladder.....	56
4.3 Instrumentation used in the test program.....	56
4.3.1 Linear potentiometers.....	56
4.3.2 Infrared camera.....	56
4.3.3 Pressure transducers.....	57
4.4 Experimental procedure.....	57
4.5 Application of bladder and pore pressure.....	61
4.6 Load path.....	61
4.7 Summary.....	62
Chapter 5 – Results	
5.1 Presentation of laboratory results.....	77
5.2 Applied pressures and measured pipe deflections.....	77

5.2.1 Results from test T1.....	78
5.2.2 Results from test T2.....	79
5.2.3 Results from test T3.....	81
5.2.4 Results from test T4.....	82
5.2.5 Results from test T5.....	83
5.2.6 Results from test T6.....	84
5.3 Summary of results.....	86
5.4 Visual observations from the infrared camera.....	87
5.4.1 Sequence of buckling images for test T1.....	87
5.4.2 Sequence of buckling images for test T2.....	88
5.4.3 Sequence of buckling images for test T3.....	89
5.4.4 Sequence of buckling images for test T4.....	89
5.4.5 Sequence of buckling images for test T5.....	90
5.4.6 Sequence of buckling images for test T6.....	90
5.5 Summary of the visual observations.....	91
Chapter 6 – Discussion	
6.1 Introduction.....	128
6.2 Contact pressures.....	129
6.2.1 First stage of the tests: Application of bladder pressure with zero fluid pressure.....	129
6.2.2 Second stage of the tests: Simultaneous application of bladder and fluid pressure.....	130

6.2.3 Pipe modulus.....	131
6.3 Interpretation of soil-structure interaction.....	134
6.3.1 Calculated contact pressures.....	134
6.3.2 Typical results.....	135
6.3.2.1 First stage of the test.....	135
6.3.2.2 Second stage of the test.....	137
6.4 Buckling capacity.....	138
6.5 Summary.....	141
Chapter 7 – Conclusions	
7.1 Introductions.....	157
7.2 Summary of major conclusions.....	157
7.3 Implications in the design.....	160
7.4 Recommendation for future research.....	161
List of References	163
Appendix A	170

LIST OF TABLES

Table 3.1	Summary of the advantages and disadvantages of the different end conditions of the pipes	44
Table 3.2	Summary of the seal configurations tested that allow radial deformations at the ends of the pipe.....	45
Table 5.1	Summary of the experimental results	93
Table 5.2	Summary of visual observations of buckling failure.....	94
Table 6.1	Maximum pipe strain, duration of the test and strain rate for each test	143
Table 6.2	Duration of the first stage, $P'c$ and A' at the end of the first stage for each test	144
Table 6.3	Comparison of the capacity beyond $P'c=0$ to the solutions by Cheney and Glock	145

LIST OF FIGURES

Figure 1.1	Photograph of a concrete manhole	6
Figure 1.2	HDPE manhole from plan view	7
Figure 1.3	Buckling failure from plan view	8
Figure 2.1	Vertical load acting on a soil with a buried flexible pipe	25
Figure 2.2	Vertical load acting on a soil with a rigid flexible pipe	26
Figure 2.3	Illustration of neutral arching	27
Figure 2.4	Stresses in a homogenous block of soil and a pipe	28
Figure 2.5	Undeformed and buckled shape of a pipe under external hydrostatic pressure with no soil support	29
Figure 2.6	Multiwave and single wave modes of buckling	30
Figure 3.1	Stresses acting on the soil and the pipe during a test	46
Figure 3.2	Plan and elevation view of the pipe modelled in the finite element analysis illustrating the dimensions and the applied load	47
Figure 3.3	Influence of the end conditions of the pipe on the circumferential stress	48
Figure 3.4	Photographs showing the seal tests of rubber sheets	49
Figure 3.5	Photographs showing the tests made on Welch's seals	50
Figure 3.6	Elevation view of the test cell	51
Figure 3.7	Photograph of the test cell	52
Figure 4.1	Grain size distribution of the gravel used in the tests	64

Figure 4.2	Photograph of the gravel used in the tests	65
Figure 4.3	Grain size distribution of the sand used in the tests	66
Figure 4.4	Plan and elevation view of the linear potentiometers	67
Figure 4.5	Photograph of the infrared camera used in the tests	68
Figure 4.6	Photograph of the bottom seal of the pipe	69
Figure 4.7	Photograph of one of the HDPE pipes used in one test	70
Figure 4.8	Photograph of the PVC cap and the gasket of the top seal of the pipe	71
Figure 4.9	Photograph of the top seal of the pipe	72
Figure 4.10	Photograph and drawing showing the backfilling operation...	73
Figure 4.11	Photograph of the test cell lid with the instrumentation installed on it	74
Figure 4.12	Test components and their layout	75
Figure 4.13	Load path of the applied bladder and pore pressure used for the tests	76
Figure 5.1	Diameter change of a pipe under pressure	95
Figure 5.2	Applied bladder and pore pressure versus time for test T1 ...	96
Figure 5.3	Diameter change vs. time for test T1	97
Figure 5.4	Applied bladder and pore pressure versus time for test T2 ...	98
Figure 5.5	Diameter change vs. time for test T2	99
Figure 5.6	Applied bladder and pore pressure versus time for test T3 ...	100

Figure 5.7	Diameter change vs. time for test T3	101
Figure 5.8	Applied bladder and pore pressure versus time for test T4 ...	102
Figure 5.9	Diameter change vs. time for test T4	103
Figure 5.10	Applied bladder and pore pressure versus time for test T5 ...	104
Figure 5.11	Diameter change vs. time for test T5	105
Figure 5.12	Applied bladder and pore pressure versus time for test T6 ...	106
Figure 5.13	Diameter change vs. time for test T6	107
Figure 5.14	Pore pressure at buckling versus effective bladder pressure for all the tests	108
Figure 5.15	Infrared camera image of the inside of the pipe before buckling for test T1	109
Figure 5.16	Infrared camera image of the inside of the pipe showing initiation of the dimple at t=2953 seconds for test T1	109
Figure 5.17	Infrared camera image of the inside of the pipe showing the propagation of the dimple at t=2954 seconds for test T1	110
Figure 5.18	Infrared camera image of the inside of the pipe showing the propagation of the dimple at t=2955 seconds for test T1	110
Figure 5.19	Infrared camera image of the inside of the pipe showing the propagation of the dimple at t=2957 seconds for test T1	111
Figure 5.20	Infrared camera image of the inside of the pipe showing the full development of the dimple at t=2958 seconds for test T1	111
Figure 5.21	Infrared camera image of the inside of the pipe before buckling for test T2	112
Figure 5.22	Infrared camera image of the inside of the pipe showing initiation of the dimple at t=5717 seconds for test T2	112
Figure 5.23	Infrared camera image of the inside of the pipe showing the propagation of the dimple at t=5718 seconds for test T2	113

Figure 5.24	Infrared camera image of the inside of the pipe showing the propagation of the dimple at t=5719 seconds for test T2	113
Figure 5.25	Infrared camera image of the inside of the pipe showing the propagation of the dimple at t=5720 seconds for test T2	114
Figure 5.26	Infrared camera image of the inside of the pipe showing the full development of the dimple at t=5722 seconds for test T2	114
Figure 5.27	Infrared camera image of the inside of the pipe before buckling for test T3	115
Figure 5.28	Infrared camera image of the inside of the pipe showing initiation of the dimple at t=8996 seconds for test T3	115
Figure 5.29	Infrared camera image of the inside of the pipe showing the propagation of the dimple at t=8998 seconds for test T3	116
Figure 5.30	Infrared camera image of the inside of the pipe showing the propagation of the dimple at t=9000 seconds for test T3	116
Figure 5.31	Infrared camera image of the inside of the pipe showing the propagation of the dimple at t=9001 seconds for test T3	117
Figure 5.32	Infrared camera image of the inside of the pipe showing the full development of the dimple at t=9003 seconds for test T3	117
Figure 5.33	Infrared camera image of the inside of the pipe before buckling for test T4	118
Figure 5.34	Infrared camera image of the inside of the pipe showing initiation of the dimple at t=6991 seconds for test T4	118
Figure 5.35	Infrared camera image of the inside of the pipe showing the propagation of the dimple at t=6993 seconds for test T4	119
Figure 5.36	Infrared camera image of the inside of the pipe showing the full development of the dimple at t=6995 seconds for test T4	119
Figure 5.37	Infrared camera image of the inside of the pipe before buckling for test T5	120

Figure 5.38	Infrared camera image of the inside of the pipe showing initiation of the dimple at t=7021 seconds for test T5	120
Figure 5.39	Infrared camera image of the inside of the pipe showing the propagation of the dimple at t=7022 seconds for test T5	121
Figure 5.40	Infrared camera image of the inside of the pipe showing the propagation of the dimple at t=7023 seconds for test T5	121
Figure 5.41	Infrared camera image of the inside of the pipe showing the full development of the dimple at t=7025 seconds for test T5	122
Figure 5.42	Infrared camera image of the inside of the pipe before buckling for test T6	123
Figure 5.43	Infrared camera image of the inside of the pipe showing initiation of the dimple at t=12026 seconds for test T6	123
Figure 5.44	Infrared camera image of the inside of the pipe showing the propagation of the dimple at t=12027 seconds for test T6	124
Figure 5.45	Infrared camera image of the inside of the pipe showing the propagation of the dimple at t=12029 seconds for test T6	124
Figure 5.46	Infrared camera image of the inside of the pipe showing the full development of the dimple at t=12031 seconds for test T6 ...	125
Figure 5.47	Photos of the buckled pipes for all tests	126
Figure 5.48	Sketches of the undeformed and buckled shape of the pipes for all tests	127
Figure 6.1	Illustration of the first stage of the tests	146
Figure 6.2	Illustration of the second stage of the tests	147
Figure 6.3	Square HDPE unit block modelled to calculate stresses from imposed strains	148
Figure 6.4	Magnitude of E_p versus time	149
Figure 6.5	Load path of P' , P_c , P'_c and u for test T1	150
Figure 6.6	Load path of P' , P_c , P'_c and u for test T2	151

Figure 6.7	Load path of P' , P_c , P'_c and u for test T3	152
Figure 6.8	Load path of P' , P_c , P'_c and u for test T5	153
Figure 6.9	Load path of P' , P_c , P'_c and u for test T6	154
Figure 6.10	Illustration of arching during the second stage of the tests	155
Figure 6.11	Illustration showing the difference between the assumptions made by Cheney and the actual conditions of the tests	156

LIST OF NOTATIONS AND SYMBOLS

A'	Arching factor
ASTM	American Society for Testing and Materials
B'	Factor in Luscher's formula to take into account the burial depth of a pipe
C	Compressibility ratio
D_p	Original external pipe diameter (mm)
D_{pi}	Original internal pipe diameter (mm)
D_s	Original diameter of a disk of soil (mm)
D_t	Deformed pipe diameter (mm)
DR	Pipe dimension ratio
E_p	Pipe modulus (kPa)
E_s	Soil modulus (kPa)
G_s	Soil shear modulus (kPa)
Gs	Soil specific gravity

HDPE	High-density polyethylene
I_p	Moment of inertia of pipe wall (mm^4/mm)
k	Modulus of subgrade reaction (kPa)
k_1	Resistance of the soil to inward deformations of the pipe (kPa)
k_2	Resistance of the soil to outward deformations of the pipe (kPa)
L	Pipe length (mm)
n	Harmonic number
n_{cr}	Critical harmonic number
N	Pipe thrust (kN/m)
N_{cr}	Critical buckling thrust (kN/m)
P	Bladder pressure (kPa)
P'	Effective bladder pressure (kPa)
P_c	Total contact pressure (kPa)
P'_c	Effective contact pressure (kPa)

P_{cr}	Critical buckling pressure (kPa)
q	Radial unit pressure applied for the finite element analysis (MPa)
r_p	Pipe radius (mm)
R	Bouyancy reduction factor
t_p	Pipe thickness (mm)
u	Pore pressure (kPa)
$\epsilon_{\theta\theta}$	Circumferential strain at the internal surface of the pipe
ΔD_p	Change in pipe diameter (mm)
ΔD_s	Change in diameter of a disk of soil (mm)
ν_p	Poisson's ratio of the pipe
ν_s	Poisson's ratio of the soil
σ_m	Uniform stress component (kPa)
$\sigma_{\theta\theta}$	Pipe circumferential stress (kPa)
σ_{zz}	Pipe axial stress (kPa)

ω_{θ}	Circumferential pipe deformation (radian)
$\omega_{\theta n}$	Maximum circumferential deformation of a lobe or dimple during buckling (radian)
$\omega_{P'c}$	Inward radial pipe deflection due to the effective contact pressure $P'c$ (mm)
ω_r	Inward radial pipe deflection (mm)
ω_{rn}	Maximum radial deflection of a lobe or dimple during buckling (mm)
ω_{ur}	Inward radial pipe deflection due to the pore pressure u acting radially (mm)
ω_{ur}	Inward radial pipe deflection due to the pore pressure u acting radially (mm)
ω_{uz}	Inward radial pipe deflection due to the pore pressure u acting axially (mm)

1. Introduction

1.1 Description of the problem

Manholes are vertical shafts that provide access for the inspection and maintenance of drainage systems in landfills. Figure 1.1 shows a photograph of a concrete manhole in a landfill during the construction phase. According to Gartung et al. (1989) a typical problem with concrete manholes is the corrosion that occurs in the shaft due to the exposure to acid chemistry, which in some cases had led to structural failure after about 5 years of operation. Plastic materials, such as high-density polyethylene (HDPE), are beneficial due to their excellent resistance to chemically aggressive environments such as those found in landfills.

The increasing landfill depths compel the use of manholes as large as 70 meters in height, resulting in significant radial loads acting on the manhole. Therefore, manholes should have sufficient structural capacity to withstand the radial loads without collapsing and putting in risk the life of the maintenance personal that may access the shafts.

As it is shown in Figure 1.2, a gravel ring surrounds plastic manholes therefore the horizontal loads from the waste are transmitted to the manhole through the gravel. Eventual clogging of the drainage system of the landfill could result in saturation of the gravel ring. Therefore the manhole would be subjected to ground (transmitted through the gravel ring) and fluid loads. The ultimate limit state of circumferential buckling of polymer manholes under

ground and fluid loads is currently unknown. Figure 1.3 illustrates the circumferential buckling failure from a plan view.

There is a paucity of good quality experimental and field data regarding the buckling capacity of manholes or pipes under ground and fluid loads. An experimental program was therefore needed to better quantify the pipe buckling under ground and fluid loads.

1.2 Current state of practice

The current practice for the design of high-density polyethylene (HDPE) manholes for subsurface application is given in standard ASTM F1759-97. This standard presents Luscher's equation to predict the buckling capacity for combined ground and fluid loads. Luscher's equation is given in Equation 2.21.

The major disadvantage of Luscher's solution is that it models the soil as radial springs instead of as a continuum. When the radial spring model is used, the shear stresses between the pipe and the soil are ignored and poor predictions are made of the number of lobes that are formed around the circumference during buckling. The shortcomings of Luscher's solution are detailed in Section 2.6. A solution for the buckling capacity of pipes under ground and fluid loads that models the soil as a continuum has not been published to date.

1.3 Objectives and methodology

This thesis presents an experimental study of pipe buckling under ground and fluid loads in order to understand some of the factors involved in the buckling failure of manholes. The experiments were performed on HDPE pipes and the loading conditions applied reproduced to some extent those at which manholes are subject. In the following chapters of this thesis the attention is focused on pipes symmetrically loaded in the radial direction because the observations of pipe buckling under those load conditions are applicable to manholes. The specific objectives of this research were to:

- Design and construct a new test cell that would allow the application of ground and fluid pressures to plastic pipes up to buckling failure,
- Develop a new set of experimental procedures to conduct pipe buckling experiments under ground and fluid pressures,
- Measure the pipe response under the applied ground and fluid pressures and record a visual sequence of the inside of the pipe during buckling, and
- Describe the soil-structure interaction that leads to buckling failure.

Since this is the first time that these types of experiments have been conducted, the development of a new test cell and the experimental procedures are important contributions of this thesis. The measurements and observations obtained from the experimental program represent a contribution to better understand the limit state of pipe buckling under ground and fluid loads.

1.4 Organization of the thesis

Following the introduction of Chapter 1, a literature review related to the problem is presented in Chapter 2. The concepts of arching and soil-structure interaction are presented. A review of the different circumferential pipe buckling solutions and their applicability is given. Finally, a critical analysis of previous tests made on cylinders under ground and fluid loads is also presented.

The concept of the new experimental facility along with a description of the applied loads is then presented in Chapter 3. An analysis of the influence of radial and axial end constraints on the circumferential stresses of the pipe is given. Finally the new test cell is described and its design explained.

Chapter 4 then describes the specific materials and the instrumentation used for the experimental program. Also given are the procedures developed for the setup of the tests and the method used to apply earth and fluid pressures.

Results from six experiments conducted in the new cell are presented in Chapter 5. Tests were conducted with two different pipe thickness and three different values of effective bladder pressure P' . The data obtained were measurements of applied pressure and pipe deflections. A visual sequence of the buckling failure is also presented.

Chapter 6 is the analysis of the data given in Chapter 5. A method to analyze the soil-structure interaction was presented along with the results.

This analysis provides a quantitative description of the loads (ground and fluid) that acted on the pipe and the variation of their magnitudes with time.

The thesis concludes with Chapter 7 where the specific conclusions obtained from the tests are summarized and recommendations for further research are given.

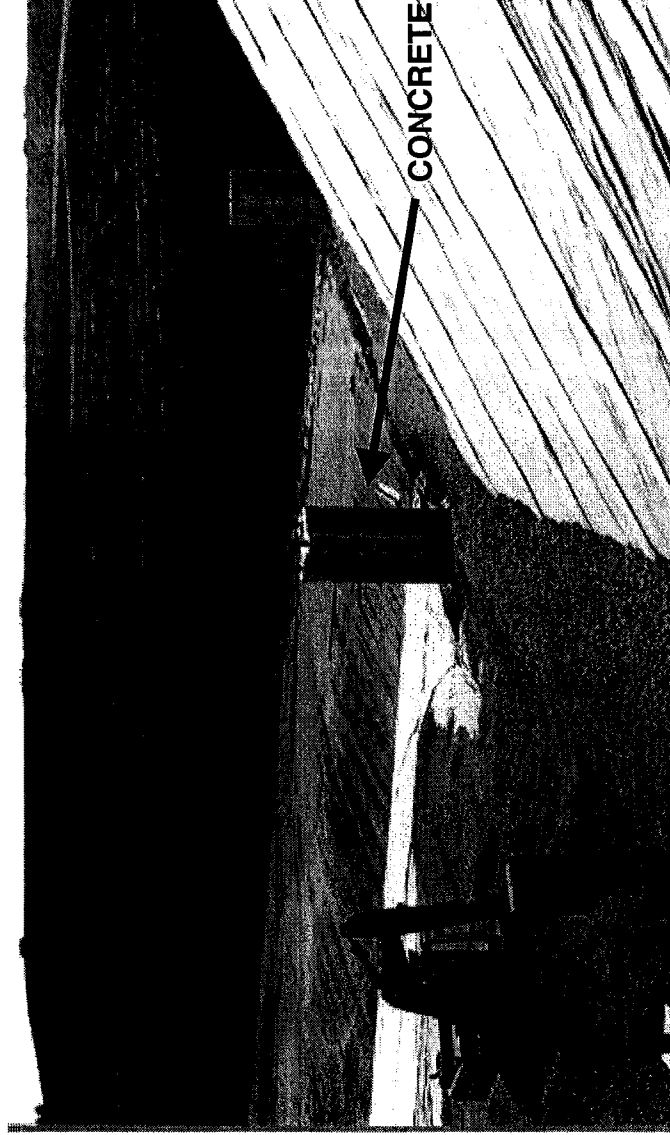


FIGURE 1.1 PHOTOGRAPH OF A CONCRETE MANHOLE IN A LANDFILL DURING THE CONSTRUCTION PHASE

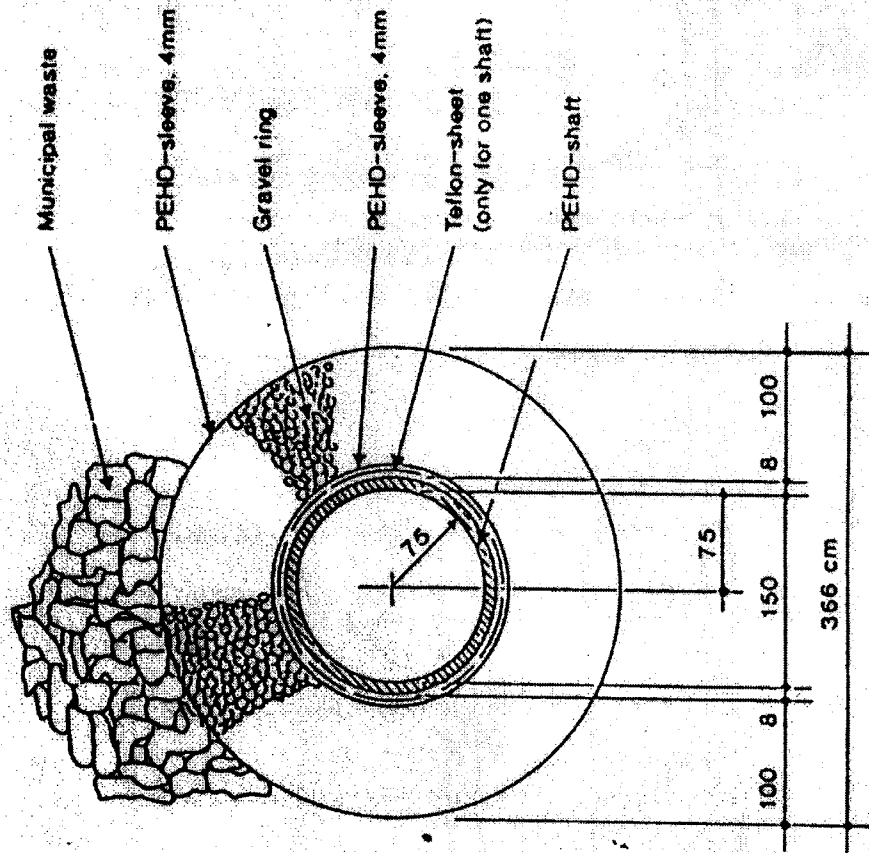


FIGURE 1.2 PLAN VIEW OF A HIGH-DENSITY POLYETHYLENE MANHOLE WITH A GRAVEL RING SURROUNDING IT (TAKEN FROM GARTUNG ET AL. (1993))

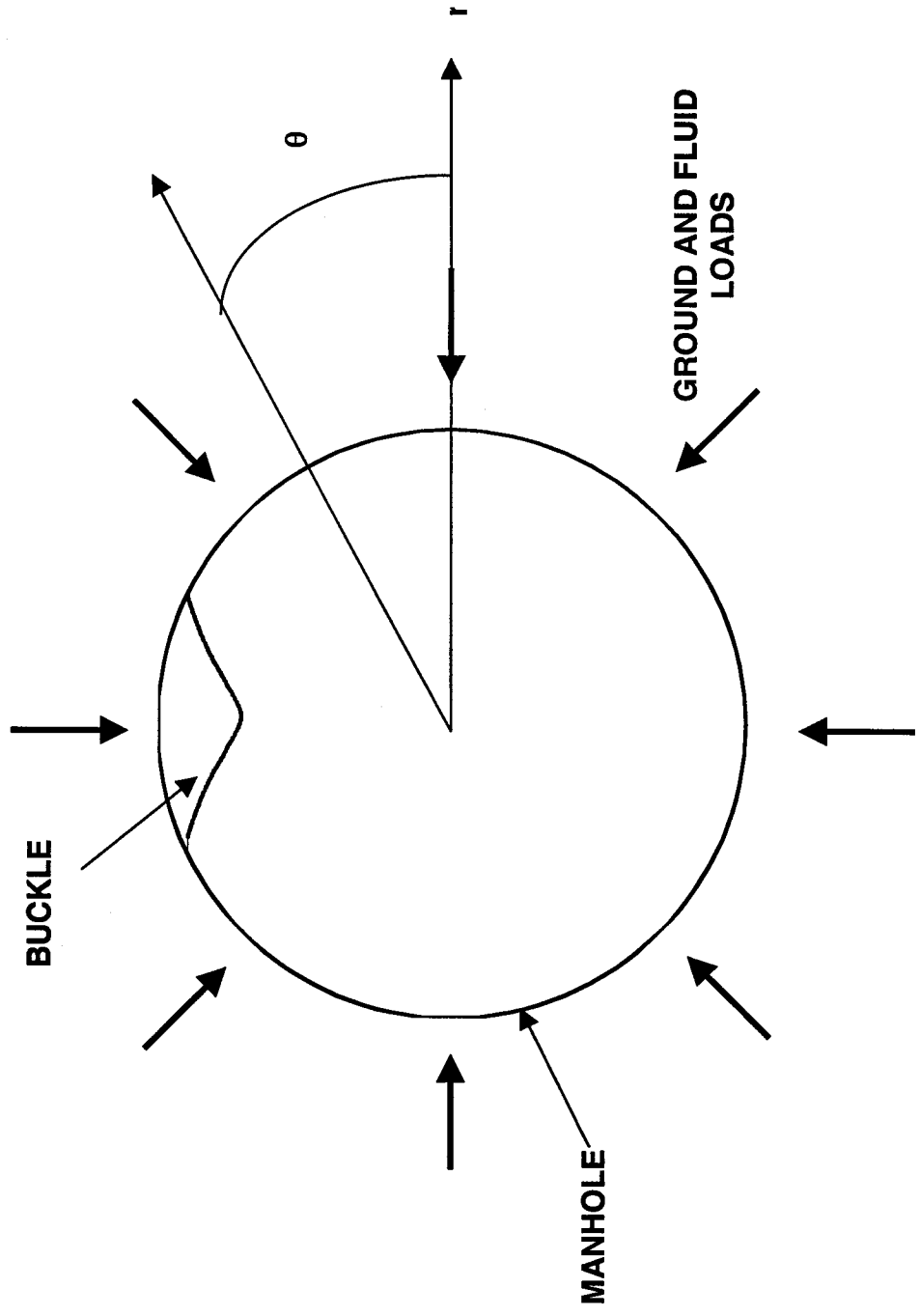


FIGURE 1.3 ILLUSTRATION OF THE BUCKLING FAILURE FROM PLAN VIEW

2 Literature review

2.1 Introduction

This chapter provides a discussion of the concepts that are needed for the development of the test facility and the experimental procedures. Also presented is the necessary theory to understand the test results within the limits of this research program and a background of previous experiments of pipe buckling under ground and fluid loads.

First, the concept of arching or redistribution of stresses is explained. Then a review of most of the available buckling solutions is presented along with their applicability. An evaluation of the buckling formula currently used for pipes under ground and fluid loads is also made. Finally, previous experiments of pipes under ground and fluid loads are described and their usefulness evaluated.

2.2 Arching

The loads applied to a pipe-soil system (such as a manhole) are redistributed between the pipe and the soil. A certain proportion of the load reaches the pipe and the remaining load is carried by the soil. This mechanism of load sharing is known as arching.

2.2.1 Mechanism of arching

The less stiff a component is, the lower the load fraction it will attract. Figure 2.1 illustrates a mass of soil with a vertical load applied at the top boundary of

the soil. The system can be divided in three columns where the center column is less stiff than the exterior columns. The entire system deforms vertically but the center column deforms more than the exterior ones. The difference of deformations, which is a result of the different stiffness of the columns, mobilizes shear stresses between columns resulting in a reduction of the vertical stress that reaches the bottom of the central column.

However, if a component is relatively more rigid it will attract a higher fraction of load. Figure 2.2 illustrates the case when the center column is stiffer than the exterior columns. Under this condition, the exterior columns deform more than the central column and the mobilized shear stresses increase the load that reaches the bottom of the central column.

For a pipe-soil system, arching would promote a sharing of loads between the soil and the pipe, which depends on the stiffness of both components. Depending on the resulting load redistribution, arching can be classified as neutral, positive or negative arching.

2.2.2 Neutral arching

Neutral arching occurs when the pipe has the same compressive stiffness as the soil it replaces. Figure 2.3 (a) shows a hypothetical situation of a block of soil loaded by a pressure σ_m at the vertical and horizontal boundaries. The dashed circle shows the original shape of the disk of soil that would be replaced by a pipe and the dotted circle is the deformed shape of this disk of soil under the imposed loads. The radial stress that reaches the disk of soil is

equal to σ_m . Figure 2.3 (b) shows the same block of soil, but with a pipe that had an original diameter equal to the undeformed disk of soil shown in Figure 2.3 (a). Under the pressure σ_m applied at the soil boundaries, the pipe deforms the same magnitude as the disk of soil in Figure 2.3 (a). Therefore the radial stress that reaches the pipe is equal to σ_m as it occurs for the disk of soil in Figure 2.3 (a). This example illustrates the condition of neutral arching.

2.2.3 Positive and negative arching

Neutral arching is not a common case. Most of the time pipes will be more or less stiff than the mass of soil they replace.

For a pipe that is stiffer than the soil it replaces, the stresses that reach the pipe, i.e. the effective contact pressure, P'_c will be higher than the pressure applied to the soil boundary σ_m . This condition of the pipe attracting loads from the soil is known as negative arching.

If the stiffness of the pipe is lower than the mass of soil that is being replaced then the stress that reach the pipe P'_c will be less than the pressure applied to the soil boundary σ_m . This condition is called 'positive arching'. Positive arching normally occurs in high-density polyethylene (HDPE) pipes and manholes because they are thin and the HDPE modulus is relatively low.

2.2.4 Arching solution

Solutions have been developed in order to calculate the arching phenomena or load sharing mechanism between the pipe and the soil. The stiffness of a pipe-soil system can be divided into two types. The first is the extensional stiffness, which is a measure of to the equal all-around uniform pressure that cause a unit diametric strain of the pipe with no change in shape. The other type is the flexural stiffness, which is a measure of the magnitude of the non-uniform pressure necessary that cause a unit diametric strain that results in an ovaling of the pipe.

For the tests performed in this research work only the extensional stiffness is relevant. Therefore only the aspects of the extensional stiffness in the arching solution will be considered in this literature review.

Hoeg (1968) developed an elastic arching solution by taking into account the relative stiffness of the soil medium to that of the pipe. For the solution, the parameter C or compressibility ratio was introduced, which is equal to the extensional stiffness of the soil medium divided by that of the pipe.

The extensional stiffness of the soil can be obtained by considering a homogenous and isotropic block of soil under a uniform stress σ_m as it is shown in Figure 2.4(a).

The diametric strain across the dotted line, which represents the location of an imaginary pipe, is given by:

$$\Delta D_s/D_s = \varepsilon_m = (\sigma_m/E_s)(1+\nu_s)(1-2\nu_s) \quad (\text{Eq. 2.1})$$

where ΔD_s and D_s are the change in diameter of the disk of soil and the original diameter of the disk of soil respectively. σ_m and ϵ_m are the radial stress and the circumferential strain of the soil disk respectively. E_s and ν_s are the elastic modulus and the Poisson's ratio of the soil respectively.

The extensional stiffness is given by:

$$[\sigma_m/(\Delta D_s / D_s)] = E_s / (1+\nu_s)(1-2\nu_s) \quad (\text{Eq. 2.2})$$

Now considering the extensional stiffness of the pipe, the diametric strain of a pipe under uniform compression, as it is shown in Figure 2.4 (b) is given by:

$$\Delta D_p/D_p = (P'c)(r_p)/(E_p)(t_p) \quad (\text{Eq. 2.3})$$

where ΔD_p and D_p are the change in pipe diameter and the original pipe diameter respectively. $P'c$ is the effective pressure acting on the pipe, r_p , E_p and t_p are the radius, elastic modulus and thickness of the pipe respectively.

For axial plane strain, the pipe modulus E_p should be replaced by the term $E_p / (1-\nu_p^2)$ where ν_p is the Poisson's ratio of the pipe. The extensional stiffness of the pipe is given by:

$$[(P'c)/(\Delta D_p/ D_p)] = [(E_p)(t_p)/(r_p)] / (1-\nu_p^2) \quad (\text{Eq. 2.4})$$

The compressibility ratio C , is obtained by dividing the extensional stiffness of the soil (Equation 2.2) by the extensional stiffness of the pipe (Equation 2.4):

$$C = [E_s / (1+\nu_s)(1-2\nu_s)] / \{[(E_p)(t_p)/(r_p)] / (1-\nu_p^2)\} \quad (\text{Eq. 2.5})$$

The ratio of the effective stresses that reach the pipe P'_c to the stresses applied to the boundary of the soil σ_m is denoted by the term A' , which is called the arching factor and is given by:

$$A' = (P'_c)/(\sigma_m) = 1 - [(1-2\nu_s)*(C-1)/((1-2\nu_s)*C+1)] \quad (\text{Eq. 2.6})$$

The above solution allows the calculation of the stress acting on the pipe given the stiffness characteristics of both the soil and the pipe.

2.3 Pipe Thrust

Thrust, which is denoted here as N , is the force per meter of length that acts circumferentially in the pipe as a result of the external pressures. Some buckling solutions are given in terms of thrust. In the absence of bending, the relation between the total contact pressure P_c and the magnitude of thrust N is given by:

$$N = (P_c)(r_p) \quad (\text{Eq. 2.7})$$

2.4 Review of circumferential buckling solutions

Buckling occurs in a flexible pipe when circumferential compressive stresses act on the structure reducing its flexural stiffness producing a curvature reversal at failure.

Many solutions have been developed in order to predict the buckling capacity of pipes. The following is a review of those solutions and their applicability.

2.4.1 Buckling of unsupported pipes under uniform external pressures

Levy (1884) developed a solution for a pipe, without any external support, which is loaded by an external hydrostatic pressure. The critical buckling pressure, under axial plane stress conditions, is given by:

$$P_{cr} = 3 [E_p I_p / (r_p)^3] \quad (\text{Eq. 2.8})$$

Where I_p is the moment of inertia of the pipe, which is equal to $t_p^3/12$. The mode of buckling under this condition is illustrated in Figure 2.5.

2.4.2 Buckling of soil surrounded pipes

The buckling solution of Equation 2.8 applies when there is no soil around the pipe. Jenkins and Kroll (1981) presented experimental evidence that the buckling resistance is enhanced by the presence of soil or grout around the pipe.

2.4.2.1 Linear multiwave theories

Linear multiwave theories assume that during buckling failure a number of buckles form around the circumference of the pipe as it is illustrated in Figure 2.6 (a). Failure is considered to occur as a harmonic disturbance in which the circumferential stress at zero bending stiffness is calculated. The radial and circumferential displacements ω_r and ω_θ are a function of the circumferential coordinate θ . The value of those displacements is given by the following equations:

$$\omega_r = \omega_{rn}(\cos n\theta) \quad (\text{Eq. 2.9})$$

$$\omega\theta = \omega_{\theta n}(\sin n\theta) \quad (\text{Eq. 2.10})$$

Where ω_m and $\omega_{\theta n}$ are respectively the maximum radial and circumferential displacements of a lobe during buckling. n is the harmonic number or number of lobes around the pipe circumference during buckling. The critical circumferential stress, which is the stress at buckling, is a function of the harmonic number n and also of the ground and pipe stiffness.

a) Multiwave Theory Using The Winkler Model

This Winkler concept models the soil as a series of springs that resists the radial deformations of the pipe. For a modulus of subgrade reaction k and having the ground resisting both inward and outward deformations of the pipe, the critical uniform thrust is given by:

$$N_{cr} = (n^2 - 1)[E_p I_p / (r_p^2)] + [((k)(r_p)) / (n^2 - 1)] \quad (\text{Eq. 2.11})$$

For large values of n , the harmonic number that gives the value of N_{cr} is:

$$n_{cr} = (kr_p^3 / E_p I_p)^{1/4} \quad (\text{Eq. 2.12})$$

and the critical thrust will be given by:

$$N_{cr} = 2(E_p I_p (k) / r_p)^{1/2} \quad (\text{Eq. 2.13})$$

Equation 2.13 corresponds to the expression presented by Meyerhof and Baikie (1963).

b) Multiwave Theory Using The Elastic Continuum Model

Forrestal and Herman (1965) developed a solution with the multiwave theory that models the soil as an elastic continuum. The hoop thrust that lead to buckling when there is no slip along the soil-pipe interface is given by:

$$N=(n^2 -1)[E_p I_p /r_p^2]+[(2(G_s)(r_p))((2n(1-v_s) - (1-2v_s))/(n^2(3-4v_s)))] \quad \text{(Eq. 2.14)}$$

where G_s is the soil shear modulus, which is equal to $E_s/(2(1+v_s))$. When there is no shear stress transmission the critical thrust is given by:

$$N=(n^2 -1)[E_p I_p /r_p^2]+[(2(G_s)(r_p))(1/(2n(1-v_s) - (1-2v_s)))] \quad \text{(Eq. 2.15)}$$

For the Equations 2.14 and 2.15, it is assumed that the ground resists both inward and outward deformations of the pipe. For large values of n and a smooth surface of the pipe-soil interface, which is the most conservative condition, the critical value of the harmonic number n is given by:

$$n_{cr} = ((E_p)(I_p)(2)(1-v_s)/(G_s)(r_p)^3)^{-1/3} \quad \text{(Eq. 2.16)}$$

and the critical hoop thrust is given by:

$$N_{cr} = 1.2(E_p I_p)^{1/3}(E_s/(1-v_s^2))^{2/3} \quad \text{(Eq. 2.17)}$$

2.4.2.2 Single wave solutions

For the single wave solutions, buckling failure is assumed to occur as a single buckle around the circumference as it is shown in Figure 2.6 (b). According to Gumbel (1983), this mechanism of deformation implies a change in length and shape of buckle with increasing wave amplitude to snap-through failure.

a) Pipes inside a rigid cavity

Solutions have been developed which are applicable to the case of liners inside rigid hosts. For example this could be the case of a flexible liner inside a deteriorated concrete pipe. It is assumed in these solutions that the host resists all outward deformation of the pipe or liner but it doesn't constraint the pipe to deform inwards. The critical pressure does not increase indefinitely as the stiffness of the host increases but is limited by the stiffness of the liner. Glock (1977) developed a solution for the case of an infinitely rigid cavity around a liner. The liner is loaded under an external hydrostatic pressure. As the liner deforms the host doesn't follow this deformation therefore a separation is assumed to occur between the liner and the cavity. The critical buckling pressure of the liner for this case under a plane condition is given by:

$$P_{cr} = [E_p/(1-\nu_p^2)](t_p/D_p)^{2.2} \quad \text{(Ep. 2.18)}$$

Where ν_p and D_p are the Poisson's ratio and the diameter of the liner respectively.

Cheney (1971) developed a solution for the same problem but assuming that the cavity moves along with the pipe up to the point of buckling. Under this condition the critical pressure is given by:

$$P_{cr} = (2.5) [E_p/(1-\nu_p^2)](t_p/D_p)^{2.2} \quad \text{(Ep. 2.19)}$$

b) Pipes in a Winkler medium

Single wave solutions that assume a Winkler medium to model the soil were developed. The contribution by Kloppel and Glock (1970) led to a solution that

is similar to that of Equation 2.13 but with k reduced by a factor of 0.25. The critical thrust is given by:

$$N_{cr} = (E_p I_p (k) / r_p)^{1/2} \quad \text{(Eq. 2.20)}$$

2.5 Applicability of the buckling solutions

2.5.1 Single wave and multiwave theories

The applicability of either the single wave or multiwave theories can be better understood by considering the two possible restraining actions of the soil around the pipe. Those restraints are the resistance to inward and outward deformations of the pipe denoted here as k_1 and k_2 respectively.

The resistance of the soil to inward deformation depends on the nature of the loads that are applied to the pipe. If the loads that reach the pipe are transmitted mostly from the soil skeleton, i.e. effective stresses, then k_1 will roughly be equal to k_2 and the multiwave mode of buckling will control failure as indicated by Falter (1980).

On the other hand if the loads applied to the pipe are mostly fluid loads then the value of k_1 will be negligible and the single-wave mode of buckling will control failure as indicated by Sonntag (1966a, 1966b) and Hain (1970).

In conclusion, according to Moore (1989), when the effective stresses, which are the stresses transmitted through the soil skeleton, are low and the pore pressures are high the single wave mode of buckling control the failure. But if the effective stresses are high and the pore pressures are low the

multiwave mode of buckling will control the failure. The proportion of effective stresses to pore pressures at which the change in mode of buckling occurs has not been determined yet.

2.5.2 Winkler model and elastic continuum

Moore (1989) summarized the considerations made by previous authors regarding the advantages and disadvantages of the elastic continuum model and the Winkler model. It pointed out that the elastic continuum theory provides better predictions of the critical harmonic number and reliable test data, such as that presented by Allgood and Ciani (1968), Gumbel (1983) and Crabb and Carder (1985), supports the two-thirds power law of Equation 2.17 rather than the square-root relationship of Equation 2.17.

Another relevant point presented by Moore (1989) included the fact that the continuum theory predicts higher buckling capacities than those predicted using the Winkler medium. In that regard, Cheney (1976) recommended that a reduction factor of eight should be used for the soil modulus because it is the tangent soil modulus that controls the incremental response and the buckling capacity of the buried structure and not the secant modulus generally used to calculate buckling strength.

Finally, a comparison made by Moore (1989) between test data, the prediction based on the Winkler model and the elastic continuum model revealed that the latter is more adequate in the prediction of the experimental trends although it overestimate the buckling capacity.

2.6 Evaluation of Luscher's solution to predict buckling under combined loads

The solution developed by Luscher (1966) is the only available solution to predict buckling under combined ground and fluid loads. Luscher's solution uses the multiwave theory and models the soil using the Winkler medium.

The critical buckling thrust is given by:

$$N_{cr} = (2.825) [[(R B' E_s' E_p I_p) / (D_p)]^{1/2}] \quad \text{(Eq. 2.21)}$$

where D_p is the pipe diameter, E_p is the pipe modulus, I_p is the moment of inertia of the pipe, E_s' is the modulus of soil reaction and R is a buoyancy reduction factor given by:

$$R = 1 - (0.33)(H'/H) \quad \text{(Eq. 2.22)}$$

where H' is the height of groundwater above the invert and H is the height of the fill. The factor B' is given by:

$$B' = (1 / (1 + 4e^{(-0.213H)})) \quad \text{(Eq. 2.23)}$$

Due to arguments presented in Section 2.5.1, Luscher's formula is not applicable when the magnitude of effective stresses in the soil is low and high fluid pressure are present because it assumes a multi-wave mode of buckling. Another disadvantage of this solution is the use of the Winkler medium to model the soil. The shortcomings of the use of the Winkler medium were explained in Section 2.5.2.

2.7 Previous buckling tests with ground and fluid loads

Luscher (1966) reported the details of a test program carried out with aluminum and plastic pipes that had soil support around them. All the pipes had a diameter of 41 mm. The aluminum pipes had a thickness of 0.08 mm and the plastic pipes had a range of thickness from 0.13 mm to 0.2 mm. The ratio of unsupported length to diameter was 3.6. Effective stresses and pore pressures were applied to the pipes up to buckling failure.

The test program revealed the dependence of the number of waves on the level of effective stresses. As the effective stress was higher during the tests the number of waves at buckling increased. This is consistent with the argument presented in previous sections.

The usefulness of the test data obtained by Luscher (1966) is limited for several reasons:

First, the soil ring around the pipes had a thickness corresponding to 46% or 83% of the pipe radius. Moore et al. (1994) demonstrated the influence of a non-uniform soil ring around the pipe in the buckling capacity. This aspect was not taken into account, perhaps because of the lack of available numerical tools at the time when the tests were carried out. Second, the details of the backfilling and compaction were not fully explained. Third, the stress path used in the tests was not specified. This is an important aspect of a test program when pore pressures are applied. Finally, the use of scaled-down structures might have introduced uncertainties which were not taken into account.

Szpak (1981) performed experiments on polyethylene pipes with ground pressures and vacuum pressure on the inside of the structure to try to simulate the effect of fluid pressures. The experimental procedures and the reported data have the following shortcomings:

First, the stress path was not reported. Second, failure occurred in only one out of the five tests performed mainly because the vacuum pressures were very low and therefore unable to simulate high hydraulic heads.

Due to the limited usefulness of the tests performed by Luscher (1966) and Szpak (1981), there is an obvious need for good quality experimental data.

2.8 Summary

The concepts of arching were explained along with the arching solution developed by Hoeg (1968). An explanation of arching is important since this influences the loads that act on a pipe. Most HDPE pipes are less stiff than the soil they replace therefore positive arching occurs resulting in the pipes shedding load to the soil.

Most of the current buckling solutions were presented and their assumptions were described. The applicability of the solutions was discussed and the buckling formula used in the current practice for pipes under ground and fluid loads was evaluated. None of the solutions are able to quantify the buckling capacity of pipes under earth and fluid pressures.

Finally, previous tests with pipes under ground and fluid loads were reviewed and their limited usefulness discussed.

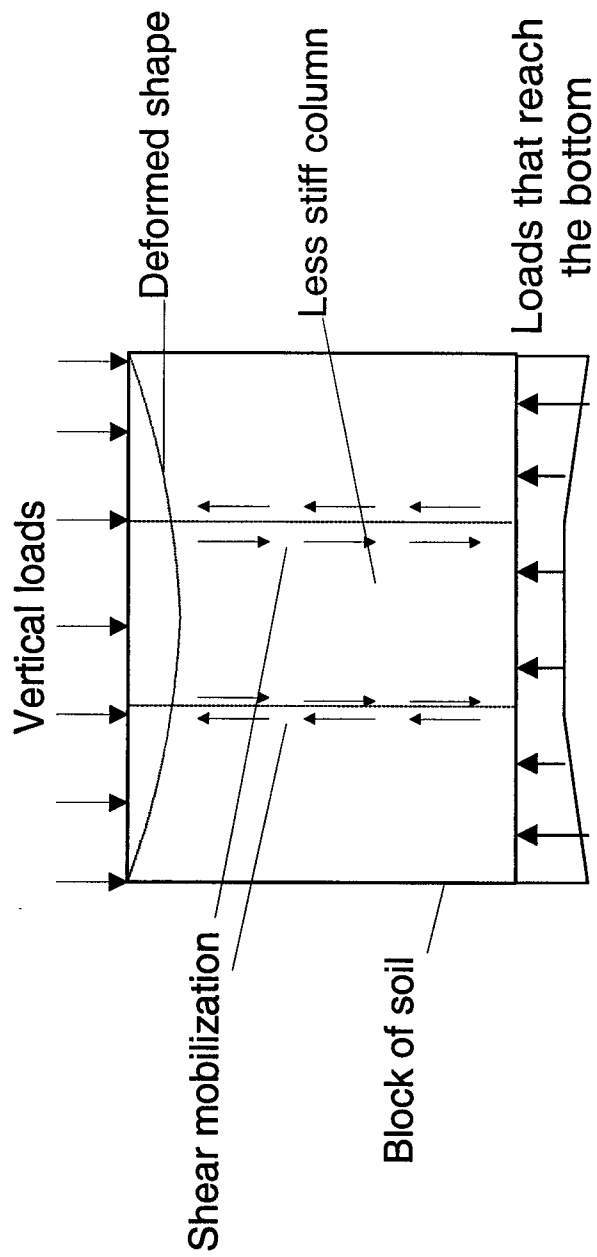


FIGURE 2.1 CENTRAL COLUMN LESS STIFF THAN EXTERNAL COLUMNS WITH A VERTICAL LOAD AT THE TOP BOUNDARY OF THE SOIL WITH MOBILIZATION OF SHEAR IN THE ADJACENT VERTICAL WALLS

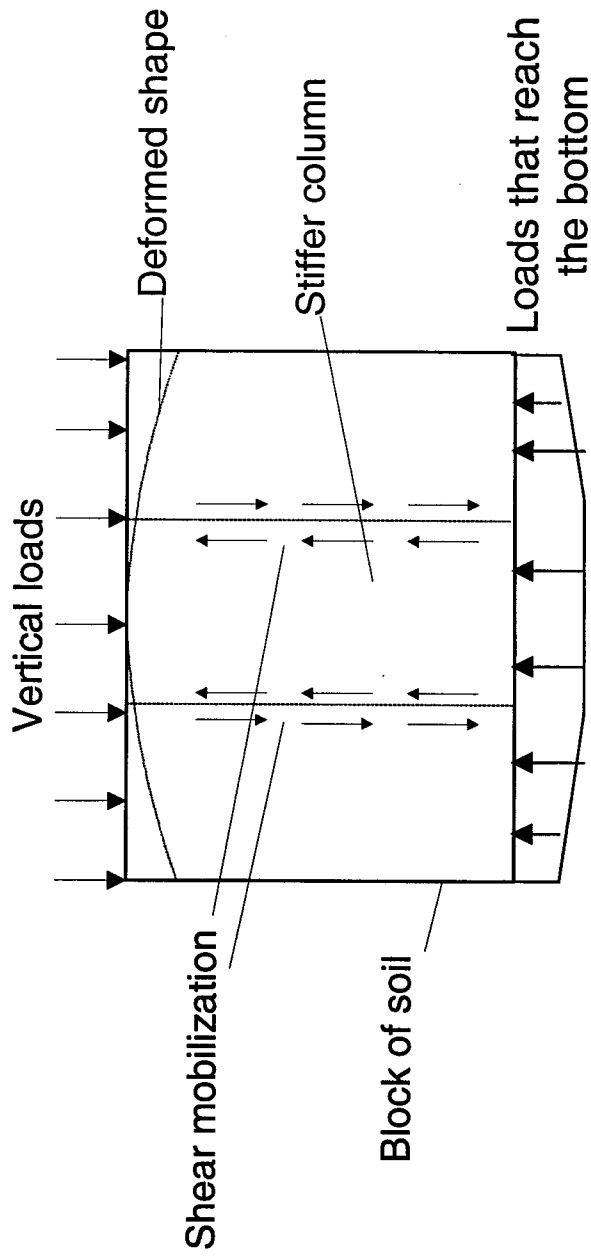
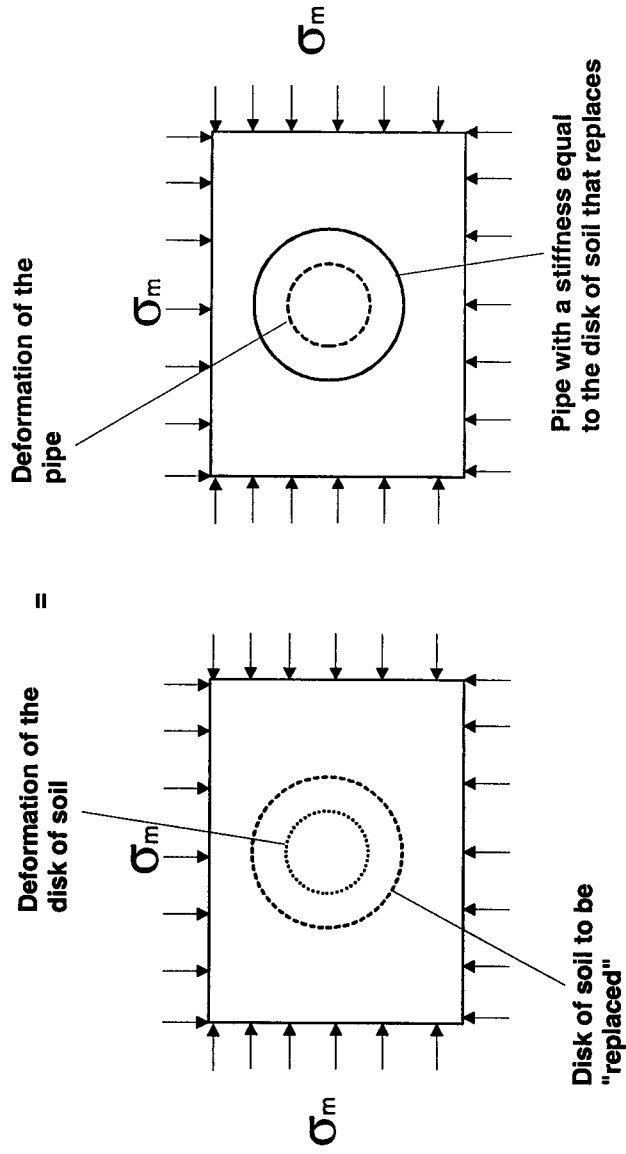


FIGURE 2.2 CENTRAL COLUMN STIFFER THAN EXTERNAL COLUMNS WITH A VERTICAL LOAD AT THE TOP BOUNDARY OF THE SOIL WITH MOBILIZATION OF SHEAR IN THE ADJACENT VERTICAL WALLS



NEUTRAL ARCHING

(a) (b)

FIGURE 2.3 ILLUSTRATION SHOWING NEUTRAL ARCHING (a) HYPOTHETICAL DISK OF SOIL DEFORMED UNDER THE STRESS σ_m APPLIED AT THE EXTERNAL SOIL BOUNDARY, (b) PIPE DEFORMED UNDER THE STRESS σ_m APPLIED AT THE EXTERNAL SOIL BOUNDARY

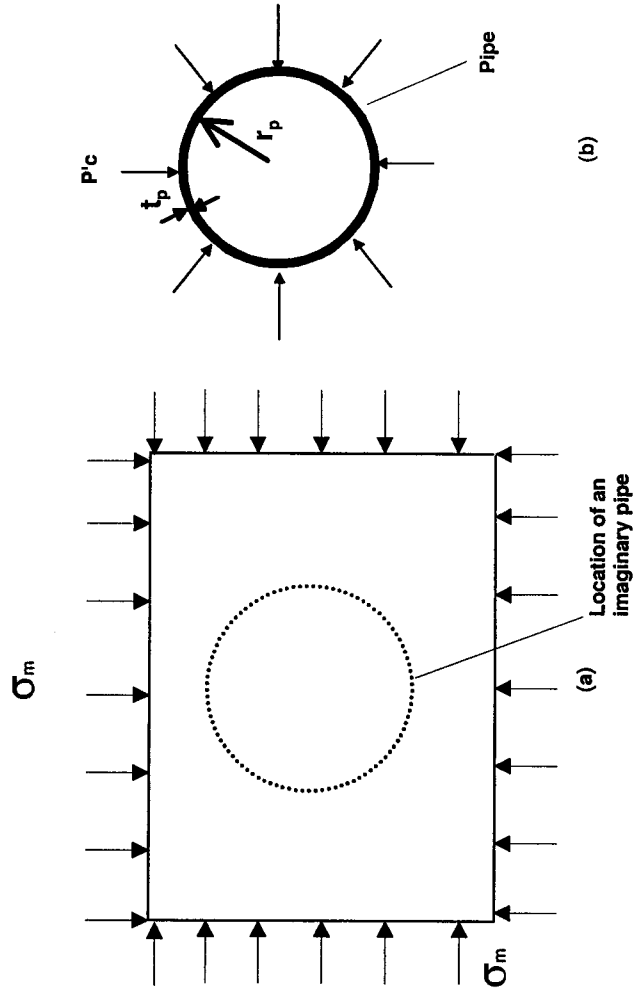


FIGURE 2.4 (a) HOMOGENEOUS, ISOTROPIC BLOCK OF SOIL UNDER A UNIFORM STRESS σ_m APPLIED AT THE EXTERNAL SOIL BOUNDARY, (b) PIPE UNDER UNIFORM COMPRESSION FROM EXTERNAL PRESSURE $P'c$

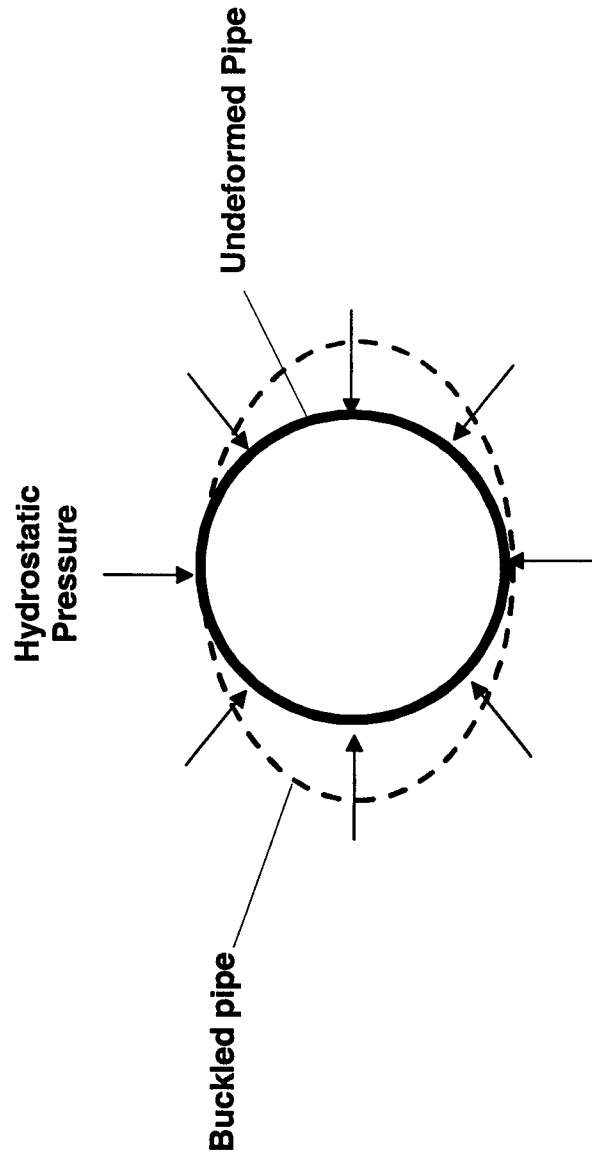
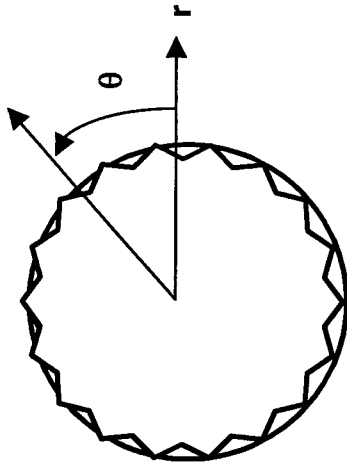
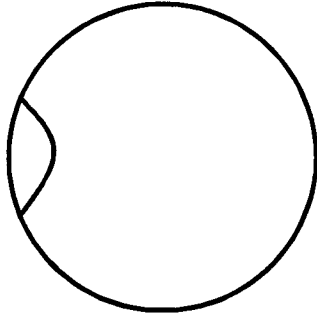


FIGURE 2.5 UNDEFORMED AND BUCKLED SHAPE OF THE PIPE UNDER FLUID LOADS AND WITH NO SOIL SUPPORT AROUND THE PIPE



Multi-wave mode of buckling

(a)



Single wave mode of buckling

(b)

FIGURE 2.6 (a) MULTI-WAVE MODE OF BUCKLING SHOWING SEVERAL DIMPLES FORMING AROUND THE PIPE CIRCUMFERENCE, (b) SINGLE WAVE MODE OF BUCKLING SHOWING THE FORMATION OF ONLY ONE DIMPLE IN THE PIPE CIRCUMFERENCE

3. Test concept and development of the test cell

3.1 Introduction

The buckling capacity of polymer pipes under combined ground and fluid loads was previously unknown. A new specialized testing facility was therefore designed and developed to measure the buckling capacity of polymer pipes under ground and fluid loads. The development of a new test cell and the experimental procedures was one of the major contributions of this thesis. In this Chapter the concept of the new experimental facility is explained. The nature of the applied stresses is described, the selection of end conditions for the pipe is analyzed and the test cell design is explained.

3.2 The test concept

The aim of the test program was to measure the buckling capacity of high-density polyethylene pipes under combined ground and fluid loads. Figure 3.1(a) shows a plan view of a ring of soil surrounding a polymer pipe. A pressure P is applied to the external boundary of the soil representing the radial earth pressure that may act on a manhole. The soil is saturated and the pore fluid is also pressurized to a certain magnitude u .

The effective pressure P' that compresses the soil ring is the difference of P and u , therefore:

$$P' = P - u \quad \text{[Eq. 3.1]}$$

The magnitude of the effective stress that reaches the pipe P'_c depends on the stiffness of the pipe and the soil ring. The arching factor A' , which was defined in Chapter 2, relates the magnitude of P'_c to the value of P' . The value of A' under the specific conditions of the tests is given by:

$$A' = P'_c / P' = P'_c / (P - u) \quad [\text{Eq. 3.2}]$$

Rearranging the terms of Equation 3.2, the value of P'_c is given by:

$$P'_c = (A')(P - u) \quad [\text{Eq. 3.3}]$$

As it is illustrated in Figure 3.1 (b), the total contact pressure acting at the pipe P_c is both the contribution of the effective contact pressure P'_c and the pore pressures u . Therefore P_c is given by:

$$P_c = P'_c + u \quad [\text{Eq. 3.4}]$$

By substituting Equation 3.3 in Equation 3.4 we have:

$$P_c = A' (P - u) + u \quad [\text{Eq. 3.5}]$$

3.3 Applied pressures

3.3.1 Earth loads

The pressure P was applied to the external soil boundary using a rubber bladder keeping the magnitude of the pressure P constant along the external soil boundary. A uniform radial pressure is representative of the radial earth pressures acting at some distance away from the manhole. Details of the rubber bladder are presented in Chapter 4.

3.3.2 Fluid loads

The pore pressure u was applied to the water that completely saturated the pores in the backfill. Pressurization of the pore fluid was attained through a fitting on the test cell. A detailed description of the test cell is given in Section 3.5.

3.4 Pipe end conditions

Constraining the radial deformations at the ends of the pipe affect the circumferential stress and the buckling capacity. The influence of the radial end conditions is reduced as the length to diameter (L/D_p) ratio of the pipe used for testing is increased. However, testing a very long pipe (e.g. $L/D_p > 10$) would require the use of a very long test cell, which was not feasible for this experimental program. On the other hand, an attempt was made to keep the pipe ends free to deform radially, but a seal could not be developed that was able to provide a seal at high pressures while allowing radial deformations.

The effects of radial constraints on the circumferential stress in the pipe were analyzed for a pipe radially constrained at the ends and with a length to diameter ratio (L/D_p) equal to three. It was found that throughout 70 percent of the length of the pipe the circumferential stress had the same magnitude than the case when the ends are free in the radial direction. Based on these results it was decided to use a pipe with a length to diameter ratio equal to three.

It is possible that the buckling capacity of the pipe is affected by the end radial conditions but it was not possible to calculate the magnitude at which the buckling capacity was affected. Although some influence of the end conditions was expected on the buckling capacity, the mechanism of buckling could still be studied for pipes under ground and fluid loads.

Axis-symmetric finite element analyses were conducted in WANFE® (Moore 1996) to calculate the effects of possible restraints in the radial and axial directions at the pipe ends. Figure 3.2 shows the dimensions of the pipe and the load applied for the analyses. Figure 3.2 (a) is a plan view of a pipe with internal diameter $D_{pi} = 260$ mm, thickness $t_p = 10$ mm and pressure $q = 1$ MPa acting radially on the external pipe wall. Figure 3.2 (b) is the elevation view of the pipe of length $L = 780$ mm. The length to diameter ratio for this analysis was equal to 3. Linear elastic finite element analyses were performed with a pipe modulus $E_p = 200$ MPa and a Poisson's ratio $\nu_p = 0.46$. The analyses were conducted with radial and axial deformations fixed and free at the ends of the pipe (i.e. at $z = L/2$). In Sections 3.4.1 to 3.4.3, the possible selections for radial and axial end conditions are analyzed. Figure 3.3 shows the results of the finite element analysis conducted with the program WANFE® (Moore 1996) for different radial and axial end conditions of the pipe. See Table 3.1 for a summary of each condition.

3.4.1 Unrestrained radial deformations

Keeping the ends of the pipe free (i.e. unrestrained) to deform in the radial direction is beneficial in that the response of the pipe is not altered. Figure 3.3 shows that the circumferential stresses are uniform throughout the length of the pipe for the case when pipes ends are allowed to deform radially. From these observations it can be inferred that the buckling resistance is not affected.

However, it is difficult to seal the pipe ends under high fluid pressures while allowing radial pipe deformations. Section 3.4.1.1 describes different attempts to implement seals that would allow radial deformations at the pipe ends during the tests.

3.4.1.1 Seal configurations tested

The following is a description of tests on two different seal configurations in order to verify the applicability of the seals to the test program. Tests with external fluid pressures were carried out and the maximum fluid pressure at which sealing was attained was recorded. It was found that the seals tested were not capable of achieving an effective sealing action at pressures higher than 400 kPa making the tested seals not suitable for the test program. Table 3.2 summarizes the seals tested.

a) Rubber sheets

Several attempts were made using rubber sheets at the pipe ends to obtain end seals that allowed radial deformations. One rubber sheet was

compressed between the test cell lid and the pipe top end. The other rubber sheet was compressed between the bottom pipe end and the base of the cell. This arrangement was effective sealing the external pore pressures to approximately 100 kPa. Figure 3.4 shows the described arrangement as tested.

b) Boot and Welch seal

The seal by Boot and Welch (1996) consists of a ring of rubber in which the internal diameter is expanded until it fits tightly to the pipe. The seals used by Boot and Welch (1996) at the ends of liners used in experiments allowed radial deformations therefore the buckling pressures obtained in their tests were not affected by the end conditions. However the highest fluid pressures applied by Boot and Welch were only 276 kPa.

A seal test was performed in order to attempt the implementation of this seals (by Boot and Welch) in the test program. The seal was installed at the end of an HDPE pipe encased in a concrete pipe. Figure 3.5 shows a photograph of the pipe and seal arrangement. At approximately 400 kPa, leakage started to occur. Therefore the seals were not implemented because it was expected to apply pore pressures higher than 1000 kPa. It was not possible to develop seals that allowed radial deformations of the pipe ends while efficiently sealing at pore pressures higher than 1000 kPa.

3.4.2 Restrained radial deformations

Restraining the radial deformations of the pipe ends affects the stress distribution through part of the pipe length. Figure 3.3 shows calculated circumferential stresses along the length of the pipe for the end condition of displacements fixed in the radial r direction but free in the axial direction of the pipe. For $0 \leq 2z/L \leq 0.70$ the normalized circumferential stresses $\sigma_{\theta\theta}/q$ have the same magnitude than the case of a pipe with ends free to deform radially. For $0.70 \leq 2z/L \leq 0.82$ the normalized circumferential stress $\sigma_{\theta\theta}/q$ increases 4 percent. Finally, for $0.82 \leq 2z/L \leq 1.0$ the circumferential stress ratio decreases about 95 percent. Therefore the results revealed the importance of placing the instruments between $0 \leq 2z/L \leq 0.70$ in order to measure deflections representative of a long pipe.

End radial restraints could affect the buckling capacity of the pipes. Moore (1998) compared the predictions made by Glock's equation (Equation 2.22) and the results of buckling tests made on encased liners that had clamped ends and different length to diameter ratios. The comparison showed that the buckling capacity approached that of a long pipe as the length to diameter (L/D_p) ratio increased. Hall and Zhu (2000) investigated the influence of constraints ends on the buckling capacity by performing three dimensional finite element analyses. A liner with clamped ends inside a rigid host was modeled for different values of L/D_p . It was found that an L/D_p equal to three increases the buckling capacity by approximately 10%. The analyses performed by Hall and Zhu (2000) give an upper bound of the effect of having

constrained radial ends on the buckling capacity because the influence of shear stresses from the soil is neglected. Using soil and thus having effective stresses acting on the flexible pipe probably lowers the effect of constrained ends on the buckling capacity.

Although the buckling capacity is expected to increase with end seals that constrain the pipe radial deflections, the pipes are easy to seal for high fluid pressures when radial deformations are not allowed. A seal could be made by welding a high-density polyethylene plate to the pipe or by using bolted flanges. Details of the seals are presented in Chapter 4.

3.4.3 Effect of restraints in the axial direction

Restraining the axial deformations at the ends of the pipe does not influence the circumferential stresses in the pipe. Figure 3.3 shows that the case with radial and axial restraints at the ends of the pipe (Fixed in r , Fixed in z) has the same circumferential stress distribution as that for the case that is restrained radially but free to deform axially at the end of the pipe (Fixed in r , Free in z) for $2z/L$ less than 0.70. This occurs because the circumferential stress in the pipe is statically determinate when subject to uniform external radial stress q . The magnitude of circumferential stress varies slightly between both cases from $2z/L = 0.70$ to $2z/L = 1.0$ but the trend of decreasing circumferential stress is similar.

Keeping the pipe free to deform axially was the easiest end condition to implement in the test program. As it is described in Chapter 4, sand was

placed between the top of the pipe and the test cell lid. Between the sand and the test cell lid an intentional 5 mm gap was left for purposes of sealing the test cell. Consequently the pipe was able to deform in the axial direction.

3.4.4 Summary

Seals that constrained the end radial deformations were used for pipes that had a length to diameter ratio equal to three. The analyzed effects of radial constraints on the circumferential stresses led to the conclusion that the pipe deformations had to be measured in the central section of the pipe (mid-height) where the influence of the radial restraints is the least.

For the tests it was decided to allow the pipes to deform axially because it is the easiest condition to implement and the axial constraints does not affect the circumferential stresses. The importance of axial boundary conditions on the interpretations of results will be discussed in more detail in Chapter 6.

3.5 Test cell description

A vertical section through the test cell is presented in Figure 3.6. The pipe is centered inside the cell and a rubber bladder applies pressure to the entire vertical length of the soil. The bladder is attached between the test cell body and the top and bottom flanges. This arrangement served to seal the internal pressures of the test cell. The internal vertical clearance of the cell is 1000

mm and the internal diameter is 600 mm. Figure 3.7 is a photograph of the test cell.

The top flange has four ¼" NPT (National Pipe Thread) ports in order to pressurize and measure the pore fluid, and for the installation of leak-proof fittings for the instrumentation cables. The test cell body, which is the main vertical cylinder, has two ½" NPT ports which are diametrically opposed. One of them serves to pressurize the bladder and the other to measure this magnitude.

The maximum internal working pressure of the test cell is 3000 kPa. The test cell was proof tested to 4500 kPa by the fabricator. The specifications provided by the fabricator are presented in Appendix A.

3.6 Test cell design

The design considerations for the new test cell are presented in the following section.

3.6.1 Test cell internal diameter

The internal diameter of the test cell depends on the external diameter of the pipe and backfill thickness to be used for the tests. The backfill thickness had to be at least equal to the radius of the pipe in order to minimize the effects of having a non-uniform backfill. According to results presented by Moore et al. (1994) for the buckling capacity of flexible cylinders with non-uniform support, the smaller dimension of the backfill should be equal or larger than the radius

of the pipe in order to avoid any minimization of the buckling capacity of the structure. It was decided to use a commercially available pipe with an external diameter pipe of 273 mm. Consequently the backfill thickness had to be at least 137 mm making the minimum internal diameter of the test cell equal to 540 mm. Therefore the test cell body consisted of a commercial steel pipe that had an external diameter of 610 mm and an internal diameter of 577 mm.

3.6.2 Test cell internal vertical clearance

The internal vertical clearance (height of the test cell body) of the test cell should be enough to contain the length of the pipe samples used for testing. In Section 3.4, arguments were presented that justified the use of a pipe with length to diameter (L/D_p) ratio equal to three thus this ratio was implemented. In Section 3.6.1 the chosen external pipe diameter was 273 mm therefore the pipe length should at least be three times the diameter, which is equal to 820 mm. Therefore it was decided to use a test cell with an internal vertical clearance of 1000 mm.

3.6.3 Pressure requirements based on available buckling solutions

The test cell parts had to be designed in order to withstand the maximum internal pressure that was going to be applied during the test program. During the early stages of the test cell design the value of maximum pressure that was going to be applied was unknown. Available buckling solutions were used in order to obtain a preliminary estimate of the applied pressures.

It was considered that the multiwave buckling solution (Equation 2.21) that models the soil as a continuum represented an upper boundary to calculate the buckling capacity of the pipe. The buckling capacity was calculated for a pipe with thickness $t_p = 8.4$ mm and pipe modulus $E_p = 960$ MPa. The soil parameters used were $E_s = 35$ MPa and Poisson's ratio $\nu_p = 0.25$. The calculated critical buckling pressure P_{cr} acting on the pipe was equal to 2088 kPa. Using the arching solution by Hoeg (1968) it was found that a 2000 kPa of bladder pressure P was needed to transmit 2088 kPa to the pipe. All the calculations assumed that the pore pressures, u , was zero. It was decided to design a test cell capable of withstanding an internal pressure of 3000 kPa.

3.7 Summary

In this Chapter, the basic test concept and the development of the test facility was presented. For the first time, test can be conducted on pipes under ground and fluid loads at pressures as high as 3000 kPa with the new test cell.

One of the most important aspects of the experimental design was the consideration of the end conditions. It was intended to perform tests with the ends of the pipe free to deform in the radial direction but seal tests demonstrated that under this condition it was not possible to seal at high pressures. Therefore the pipes had to be sealed while constraining the pipe radial deformations.

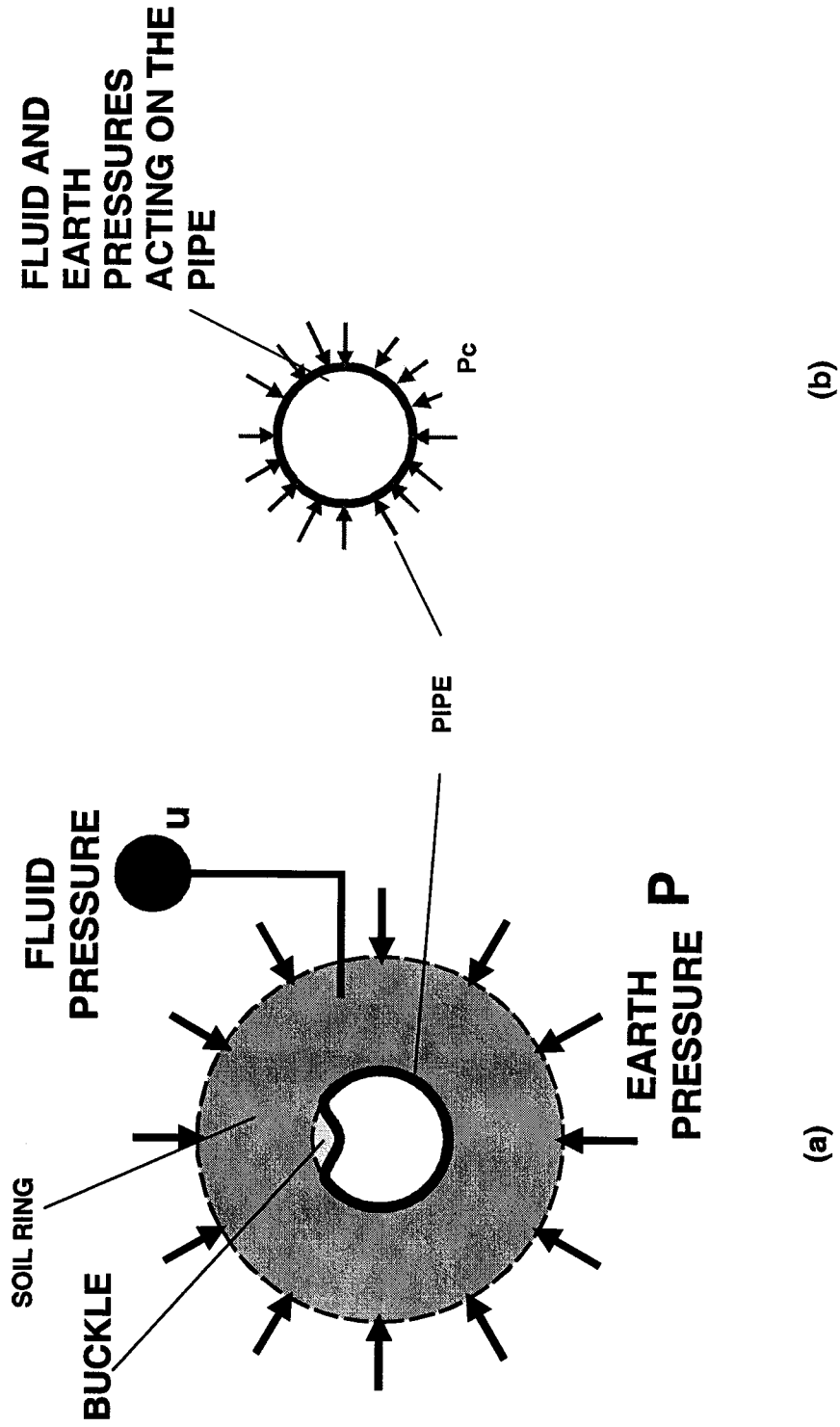
In order to limit the boundary effects tests had to be performed with very long pipes (e.g. $L/D_p > 10$) but this would have required a very long test cell. It is expected an increase of the buckling capacity, by a maximum of 10%, due to having the ends of the pipe constrained in the radial direction.

RADIAL DEFORMATIONS AT THE END OF THE PIPE	AXIAL DEFORMATIONS AT THE END OF THE PIPE	COMMENTS
FREE	FREE	<ul style="list-style-type: none"> • RADIAL CONDITIONS DO NOT AFFECT THE CIRCUMFERENTIAL STRESS IN THE PIPE AND THE BUCKLING RESISTANCE • THIS AXIAL CONDITION IS EASIER TO IMPLEMENT AND DOES NOT AFFECT THE CIRCUMFERENTIAL STRESS • DIFFICULT TO SEAL
FIXED	FIXED	<ul style="list-style-type: none"> • RADIAL CONDITIONS AFFECT THE CIRCUMFERENTIAL STRESS IN THE PIPE AND THE BUCKLING RESISTANCE • THIS AXIAL CONDITION DOES NOT AFFECT THE CIRCUMFERENTIAL STRESS • IT IS POSSIBLE TO SEAL

TABLE 3.1 SUMMARY OF THE POSSIBLE END CONDITIONS THAT WERE CONSIDERED DURING THE DESIGN OF THE EXPERIMENT. THE ADVANTAGES AND DISADVANTAGES OF THE DIFFERENT END CONDITIONS ARE GIVEN

SEALS USED	MAXIMUM EXTERNAL FLUID PRESSURE AT WHICH SEALING WAS OBTAINED (kPa)	COMMENTS
RUBBER SHEETS COMPRESSED BETWEEN THE PIPE ENDS AND THE TEST CELL	100	REQUIRES THAT THE PIPES SHOULD BE CUT AT A LENGTH ALMOST EQUAL TO THE INTERNAL VERTICAL CLEARANCE OF THE CELL TO OBTAIN AN EFFECTIVE COMPRESSION OF THE RUBBER SHEETS
SEALS USED BY BOOT AND WELCH	400	THE EFFICIENCY OF THE SEAL IS LIMITED BECAUSE THE SEAL MATERIAL (RUBBER) CANNOT BE BONDED TO THE POLYETHYLENE PIPE

TABLE 3.2 SUMMARY OF THE SEAL CONFIGURATIONS TESTED THAT ALLOW RADIAL DEFORMATIONS AT THE ENDS OF THE PIPE



(a)

(b)

FIGURE 3.1 (a) PLAN VIEW OF THE SOIL AND PIPE WITH THE BLADDER AND PORE PRESSURE ACTING ON THE SYSTEM, (b) FLUID AND EARTH LOADS ACTING ON THE PIPE

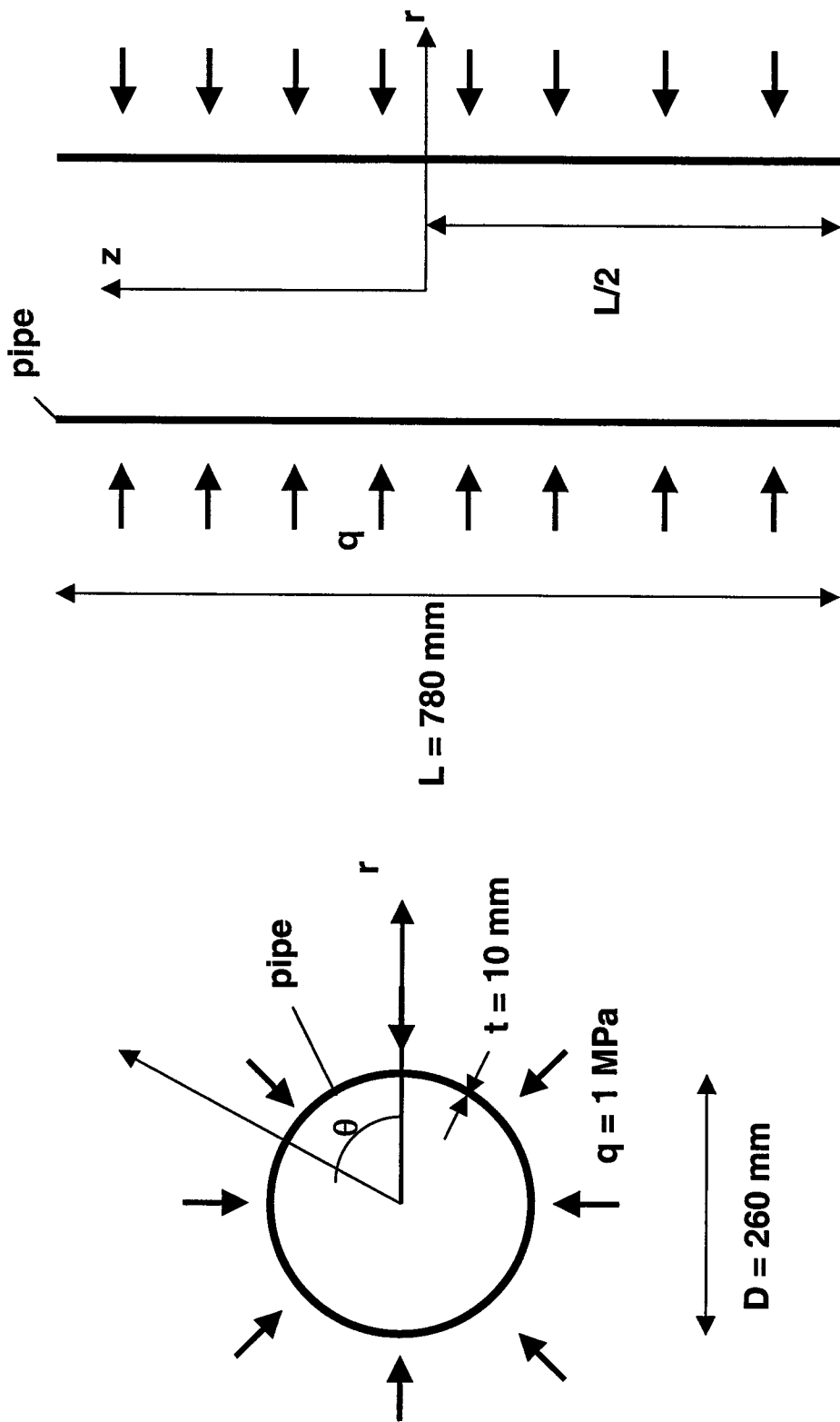


FIGURE 3.2 (a) PLAN VIEW OF THE PIPE MODELED IN THE FINITE ELEMENT ANALYSIS, (b) ELEVATION VIEW OF THE PIPE MODELED

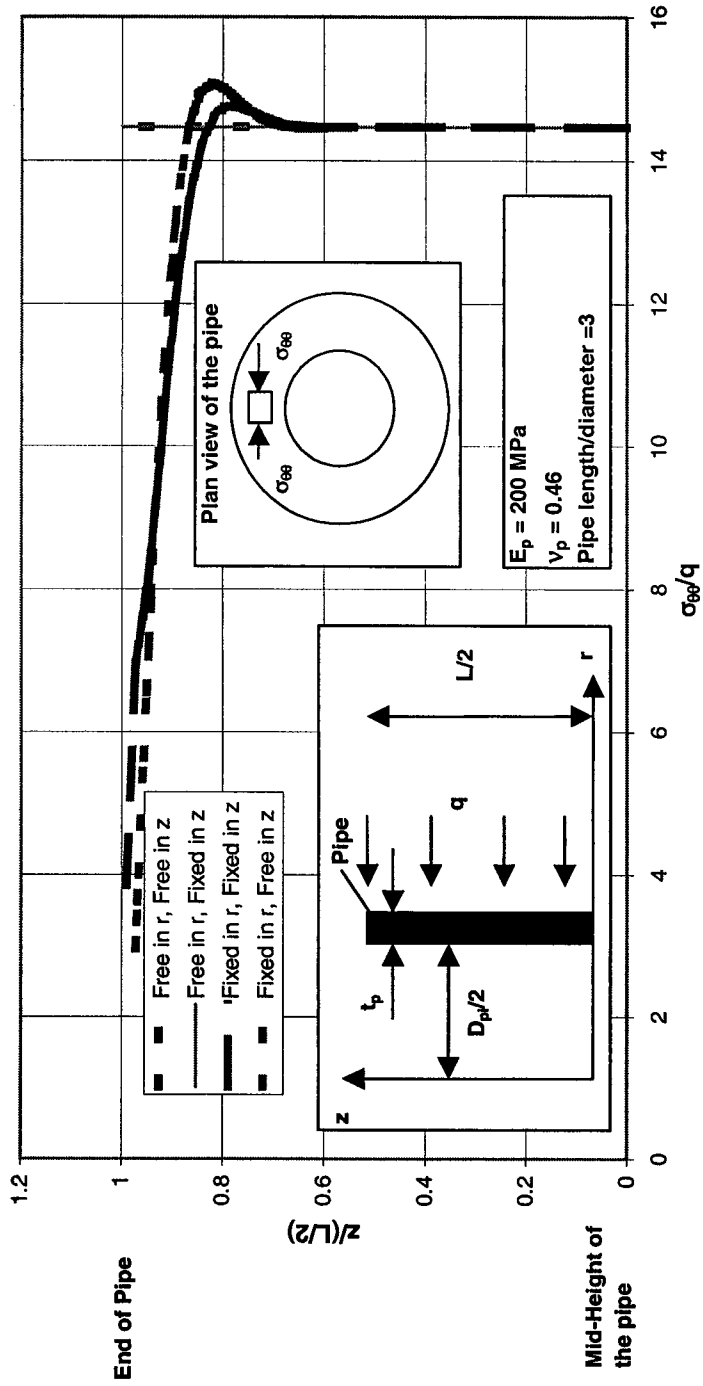


FIGURE 3.3 INFLUENCE OF RADIAL AND AXIAL RESTRAINTS AT THE END OF THE PIPE ON THE CIRCUMFERENTIAL STRESS IN THE PIPE

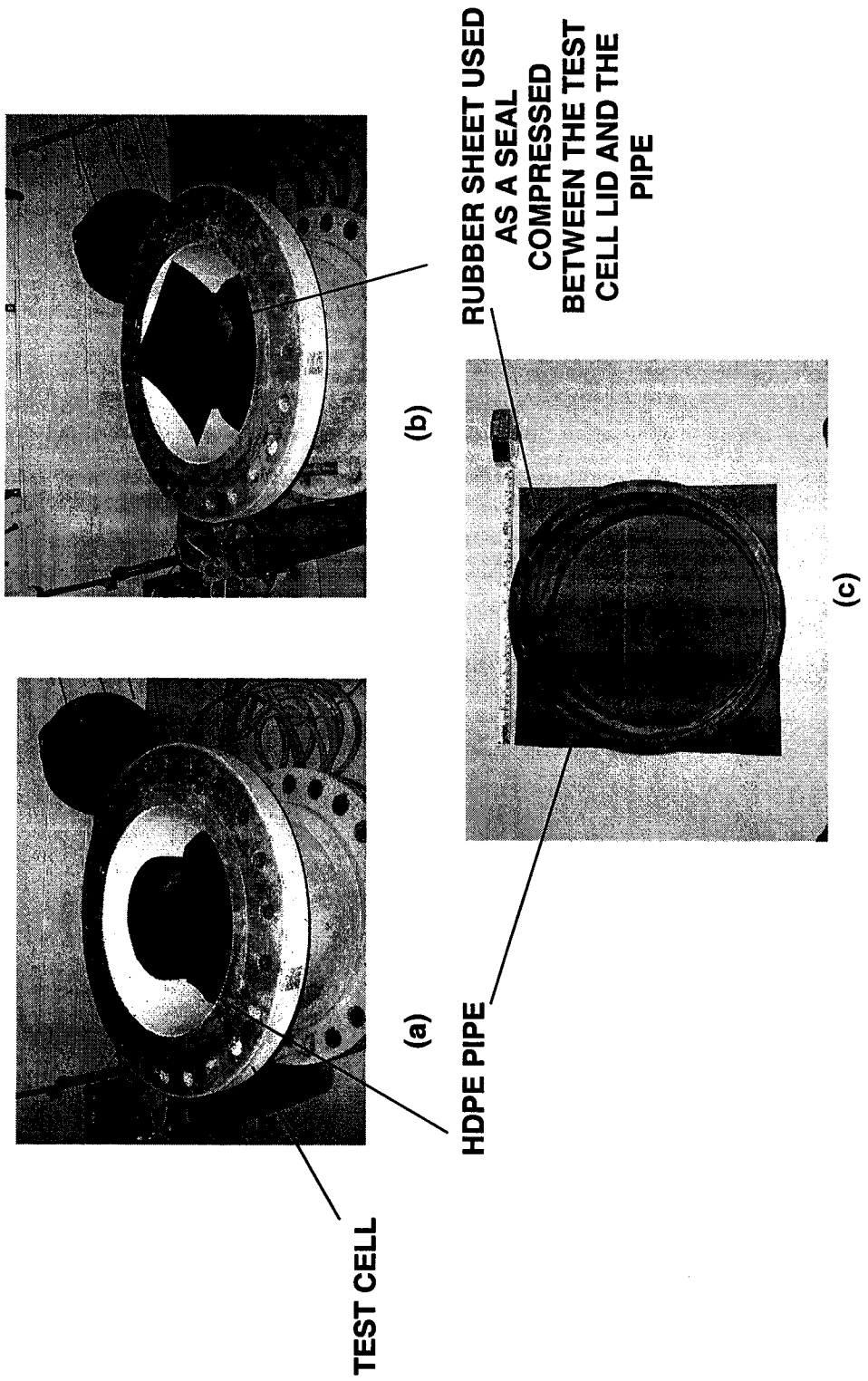


FIGURE 3.4 PHOTOGRAPHS SHOWING THE TESTED SEAL THAT COULD HAD KEPT THE END OF THE PIPE FREE TO DEFORM RADially (a) TEST CELL AND HDPE PIPE, (b) TEST CELL, HDPE PIPE AND SEAL, (c) PLAN VIEW OF THE HDPE PIPE AND SEAL

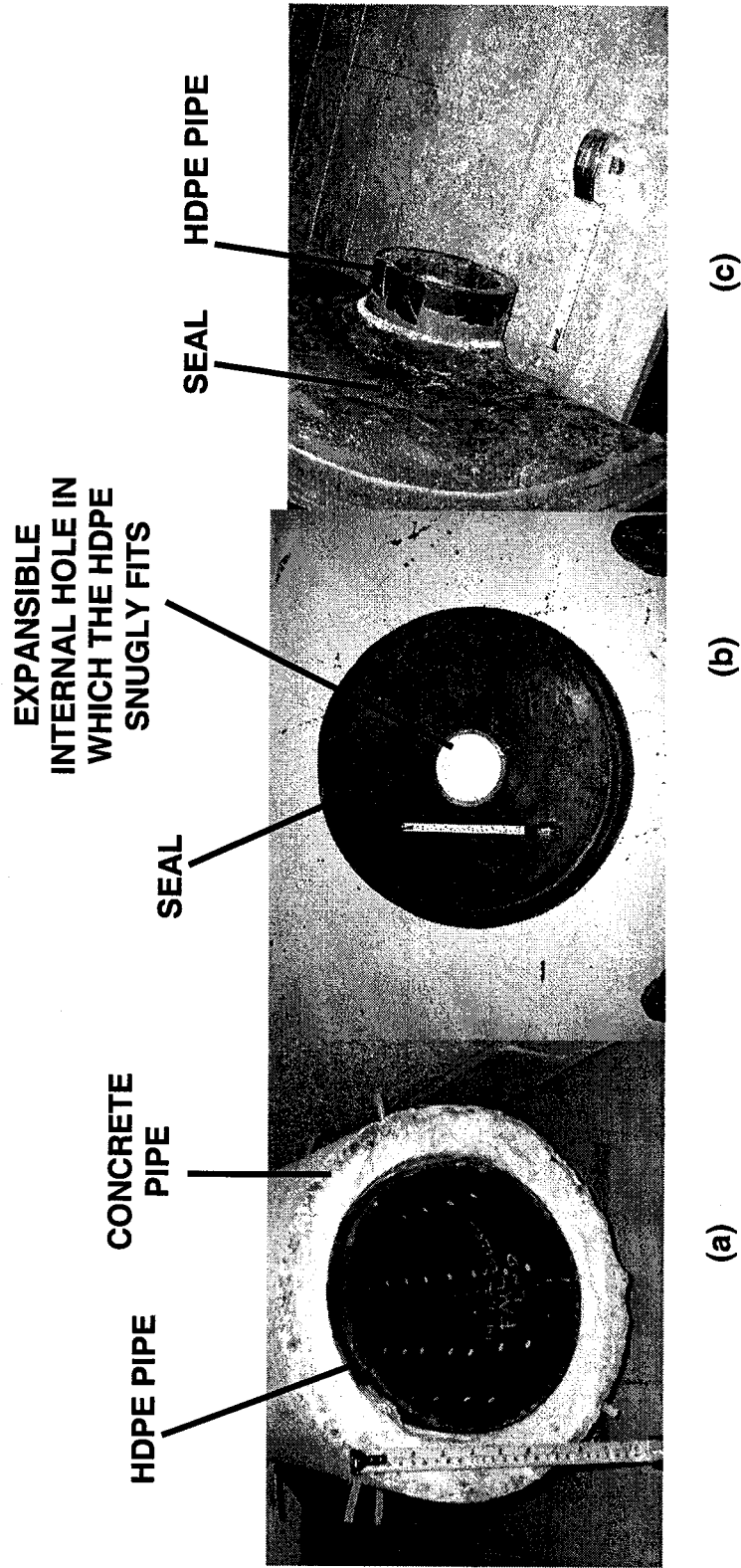


FIGURE 3.5 PHOTOGRAPH OF THE TEST WHERE THE SEAL USED BY BOOT AND WELCH
 WAS IMPLEMENTED (a) PHOTOGRAPH OF THE PIPE ENCASED INSIDE THE CONCRETE
 PIPE, (b) PHOTOGRAPH SHOWING A PLAN VIEW OF THE SEAL, (c) PHOTOGRAPH
 SHOWING THE SEAL INSTALLED IN THE PIPE

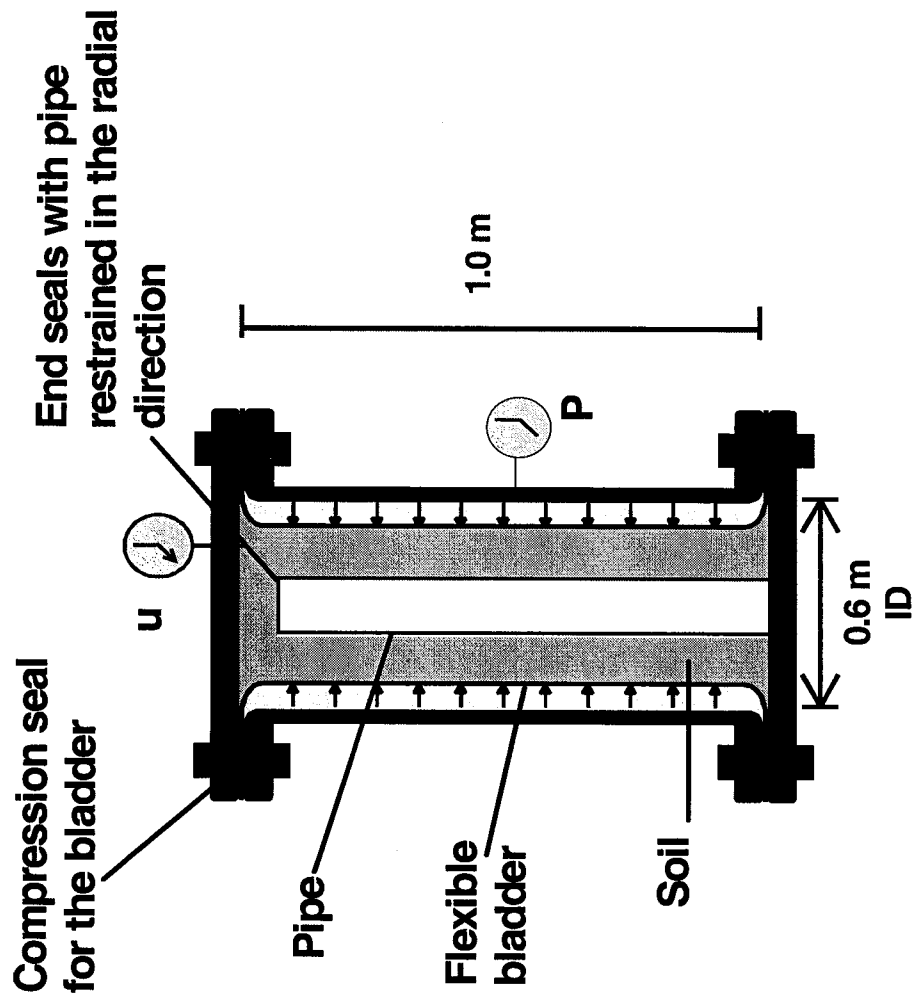
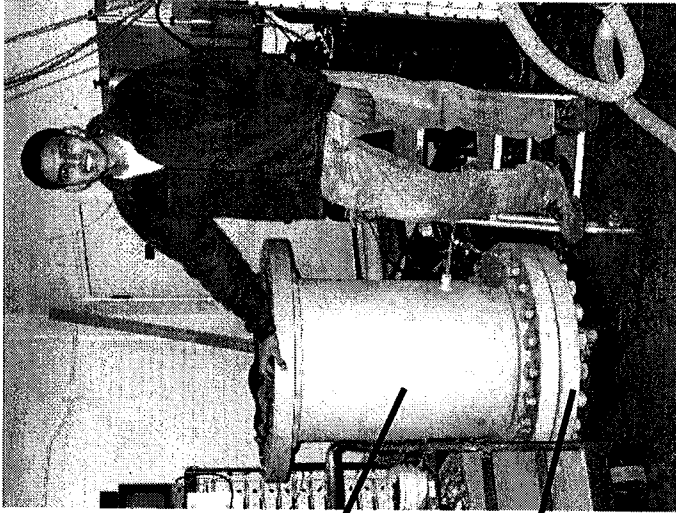


FIGURE 3.6 ELEVATION VIEW OF THE TEST CELL SHOWING THE PIPE, BLADDER AND SOIL RING



**TEST CELL
BODY**

**BOTTOM
FLANGE OF
THE CELL**

FIGURE 3.7 PHOTOGRAPH OF THE TEST CELL

4. Methodology

4.1 Introduction

The details of a new test cell developed to measure the buckling capacity of flexible pipes under earth and fluid pressures was provided in Chapter 3. In this Chapter, a description of the materials used in the test program, the procedures developed to conduct experiments in the new test cell, and the techniques that were developed to apply combined earth and fluid pressures are presented. This was the first time that these test were conducted therefore new procedures had to be developed.

4.2 Materials used

4.2.1 Pipe specimens

The tests were conducted on high-density polyethylene (HDPE) pipes that had an average external diameter of 273 mm. These pipes had a cell classification of PE 345434C in accordance with ASTM D3350 and Class PE 3408 according to the Plastic Pipe Institute.

The tests were conducted with two values of pipe thickness. Three pipes were 13 mm thick and the other three 8.4 mm thick. The thickness of a pipe is commonly expressed using the Dimension Ratio (DR), which is equal to the external pipe diameter divided by the pipe thickness. The 13 mm thick pipes had a DR of 21, and the 8.4 mm thick pipes had a DR of 32.5.

4.2.2 Geotextile

A geotextile was used to separate the gravel and sand materials and to protect the bladder from possible puncture by the gravel particles. It consisted of polypropylene non-woven needle-punched geotextile (brand name Amoco 4508) and had a mass per unit area of 271 g/m².

4.2.3 Gravel backfill

A ring of gravel was placed around the pipe in order to simulate the backfill placed around buried pipes and manholes. The ring had a thickness of approximately 160 mm extending in the radial direction from the external surface of the pipe to the rubber bladder.

The characteristics of granular soils (such as sand and gravel) are preferred for buried pipe installations. According to Selig (1990), coarse-grained soils are stable under long-term moisture changes, exhibit little creep and consolidation deformations, provide good drainage and have enough stiffness to limit the pipe deformations and enhance the buckling strength. Gravel was used for the tests because it was easier to saturate than sand and it is usually used around polymer manholes.

The gravel used for the tests was a poorly graded coarse gravel (GP) according to the classification given by ASTM D2487-93. Grain size analysis conducted according to ASTM 422-63 revealed that the gravel consisted of sub-angular particles that were 77% finer than 19 mm sieve size but all the material was coarser than the 9.5 mm sieve size. Figure 4.1 is the grain size

distribution curve for the backfill and Figure 4.2 is photograph of the soil grains. A value of specific gravity of the solid phase G_s equal to 2.64 was obtained by following the procedures given in ASTM C127-88.

The gravel was placed uncompacted for every test in order to minimize the support provided to the pipe from the soil and attain pipe buckling at pressures that the bladder and test cell could withstand. A consistent uncompacted soil density was achieved by dropping all the soil in the test cell from a constant height. The average dry density obtained for the tests was 1450 kg/m^3 . According to the specification given in ASTM D4254 – 91 the minimum density obtained for the gravel was 1428 kg/m^3 and following the specifications given in ASTM D4253 – 93 the maximum density for the backfill was 2200 kg/m^3 . It is important to acknowledge that in the field the soil may be compacted but because these tests were the first step to solve the problem of pipe buckling under ground and fluid loads it was decided to use uncompacted backfill.

4.2.4 Sand

A 50 mm thick layer of sand was placed around the bottom and at the top of the pipe. This ensured the confinement of the upper and lower ends of the rubber bladder in order to prevent its rupture when pressures were applied. The material used was a uniform fine sand (SP) according to the classification given in ASTM D2487-93 and its grain size distribution curve is shown in

Figure 4.3. The sand was placed uncompacted at the bottom and at the top of the pipe.

4.2.5 Rubber bladder

The rubber bladder consisted of a rubber cylinder of 500 mm in diameter and 1000 mm in length with flanges at both top and bottom that were 77 mm in length. The membrane had a thickness of 10 mm. The material used was natural gum rubber because it can withstand large tensile strains without mobilizing large tensile forces that could diminish the pressure applied to the soil.

4.3 Instrumentation used in the test program

4.3.1 Linear potentiometers

The measurement of pipe deflections was made using Novotechnik TR 50 linear potentiometers. The potentiometers had a mechanical stroke of 50 mm. Calibration was achieved by recording the voltage readings from the potentiometer at different stroke extensions. Figure 4.4 is a sketch of the potentiometers and the mounting brackets used to attach them to the pipe.

4.3.2 Infrared camera

An infrared camera was located inside the pipe to provide visual observations of the shape of the pipe during testing. The camera was a Subsea Video

System model S-60LPH/38 with dimensions 48 mm x 57 mm. The zoom and focus of the camera is fixed and the field of view is 76 degrees. The camera had eight infrared lights attached to it with a maximum range of 6000 mm. A card and software (brand name Hauppauge) were used to capture still images from the video recording. Figure 4.5 is a photograph of the camera.

4.3.3 Pressure transducers

Two pressure transducers were used to measure the bladder and pore pressure. The transducers used were AST 4410 models with a pressure range of 0 to 10000 kPa. The calibration consisted of comparing voltage readings and applied pressures in the range of 0 to 5000 kPa.

4.4 Experimental procedure

The following sections describe the procedures and details of the experiments, which are given in chronological order.

Step 1: Seal the bottom of the pipe

Seals were required at both ends of the pipe to permit the application of external fluid pressures without leakage. The base seal consisted of an HDPE plate welded by thermal fusion to the bottom of the pipe. A photograph of the bottom seal is given in Figure 4.6.

Step 2: Installation of instrumentation

The linear potentiometers and the infrared camera were installed. At least two linear potentiometers were located in the central section pipe (mid-height of the pipe). The two potentiometers were oriented perpendicular but if three potentiometers were used, the third one would have been installed at forty-five degrees of one of the potentiometers. The infrared camera was placed at the center of the top seal.

Step 3: Installation of the top seal

The top seal was different from the base seal to allow access to the inside of the pipe to install the instrumentation. The seal was constructed by first welding an HDPE flange to the pipe. Figure 4.7 shows the location of the welding bead of the pipe to the flange. A rubber gasket was then placed between the flange and a PVC cap. Figure 4.8 is a photograph of the PVC cap and the gasket. The PVC cap was then bolted to a steel ring located beneath the HDPE flange as it is shown in Figure 4.9. The instrumentation cables were passed through leak-proof fittings in the PVC cap.

Step 4: Bladder installation

The bladder was used to apply compressive radial pressures on the external soil boundary and also served to seal the test cell. The rubber used was natural gum rubber because of its capability to resist large strains. The rubber bladder consisted of a cylinder with flanges at both ends. The bottom

flange of the bladder was installed between the test cell and the bottom steel flange in order to seal the bottom of the cell. The top flange of the bladder was installed between the test cell body and a slip-on flange (steel ring) in order to seal the top of the cell. Following the installation of the bladder flanges, a vacuum pump was used to remove a gap between the bladder and the test cell wall (the bladder had a diameter of 508 mm and the test cell a diameter equal to 591 mm) resulting in an expansion of the bladder. The initial stretching of the bladder by expanding its diameter is beneficial from the perspective of the pressure capacity of the bladder.

Step 5: Backfilling

After installing the bladder and placing the pipe inside the cell, gravel was placed around the pipe. The procedure was as follows:

- a) Three geotextile layers were taped to the bladder in order to protect it from the gravel backfill.
- b) Sand was then poured around the pipe to a height of 50 mm in order to protect the bottom of the bladder.
- c) Gravel was deposited up to the level of the PVC cap. Figure 4.10(a) is a photograph looking at the test cell from above once all the gravel was placed.
- d) A layer of sand was placed on top of the pipe and gravel filling the test cell but a 5 mm gap was left between the top of the sand and the top of

the cell in order ensure sealing of the bladder. Figure 4.10(b) shows the completed backfill operation.

Step 6: Soil saturation

Once the backfill operation was completed the soil was saturated with water. Water was poured over the soil until complete saturation was achieved. De-aeration of the test cell was obtained by having the lid off during the operation.

Step 7: Supply of bladder fluid

The slip-on flange was removed from the top of the cell and the gap between the bladder and the cell was filled with water, which was the pressurizing fluid used for the bladder.

Step 8: Installation of the test cell lid

The steel lid of the test cell was placed on top of the steel flanges of the test cell body and then connected with twenty-four 35 mm diameter bolts. The instrumentation cables were passed through leak-proof fittings in the lid.

Step 9: Installation of the test cell instruments

The pressure transducer that measured the pore pressure was installed in the test cell lid and the other transducer used to measure the bladder pressure was installed in the test cell body. Figure 4-11 is a photograph of the lid with

the instrumentation. The setup of the test was now complete and was ready for the testing to commence.

4.5 Application of bladder and pore pressure

The pressurization of both the bladder and the pore fluid was achieved by means of a pumping system that was developed specifically for these tests. Figure 4.12 illustrates the components (Items A to E) and layout of the pumping system. A hydraulic jack (E) was used to displace the fluid of an oil-water interface (C). The interface (C) displaced water to the inside of the test cell in order to pressurize either the pore fluid or the bladder. The oil reservoir (D) was used to supply oil to the hydraulic jack (E). Several times during pumping, the water in the oil-water interface (C) was depleted and more water had to be added to the system. This was solved by means of an air-water interface (B) that was connected to an air regulator (A). The regulator (A) allowed the air to displace the water in the interface (B). Water was recharged from the air-water interface (B) to the oil-water interface (C). The overall result was the application of pressures as large as 3000 kPa to the test cell using a hydraulic jack.

4.6 Load path

The term load path refers to the sequence and duration that the bladder and fluid pressures were applied during the experiment. It was decided to conduct the tests at a constant applied effective bladder pressure ($P' = P - u$) at the

external soil boundary. First, the bladder pressure P was applied in steps (with the pore pressures u equal to zero) until the desired value of effective bladder pressure was reached. Then both the bladder pressure P and the pore pressure u were increased by the same amount resulting in an increase of pore pressures acting on the pipe at a constant effective stress P' at the external soil boundary. Figure 4-13 illustrates this concept.

The pressures were incremented in 100 kPa increments sustained for five minutes before proceeding to the next increment. Applying the pressures in equal increments resulted in a constant strain rate of the pipe, which facilitated the nonlinear viscoplastic analysis of the high-density polyethylene (HDPE).

4.7 Summary

In this Chapter, a description of the materials used in the test program, the procedures developed for the new test cell, the pumping system and load path of the applied pressures were presented. Details were given about the pipe specimens, geotextile, gravel, sand and the instrumentation used in the tests. The procedures for a test setup were then presented in chronological order. Finally, the pumping system and the load path of the applied pressures were described.

These new procedures were developed to conduct buckling tests under ground and fluid loads for the first time. The biggest challenge was the application of pressures as high as 3000 kPa, which demanded protective

measures for the bladder and sealing of the pipes and test cell. The pipes were sealed at both ends and the test cell was sealed using the top and bottom flanges of the rubber bladder.

In the following Chapter, results from a series of experiments conducted to measure the buckling capacity under ground and fluid loads are presented.

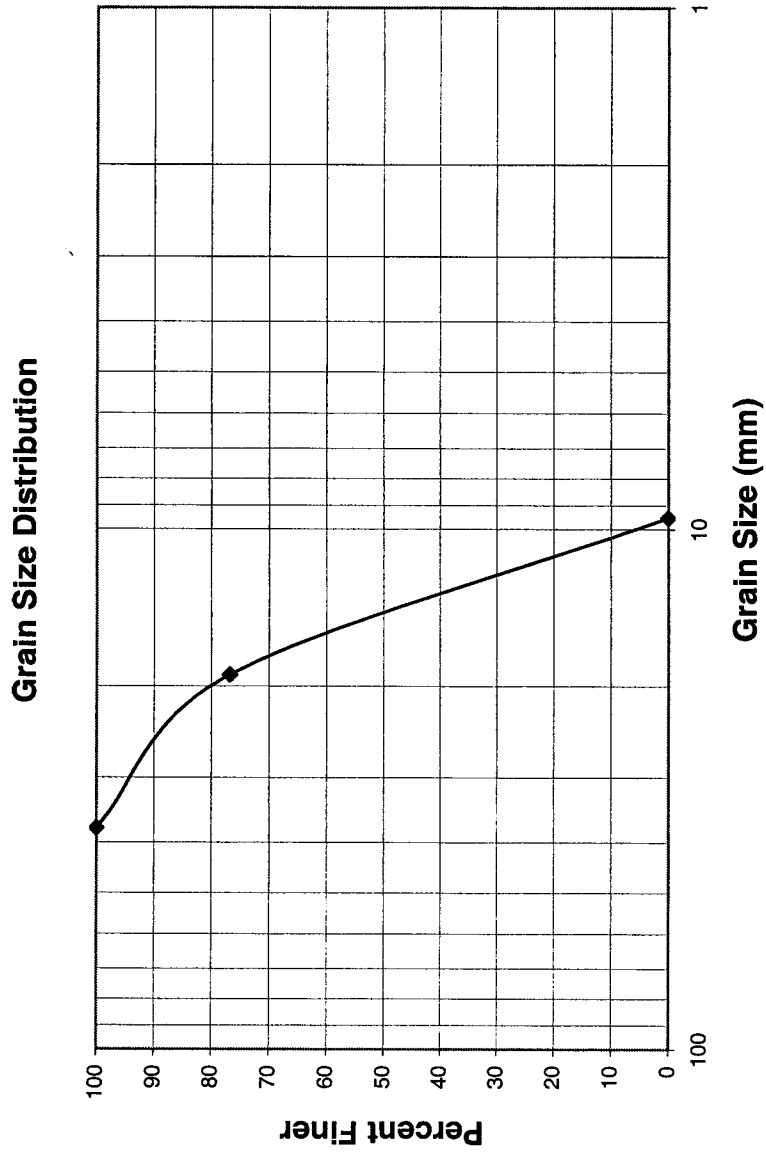


FIGURE 4.1 GRAIN SIZE CURVE FOR THE GRAVEL USED IN THE EXPERIMENTS



FIGURE 4.2 PHOTOGRAPH OF THE GRAVEL BACKFILL USED

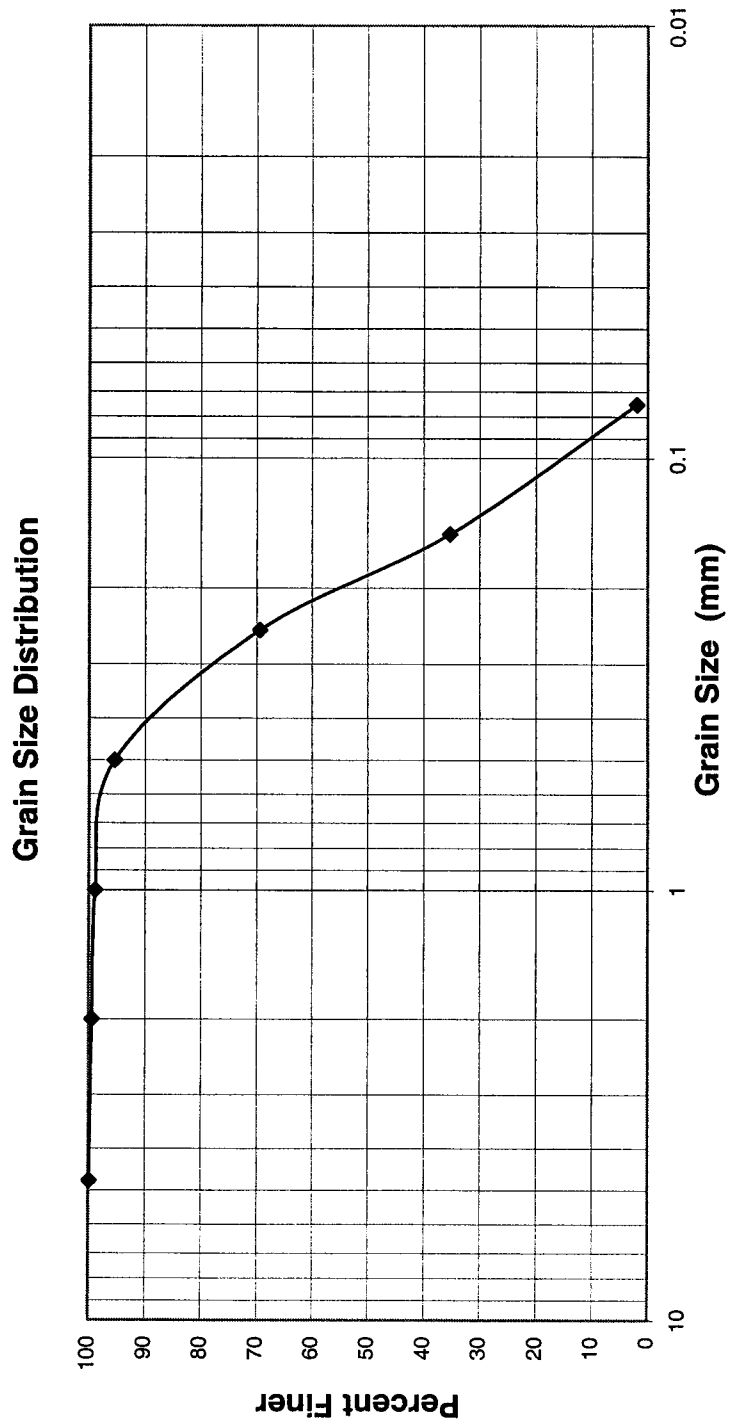


FIGURE 4.3 GRAIN SIZE CURVE FOR THE SAND USED IN THE EXPERIMENTS

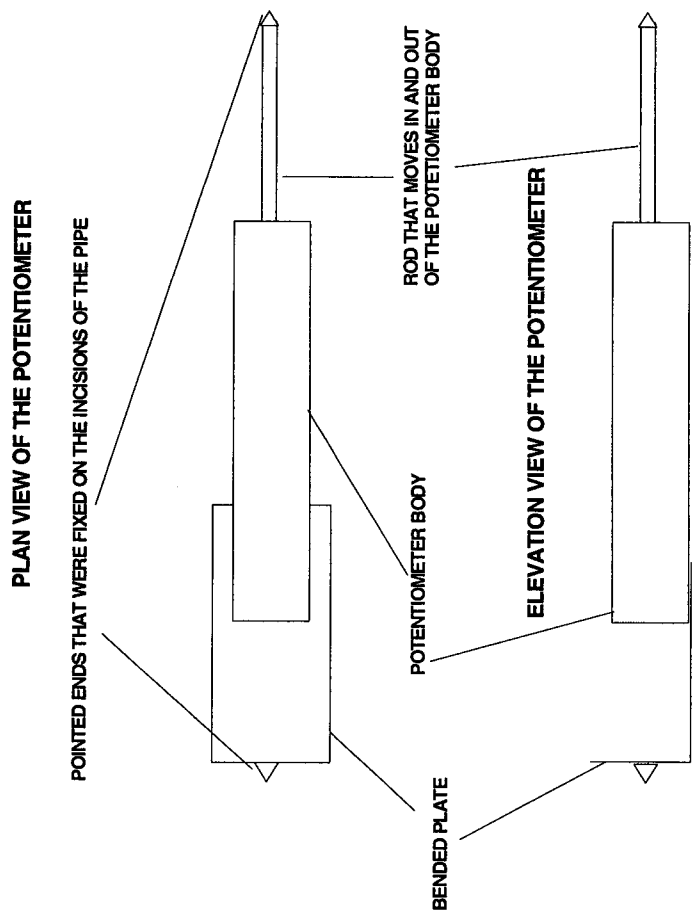


FIGURE 4.4 PLAN AND ELEVATION VIEW OF THE LINEAR POTENTIOMETERS USED TO MEASURE THE PIPE DEFORMATION

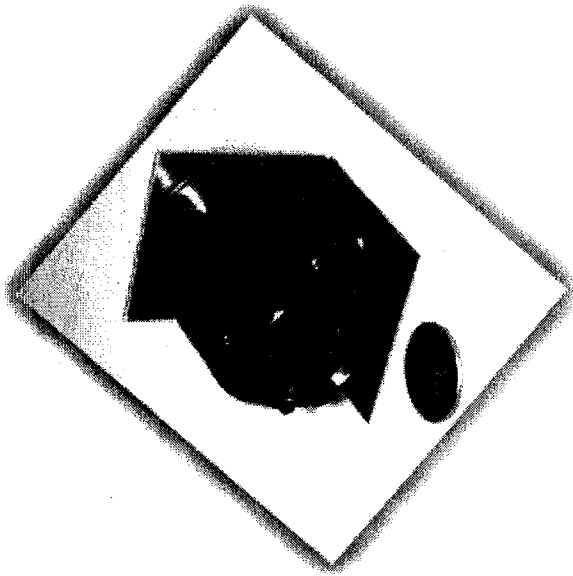
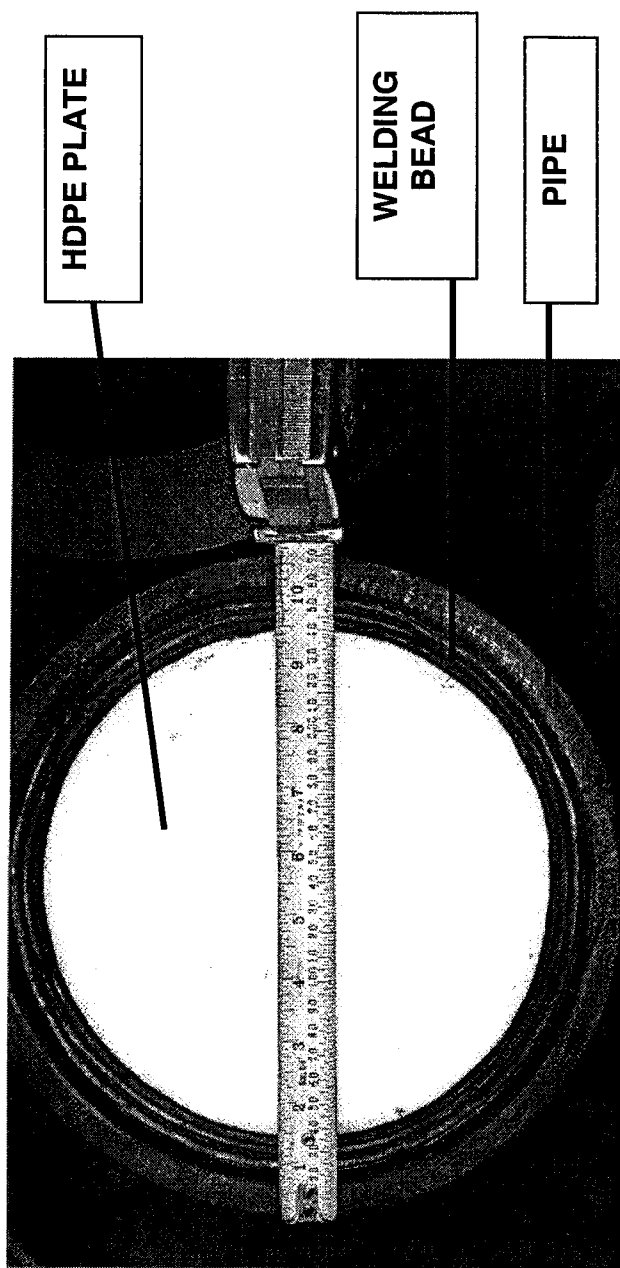
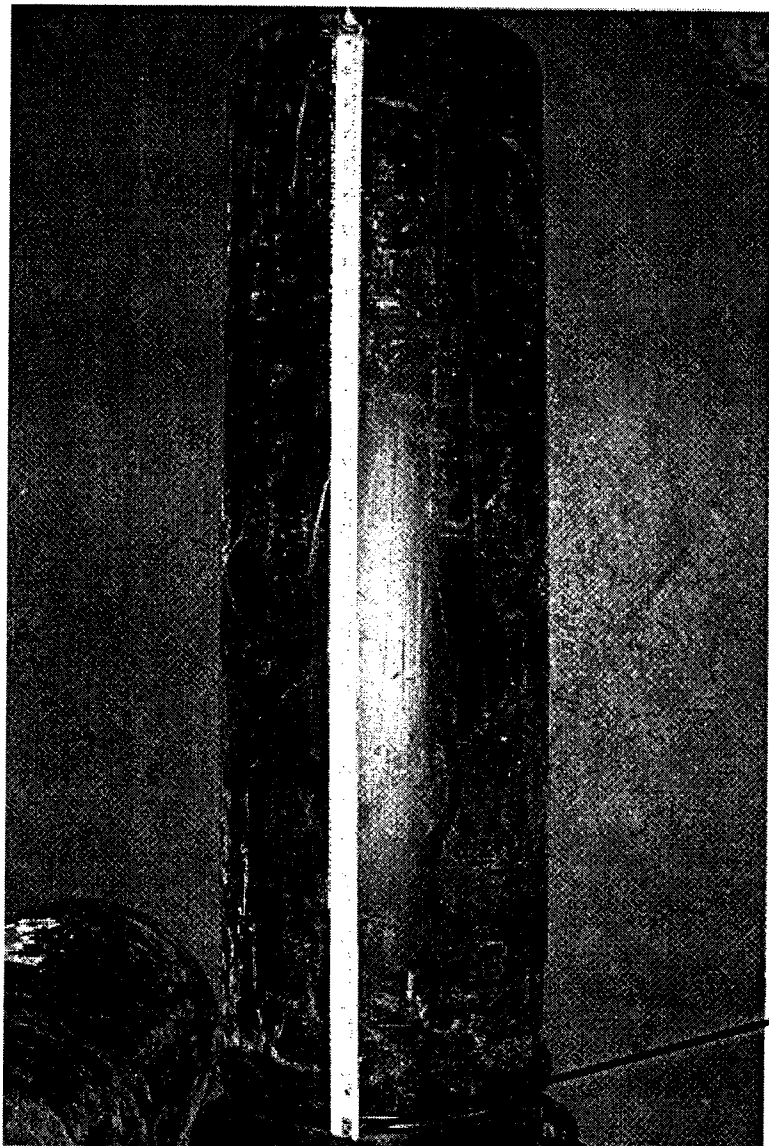


FIGURE 4.5 PHOTOGRAPH OF THE INFRARED CAMERA (TAKEN FROM SUBSEA VIDEO SYSTEMS)



Bottom part of the pipe

FIGURE 4.6 PHOTOGRAPH OF THE BOTTOM SEAL OF THE PIPE SHOWING THE HDPE PLATE WELDED TO THE PIPE



FLANGE

Top welding bead

FIGURE 4.7 PHOTOGRAPH OF ONE OF THE HDPE PIPES USED. THE PIPE HAD A LENGTH OF 83mm BETWEEN THE TOP WELDING BEAD AND THE BOTTOM PLATE WELDED TO THE PIPE

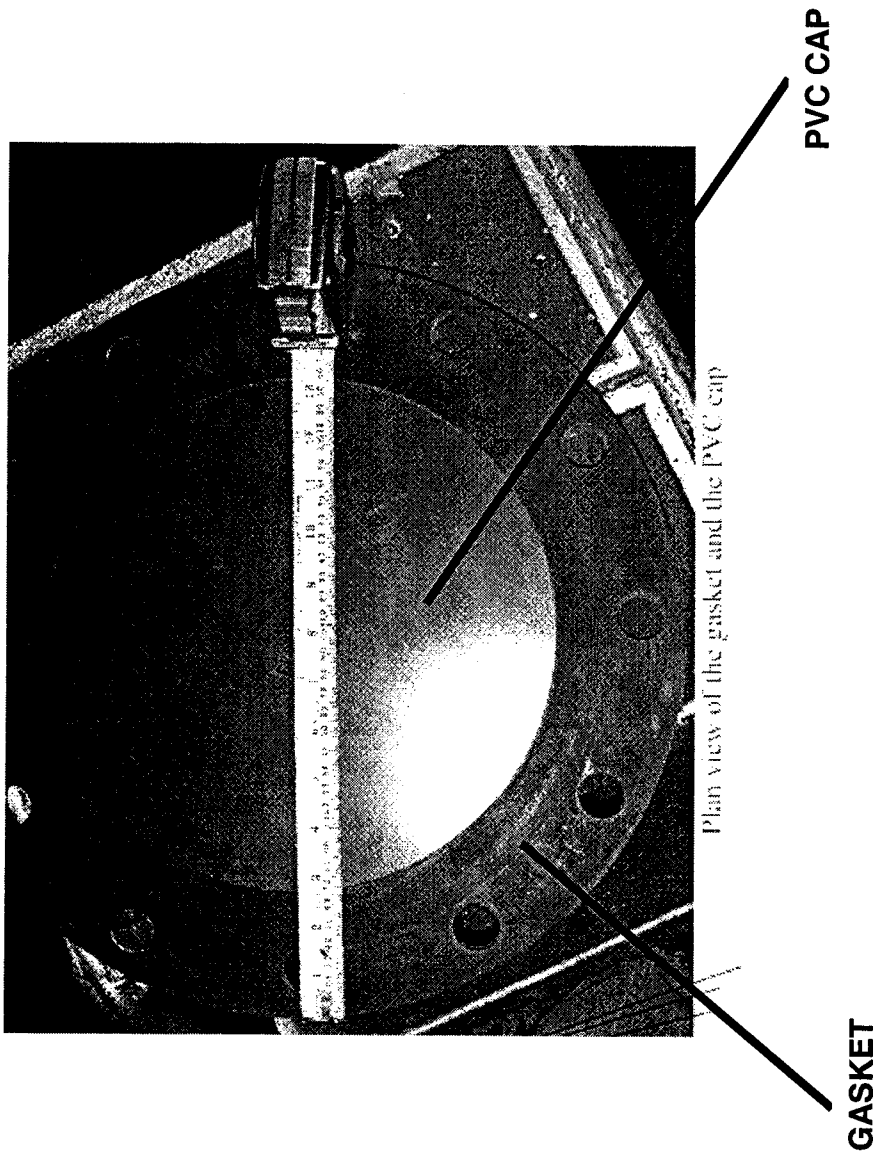


FIGURE 4.8 PHOTOGRAPH OF PVC CAP (203 mm DIAMETER) AND GASKET

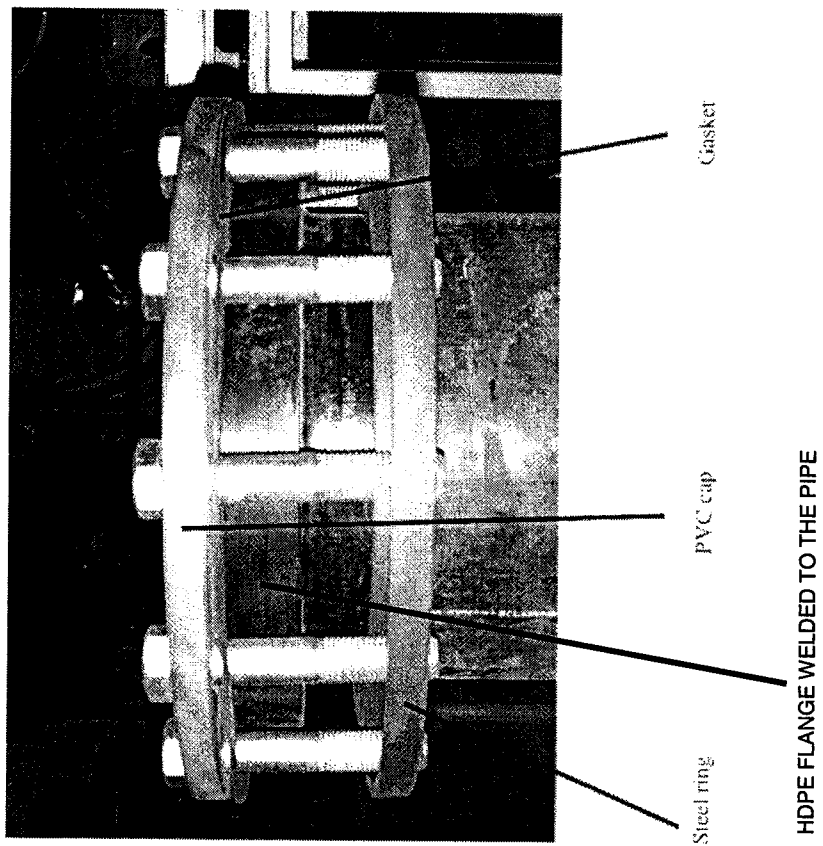


FIGURE 4.9 PHOTOGRAPH OF THE TOP SEAL OF THE PIPE SHOWING THE PVC CAP, STEEL RING, GASKET AND HDPE FLANGE

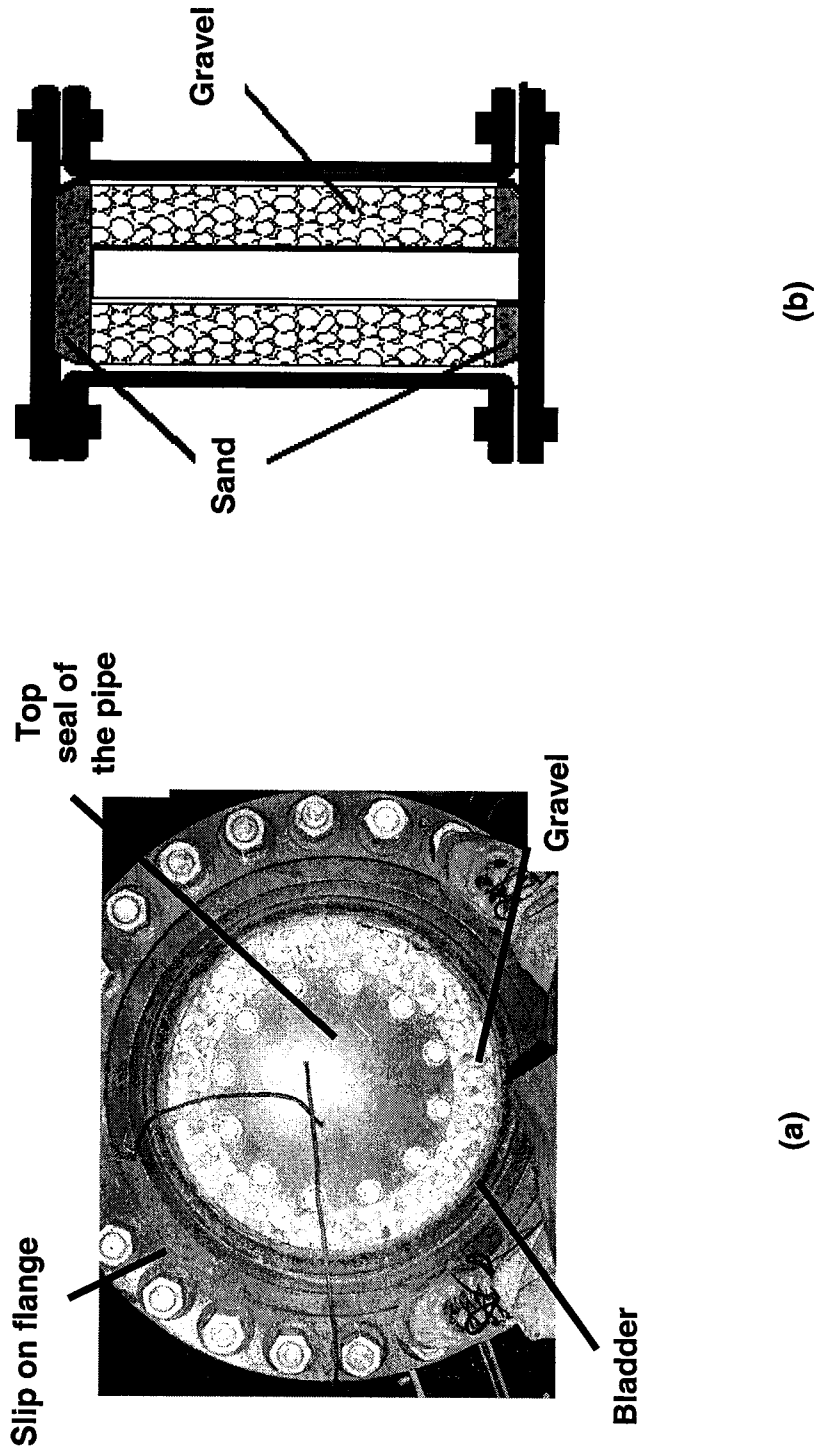


FIGURE 4.10 (a) PHOTOGRAPH SHOWING PLAN VIEW OF TEST CELL FOLLOWING COMPLETE BACKFILLING OF GRAVEL WITHOUT THE TOP SAND LAYER, (b) ELEVATION VIEW OF THE COMPLETED BACKFILLING OPERATION

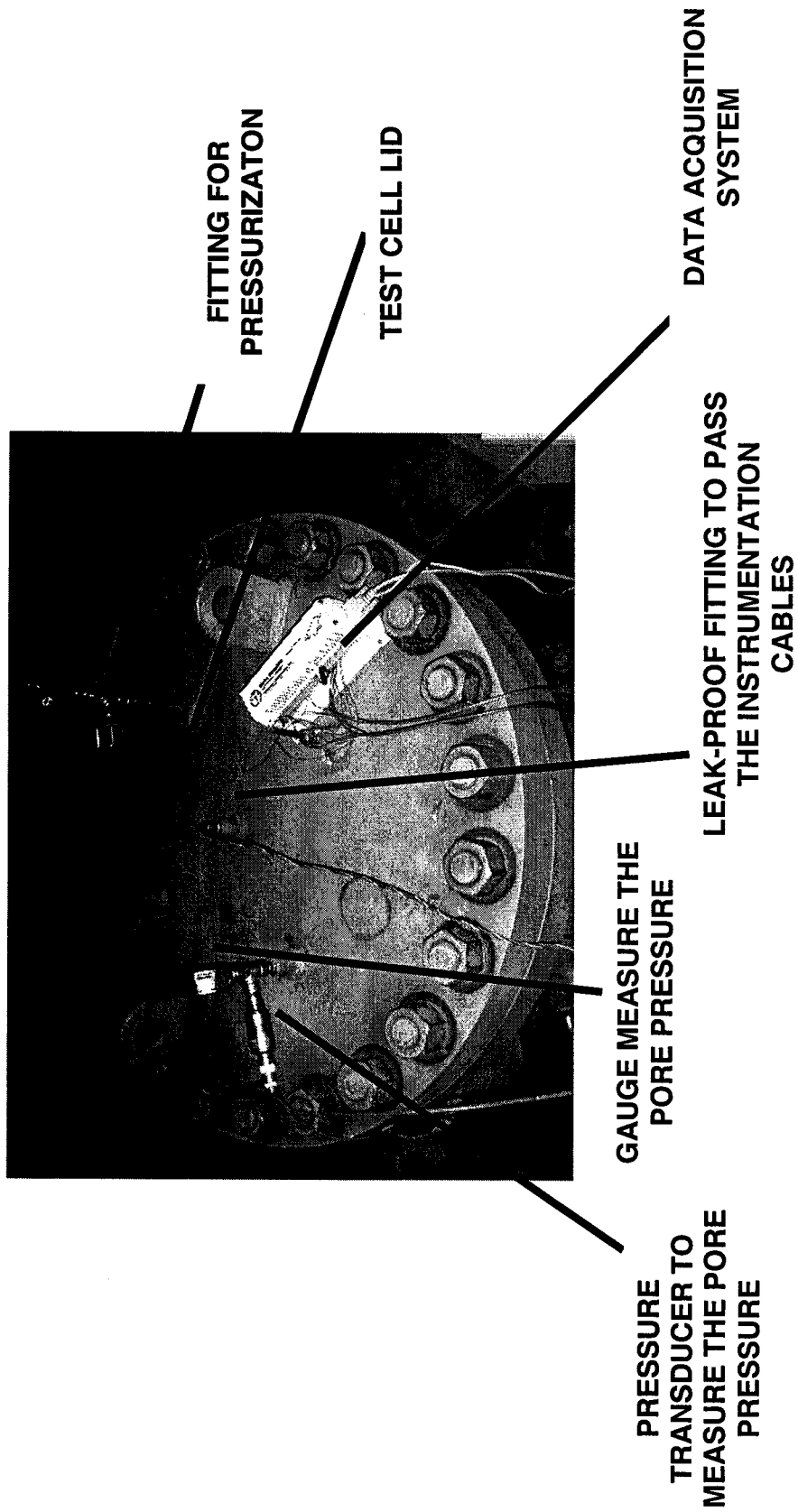


FIGURE 4.11 PHOTOGRAPH OF THE TEST CELL LID SHOWING THE PRESSURE TRANSDUCER AND THE GAUGE USED TO MEASURE THE PORE PRESSURE, THE LEAK-PROOF FITTING USED TO PASS THE INSTRUMENTATION CABLES, THE FITTING TO PRESSURIZE THE PORE FLUID AND THE DATA ACQUISITION SYSTEM

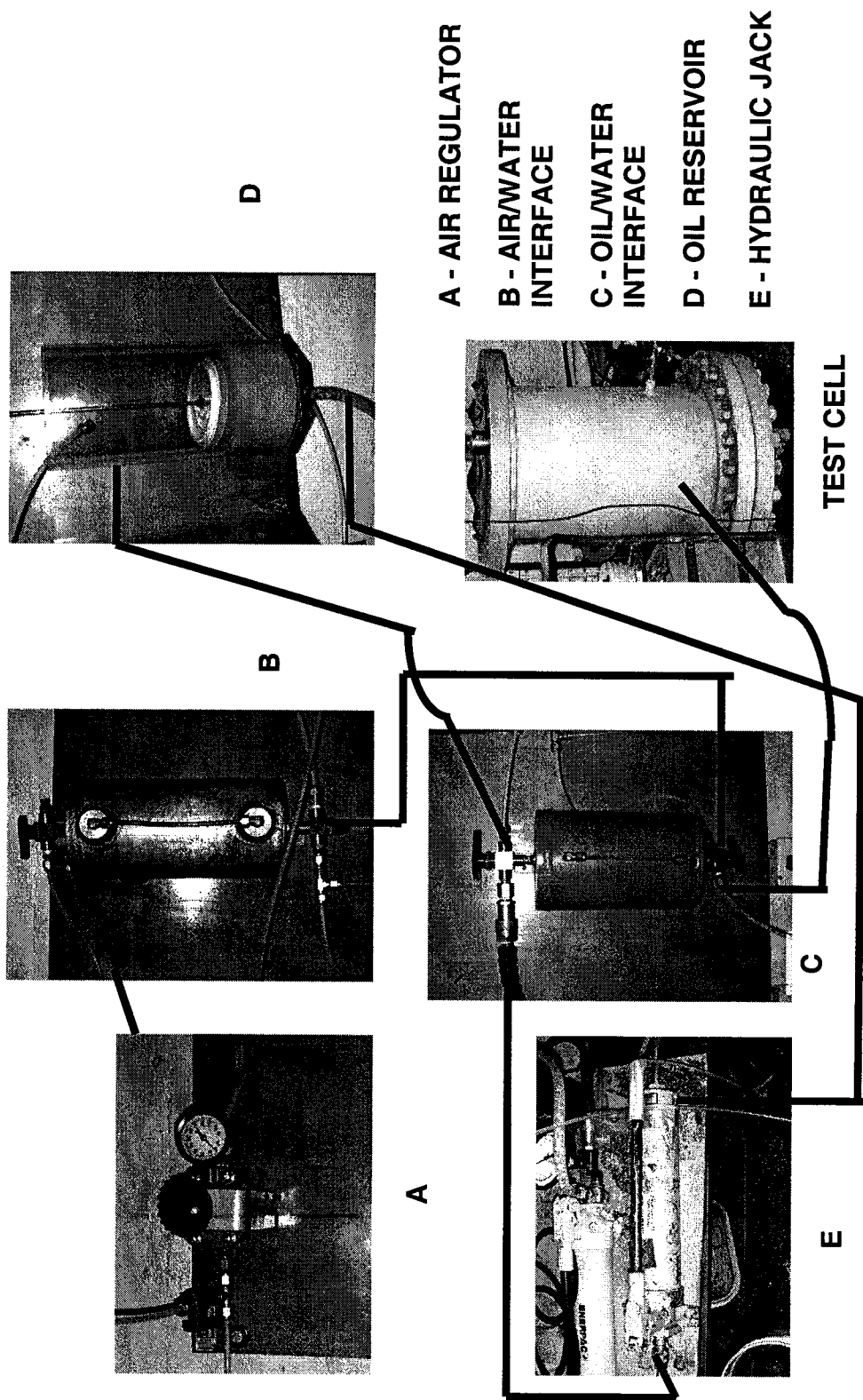
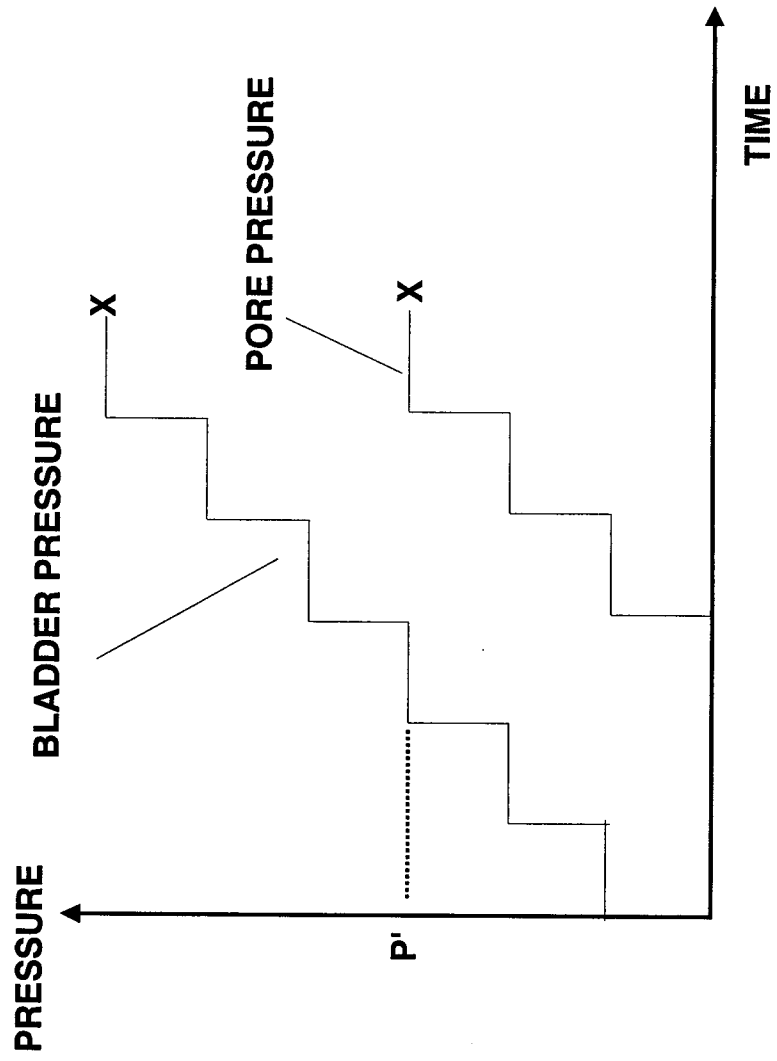


FIGURE 4.12 SKETCH SHOWING THE PUMPING SYSTEM COMPONENTS AND THE TEST CELL



P' MAX. EFFECT. BLADDER PRESSURE

X FAILURE

FIGURE 4.13 LOAD PATH OF THE BLADDER AND PORE PRESSURE

5. Results

5.1 Presentation of laboratory results

The results from six laboratory experiments conducted to measure the buckling capacity of polymer pipes under radially symmetric earth and fluid pressures are presented in this Chapter. The applied bladder and pore pressures, measurements of pipe deflections and a sequence of images showing buckling of the pipe are given for each test. Detailed analysis of the contact pressures acting on the pipe and an explanation of measured buckling capacity are presented in Chapter 6.

5.2 Applied pressures and measured pipe deflections

Plots of pressure versus time presented in this section illustrate the loading sequence of the applied bladder and pore pressure up to buckling failure for each test. The loading sequence consisted of two stages. In the first stage the bladder pressure was applied up to a certain magnitude while keeping the pore pressures equal to zero. Then in the second stage both bladder and pore pressures were raised keeping the difference between both pressures constant until buckling failure occurred. The difference between the applied bladder and pore pressures is called the effective bladder pressure.

Each test was conducted with a different magnitude of effective bladder pressure and pipe thickness. All the pipes had an external diameter of 273mm. The pipes used had thickness values of 8.4 mm and 13 mm that

correspond to values of DR equal to 32.5 and 21 respectively. The DR 32.5 pipes were used in Tests T1, T2 and T3 with values of effective bladder pressures of 100, 300 and 1000 kPa, respectively. Tests T4, T5 and T6 were conducted with effective bladder pressures of 100, 300, 1000 kPa using DR 21 pipes. A summary of the tests conducted is presented in Table 5.1

The deflections of the pipe are presented in terms of the internal diameter change of the pipe. As illustrated in Figure 5.1, a positive diameter change is defined as the decrease in pipe diameter when subject to external radial pressure. The diameter change was measured using linear potentiometers that had a defined radial orientation. The radial orientation of the potentiometer denoted as LP1 was in the North-South (N-S) direction. North was arbitrarily chosen for each pipe. The potentiometer LP2 was always perpendicular to LP1 measuring the diameter change in the East-West (E-W) direction. For the test where a third potentiometer (LP3) it was used it would had been oriented Northeast-Southwest (NE-SW). The diameter change was measured at the central section of the pipe since the influence of the end conditions is the least at this location.

5.2.1 Results from test T1

Figure 5.2 is a plot of the applied bladder and pore pressure versus time during test T1. The bladder pressure was initially increased up to a magnitude of 100 kPa that was attained at approximately 600 seconds. From that point on both the bladder and pore pressures were increased simultaneously in

steps of 100 kPa and were kept constant for intervals of 5 minutes. The effective stress at the external soil boundary was equal to 100 kPa and was kept constant during the entire test. At approximately 2900 seconds, both the bladder and pore pressures reached their maximum values of 780 kPa and 680 kPa, respectively, at which time buckling of the pipe occurred.

Figure 5.3 is a plot of the measured diameter change of the pipe versus time (positive diameter change corresponds to a decrease in pipe diameter). For test T1, three linear potentiometers denoted as LP1, LP2 and LP3 were used to measure this diameter change. LP1, LP2 and LP3 were oriented N-S, E-W and NE-SW directions, respectively. The diameter change increased with pressure. The deflections measured by the three linear potentiometers were similar showing essentially radially symmetric compression of the pipe. This was as expected since the applied pressures and geometry were radially symmetric. At buckling, the maximum diameter change registered was 4.5 mm and the minimum diameter change was 3.3mm corresponding to percentage diameter change of 1.76% and 1.29% respectively.

5.2.2 Results from test T2

Figure 5.4 is a plot of applied bladder and pore pressure versus time for the experiment T2. For this experiment the bladder pressure was initially increased up to 300 kPa keeping the pore pressures equal to zero. Then both the bladder and pore pressures were increased simultaneously, keeping the

difference between both pressures to a constant value of 300 kPa at the external soil boundary. Pipe buckling occurred at approximately 5700 seconds with applied bladder and pore pressures of 1050 kPa and 750 kPa, respectively.

Figure 5.5 is a plot of the measured diameter change of the pipe versus time. Two linear potentiometers denoted as LP1 and LP2 measured the pipe deflections oriented in the N-S and E-W directions respectively. For this and all other experiments only two linear potentiometers were used instead of three as in test T1 in order to improve the quality of images obtained from the infrared camera. Deflections measured with LP1 and LP2 and plotted in Figure 5.5 were similar for the first 3000 seconds indicating a radially symmetric response of the pipe during this interval.

After 3000 seconds the deflection measurements of both linear potentiometers started to differ suggesting a possible non-symmetric response of the pipe. Possible reasons for a non-symmetric response could be non-uniformity of gravel support, variable pipe thickness or out of roundness of the pipe. Besides a non-symmetric response of the pipe, the deflection readings could have been affected by mechanical or electrical problems with the potentiometers. The calibration of the potentiometers was checked after this test showing no anomalies. The difference in deflection readings does not however affect the usefulness of the data because the conclusions obtained from this test were similar as those obtained in other tests as it is presented in Chapter 6.

At pipe buckling LP1 registered a diameter change of 5 mm and LP2 a diameter change of 7 mm, which correspond to deformations of 1.95% and 2.73% of the original pipe diameter respectively.

5.2.3 Results from test T3

Figure 5.6 shows the load sequence followed for experiment T3. Initially the bladder pressure was increased up to a magnitude of 1000 kPa with zero pore pressure. Then both the bladder and the pore pressure were raised simultaneously. A constant effective stress in the external soil boundary of 1000 kPa was kept throughout the test. Both the bladder and pore pressures reached their maximum values of 1950 kPa and 950 kPa, respectively, at approximately 9000 seconds when pipe buckling occurred.

Figure 5.7 is a plot of diameter change of the pipe versus time. Two linear potentiometers denoted as LP1 and LP2 oriented in N-S and E-W directions respectively were used to measure the pipe deflections. A symmetric response is evident because both linear potentiometers measured almost the same values of diameter change throughout the entire test with a maximum of 2% of difference in reading. Both linear potentiometers measured 11.5 mm at pipe buckling which corresponds to a deflection of 4.7% of the original pipe diameter.

Three different slopes can be distinguished from Figure 5.7. The first slope extends from the beginning of the test up to approximately 4500 seconds. This first region corresponds to loading of the soil and pipe under

bladder pressure only (zero pore pressures). The second slope extends from approximately 4500 seconds to 6300 seconds. Finally there is a third slope that extends from 6300 seconds up to pipe buckling.

The pore pressures most likely cause the different slopes noticeable in Figure 5.7. In fact, the first change in slope occurred when the pore pressure started to be applied thereby inducing additional deflections on the pipe. As a consequence, the soil may have tended to follow the pipe resulting in a decrease of the ground pressures acting on the pipe and therefore causing the second slope to be less steep than the first one. The third slope is steeper than the second one probably indicating that the pipe was loaded by magnitudes of pore pressure that were relatively high compared to the ground loads that reached the pipe during that third stage. These observations will be valuable when interpreting the results. The mechanisms leading to the three different slopes will be explained in Chapter 6.

5.2.4 Results from test T4

Figure 5.8 is a plot of applied bladder and pore pressure versus time during experiment T4. The bladder pressure was increased up to a magnitude of 100 kPa with zero pore pressure. The applied effective stress of 100 kPa at the external soil boundary was kept constant throughout the entire test. In the interval between 5500 - 6300 seconds both the bladder and the pore pressure decreased as a result of a leak in the pumping system. It is unlikely that this decrease in bladder and pore pressures had a detrimental effect on the

pressures that caused buckling since the leak was repaired within a short period of time and the effective stress at the external soil boundary was maintained constant during this period. At approximately 7000 seconds, both the bladder and pore pressures reached their maximum values of 1000 kPa and 900 kPa respectively, at which time buckling of the pipe occurred.

Figure 5.9 is a plot of diameter change versus time. Two linear potentiometers LP1 and LP2 oriented in N-S and E-W directions respectively were used to measure the pipe deflections. Both linear potentiometers measured almost the same values of diameter change from the start of the test until approximately 2500 seconds. For times greater than 2500 seconds the measurements between the two linear potentiometers started to differ. At buckling, LP1 registered a deflection of 11 mm (4.45% deflection) and LP2 registered 1 mm (0.8% deflection). Both linear potentiometers presented disproportionate values of deflection that made this test useless for the further data analysis presented in Chapter 6. This is the only test that presented disproportionate values of pipe deflection and do not represent an important source of uncertainty for the entire test program.

5.2.5 Results from test T5

Figure 5.10 is a plot of applied bladder and pore pressure versus time during experiment T5. The bladder pressure was increased up to a magnitude of 300 kPa attained at approximately 2300 seconds with zero pore pressures. At approximately 7000 seconds both the bladder and pore pressures reached

their maximum values of 1500 kPa and 1200 kPa respectively at which time buckling of the pipe occurred.

Figure 5.11 is a plot of diameter change of the pipe versus time. Two linear potentiometers LP1 and LP2 oriented in N-S and E-W respectively measured the pipe deflections. At the early stages of the test the difference of the two measurements was approximately 1 mm but as the test progressed the difference in reading was narrowed. At pipe buckling, LP1 registered a deflection of 7.5 mm and LP2 registered a deflection of 5 mm that correspond respectively to percentage deflections of 3% and 2% of the original pipe diameter.

5.2.6 Results from test T6

Figure 5.12 is a plot of applied bladder and pore pressure versus time for experiment T6. The bladder pressure was increased up to a magnitude of 1000 kPa that was attained at approximately 5000 seconds with zero pore pressures. At this point both the bladder and pore pressures were increased simultaneously in steps of 100 kPa and were kept constant for intervals of 5 minutes. The applied effective stress of 1000 kPa at the external soil boundary was kept constant throughout the entire test. At approximately 12000 seconds both the bladder and pore pressures reached their maximum values of 2400 kPa and 1400 kPa respectively at which time buckling of the pipe occurred.

Figure 5.13 is a plot of measured diameter change versus time measured by two linear potentiometers LP1 and LP2 oriented N-S and E-W respectively. The measurements between LP1 and LP2 are almost the same (with a maximum 2.3 % difference) showing that the pipe deflections were essentially radially symmetric.

Three slopes can also be distinguished in Figure 5.13. The first slope extends from the beginning of the test up to approximately 5100 seconds. This first region corresponds to loading of the soil and pipe under bladder pressure only. The second slope extends approximately from 5100 to 7500 seconds. The third slope extends from 7500 seconds to the end of the experiment.

The slopes of the plot indicate the possible influence of the pore pressures on the ground loads that reached the pipe. As it turned out for test T3, the first change in slope occurred when the pore pressures were increased. The pore pressures induced additional deformations of the pipe probably causing the soil to follow the radial deformation of the pipe resulting in a decrease of the ground loads that reached the pipe. The decrease in ground loads could be reflected in a less steep slope. Finally the third slope was steeper than the second one probably indicating that the magnitude pore pressures was high compared to the ground loads that acted on the pipe during that stage of the test. These observations, gathered in test T3 and T6, are important in the analysis of the buckling mechanism presented in Chapter 6.

Finally at pipe buckling, LP 1 registered a diameter change of 14.4 mm (5.2% deflection of original pipe diameter) and LP2 registered 13.3 mm (4.8% deflection of original pipe diameter).

5.3 Summary of results

Table 5.1 summarizes the bladder pressure P and the pore pressure u that caused buckling for every test. Figure 5.14 is a plot of pore pressure at failure versus the effective bladder pressure P' for each test. Each line corresponds to a group of pipes with the same DR. A higher buckling capacity was recorded for thicker pipes.

For the six experiments the buckling resistance of the pipes increased as the effective bladder pressure increased. This seems reasonable since the buckling resistance is dependent on the stiffness of the soil that surrounds the pipe and the soil stiffness is increased as the magnitude of effective stress acting in the soil increased.

The measured deflections showed that the percentage deflections at buckling were lower than the limits recommended by the ASTM F714-97. The percentage deformation at buckling failure ranged from 1.3% to 5.8%, which contrasts with the recommended range of percentage deformations of 3.3% to 11% for plain HDPE pipes given in the ASTM F714-97. Therefore proper care must be exercised for pipes designed under ground and fluid loads.

The three different slopes in the deformation plots of test T3 and T6 (Figure 5.7 and Figure 5.13 respectively) suggested that the pore pressures

affected the ground loads that reached the pipe. The additional deformations on the pipe induced by the pore pressures and the decrease of ground loads that results when the soil follows the pipe are consistent arguments to explain the difference in slopes. This possible explanation for these different slopes will be confirmed in Chapter 6.

5.4 Visual observations from the infrared camera

The images captured with the infrared camera located inside the pipe provided useful observations to understand the buckling mechanism under soil and fluid loading. Table 5.2 summarizes the following observations about the dimple (the dimple refers to the bulging that occurs inside the pipe at the time of buckling):

- Orientation of the radial axis of the dimple with respect to the upward vertical direction of the image,
- Axial location of the dimple in the pipe,
- Circumferential angle of the dimple,
- Influence of the dimple on the deformation measurements,
- Description of the dimple curvature (gradual or abrupt), and
- Number of dimples.

5.4.1 Sequence of buckling images for test T1

Figure 5.15 is the image of the inside of the pipe prior to the onset of buckling captured with the infrared camera. Reference points (appearing as white dots

in the image) were placed on the pipe wall in order to define the inside surface of the pipe. A reference line was also drawn at mid-height of the pipe to track the response of the centre section. These references marks were used for all tests except for test T4 because it was the first test performed and it revealed the need for references marks to identify the buckled shape.

Figures 5.16 to 5.20 shows the sequence of the buckling failure. The time for the dimple to initiate and develop was only approximately 5 seconds for test T1. Only one dimple was formed and because it occurred on some of the reference points the buckling sequence can be clearly seen from the images. This dimple had a gradual curvature with a circumferential angle of approximately 50 degrees and an orientation of 330 degrees clockwise from the upward vertical direction of the images. The deformations measurements were influenced as a result of the proximity with the dimple.

5.4.2 Sequence of buckling images for test T2

Figure 5.21 shows the image of the inside of the pipe prior to buckling. In Figures 5.22 to 5.26 the sequence of buckling failure is shown for test T2. Only one dimple was formed and it occurred above the mid-height of the pipe with an orientation of approximately 170 degrees clockwise from the upward vertical direction of the image. Because the dimple occurred so close to the camera it is not as easily discernible as for test T1 and although it appears to be smaller than that of test T1 in the images, it had the same approximate size. The dimple occurred away from the deformation measurements, it took

5 seconds to form and it could be described as having a gradual curvature like dimple of test T1. The circumferential angle of the dimple was difficult to determine given the close proximity of the dimple to the camera.

5.4.3 Sequence of buckling images for test T3

Figure 5.27 shows the image of the inside of the pipe prior to buckling. In Figures 5.28 to 5.32 the sequence of buckling failure is shown for test T3. Only one dimple was formed and it occurred above the mid-height of the pipe with an orientation of 20 degrees clockwise from the upward vertical direction of the image. The dimple could be easily seen in the sequence of images, it had a circumferential angle of approximately 45 degrees and occurred away from the deformation measurements. The dimple took 7 seconds to form and it had an abrupt curvature compared with the dimple curvatures from test T1 and T2. This observation suggests that the higher the effective bladder pressure P' the more abrupt the curvature of the dimple. This is consistent because a more abrupt curvature is related to a stiffer soil which is proportional to the magnitude of P' .

5.4.4 Sequence of buckling images for test T4

Figure 5.33 shows the image of the inside of the pipe prior to buckling. In Figures 5.34 to 5.36 the sequence of the buckling failure is shown for test T4. Because this was the very first test performed it had not reference points and the difficulty in detecting the wrinkle revealed the need for reference marks for

the subsequent tests. Nevertheless, the dimple can be seen in the images and had a circumferential angle of approximately 40 degrees with an orientation of 190 degrees clockwise from the upward vertical direction of the image. The proximity of the potentiometer LP1 to the dimple influenced the deformation reading showing a clear increase in inward diametric deformation during buckling. The dimple took 4 seconds to form and had a gradual curvature similar to the dimple curvatures in tests T1 and T2.

5.4.5 Sequence of buckling images for test T5

Figure 5.37 shows the image of the inside of the pipe prior to buckling. In Figures 5.38 to 5.41 the sequence of buckling failure is shown for test T5. Only one dimple was formed with a circumferential angle of approximately 30 degrees and an orientation of approximately 250 degrees clockwise from the upward vertical direction of the image. The dimple took 4 seconds to form and occurred in the lower section of the pipe. The lack of reference points in that location made the dimple not easily discernible in the sequence of images. Nevertheless, the dimple curvature was gradual as the dimple curvatures in tests T1, T2 and T4.

5.4.6 Sequence of buckling images for test T6

Figure 5.42 shows the image of the inside of the pipe prior to buckling. In Figures 5.43 to 5.46 the sequence of the buckling failure is shown for test T6. In about 5 seconds only one dimple was formed, and it had a circumferential

angle of approximately 30 degrees, and an orientation of approximately 45 degrees clockwise from the upward vertical direction of the image. Because it occurred in the lower section of the pipe it is difficult to see the dimple in the photo sequence due to the lack of reference points in that location. The dimple had an abrupt curvature compared with the dimples in tests T4 and T5. This observation is similar to the one made for tests T1, T2 and T3 in which a more abrupt curvature is observed as the effective bladder pressure P' was higher.

5.5 Summary of the visual observations

Figure 5.47 is a compilation of the final buckling images from the six tests. Figure 5.48 is a set of sketches of the images at buckling for the six tests in order to make the images comparable from each test. The orientation of the dimple and its axial location was different in every test. No correlation was found between the variables of the test (effective bladder pressure P' , pipe DR and fluid pressure at buckling) and the location of the dimples for the six tests conducted. For both tests T5 and T6 the dimple occurred at approximately 200 mm from the bottom seal possibly showing that the influence of the bottom end condition on the buckling resistance was minimal for this section of the pipe.

It was also observed that the higher the effective bladder pressure P' used for a test, the more abrupt the curvatures of the dimples. This observation is consistent with the fact that the higher the magnitude of P' the

stiffer the soil is going to be and a more abrupt curvature is expected as the stiffness of the soil increases.

The sequence of buckling revealed a single-wave type of failure in every test. A single-wave type of failure means the formation of only dimple throughout the entire circumference of the pipe. This observation implies that at the time of buckling the loads acting on the pipe were mostly fluid loads.

The observations obtained from the infrared camera and the measured deflections of the pipe data are the starting point of a more detailed analysis in Chapter 6 to clarify and explain the mechanism leading to buckling.

Test	Pipe DR	Effective Bladder Pressure P' (kPa)	Bladder Pressure P at failure (kPa)	Pore Pressure u at failure (kPa)
T1	32.5	100	780	680
T2	32.5	300	1050	750
T3	32.5	1000	1950	950
T4	21	100	1000	900
T5	21	300	1500	1200
T6	21	1000	2400	1400

TABLE 5.1 SUMMARY OF THE EXPERIMENTAL RESULTS SHOWING THE TEST NOTATION, PIPE DR, EFFECTIVE BLADDER PRESSURE, BLADDER PRESSURE AT FAILURE AND THE PORE PRESSURE AT FAILURE

Test	Clockwise orientation of radial axis of dimple with respect to the vertical	Axial location of the dimple	Circumferential angle of the dimple	Was the dimple close to linear potentiometers ?	Influence on deflection measurements ?	Description of the curvature of the dimple	Number of dimples
T1	330 degrees	Above mid-height	50 degrees	Yes	Yes (LP1 and LP3 registered outward deformation and LP2 registered inward deformation)	Gradual curvature	1
T2	170 degrees	Above mid-height	Difficult to determine	No	None	Gradual curvature	1
T3	20 degrees	Above mid-height	45 degrees	No	None	Abrupt curvature	1
T4	190 degrees	Above mid-height but very close to linear potentiometers	40 degrees	Yes	Yes (LP1 registered outward deformation and LP2 registered inward deformation)	Gradual curvature	1
T5	250 degrees	Below	30 degrees	No	None	Gradual curvature	1
T6	45 degrees	Below	30 degrees	No	None	Abrupt curvature	1

TABLE 5.2 SUMMARY OF THE VISUAL OBSERVATIONS OF BUCKLING FAILURE PRESENTING FOR EACH TEST THE ORIENTATION OF THE DIMPLE, THE LOCATION WITH RESPECT TO THE MID-HEIGHT OF THE PIPE, THE CIRCUMFERENTIAL ANGLE OF THE DIMPLE, THE INFLUENCE OF THE DIMPLE ON THE MEASUREMENTS, THE DESCRIPTION OF THE DIMPLE AND THE NUMBER OF DIMPLES

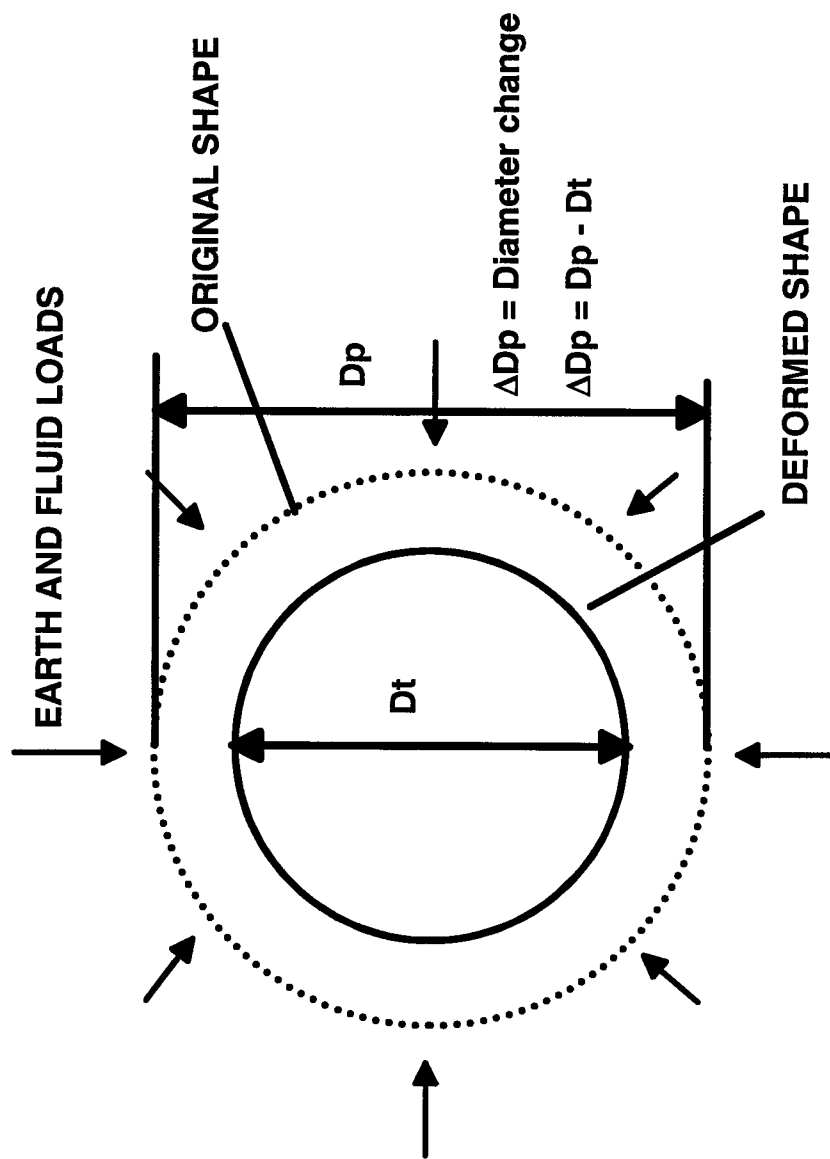


FIGURE 5.1 DIAMETER CHANGE OF A PIPE UNDER EARTH AND FLUID PRESSURES

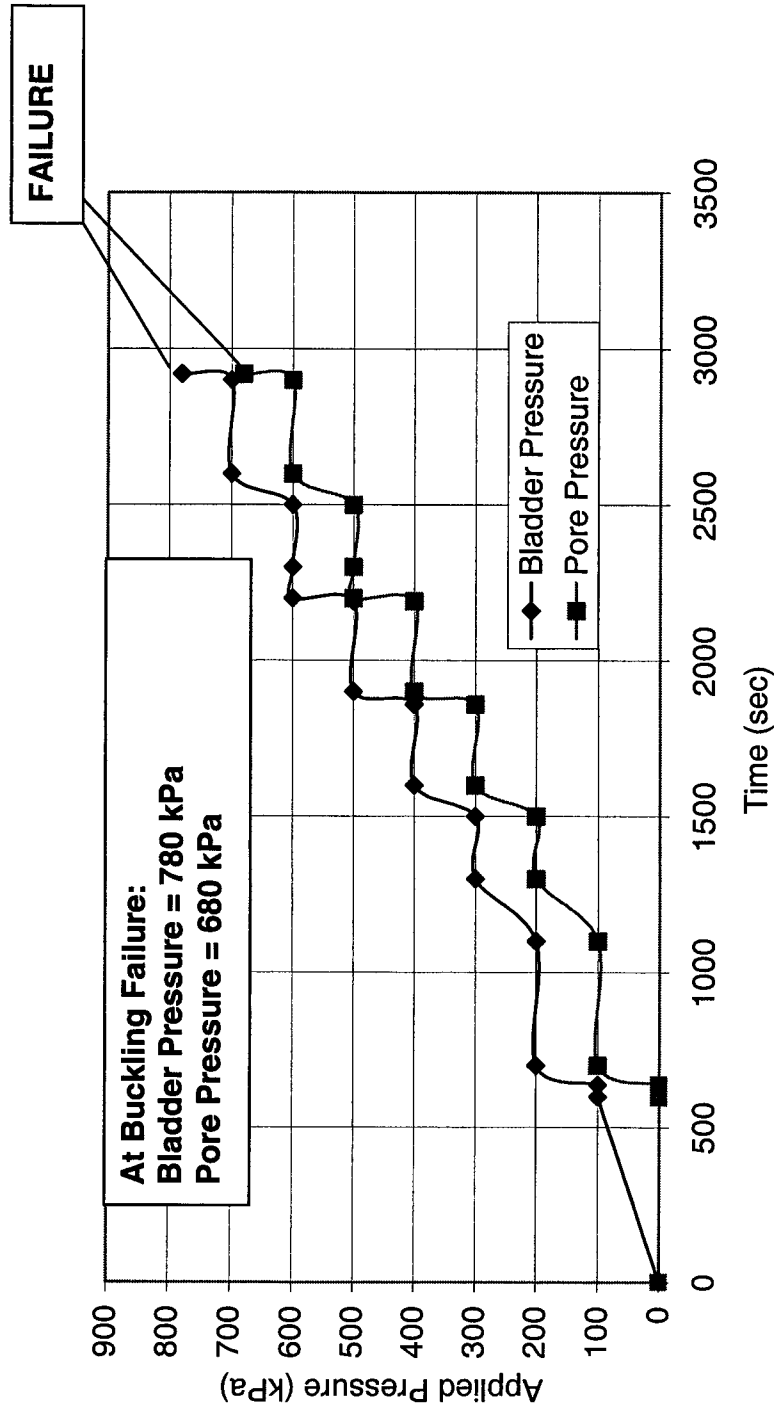


FIGURE 5.2 APPLIED BLADDER AND PORE PRESSURE VS. TIME FOR TEST T1 (DR 32.5 AND P'=100 kPa)

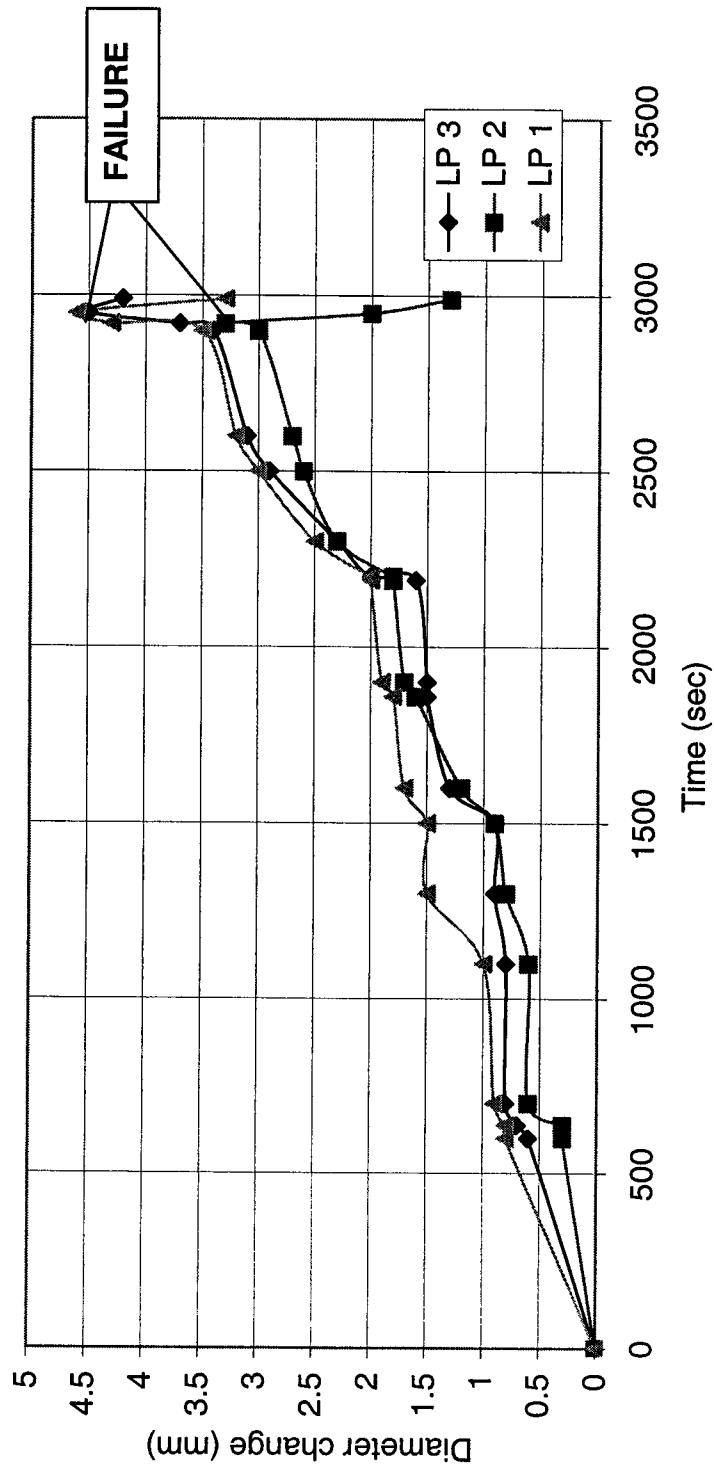


FIGURE 5.3 DIAMETER CHANGE VS. TIME FOR TEST T1 (DR 32.5 AND P'=100 kPa)

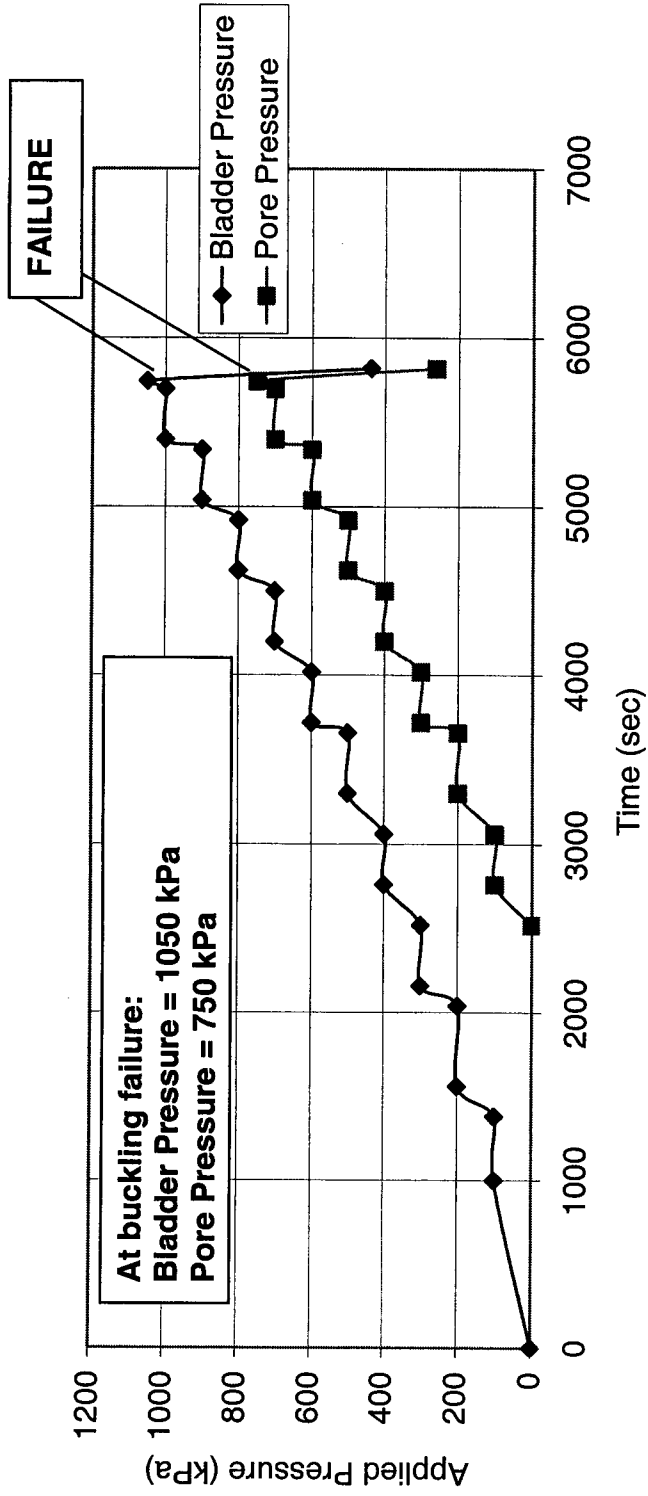


FIGURE 5.4 APPLIED BLADDER AND PORE PRESSURE VS. TIME FOR TEST T2 (DR 32.5 AND P'=300 kPa)

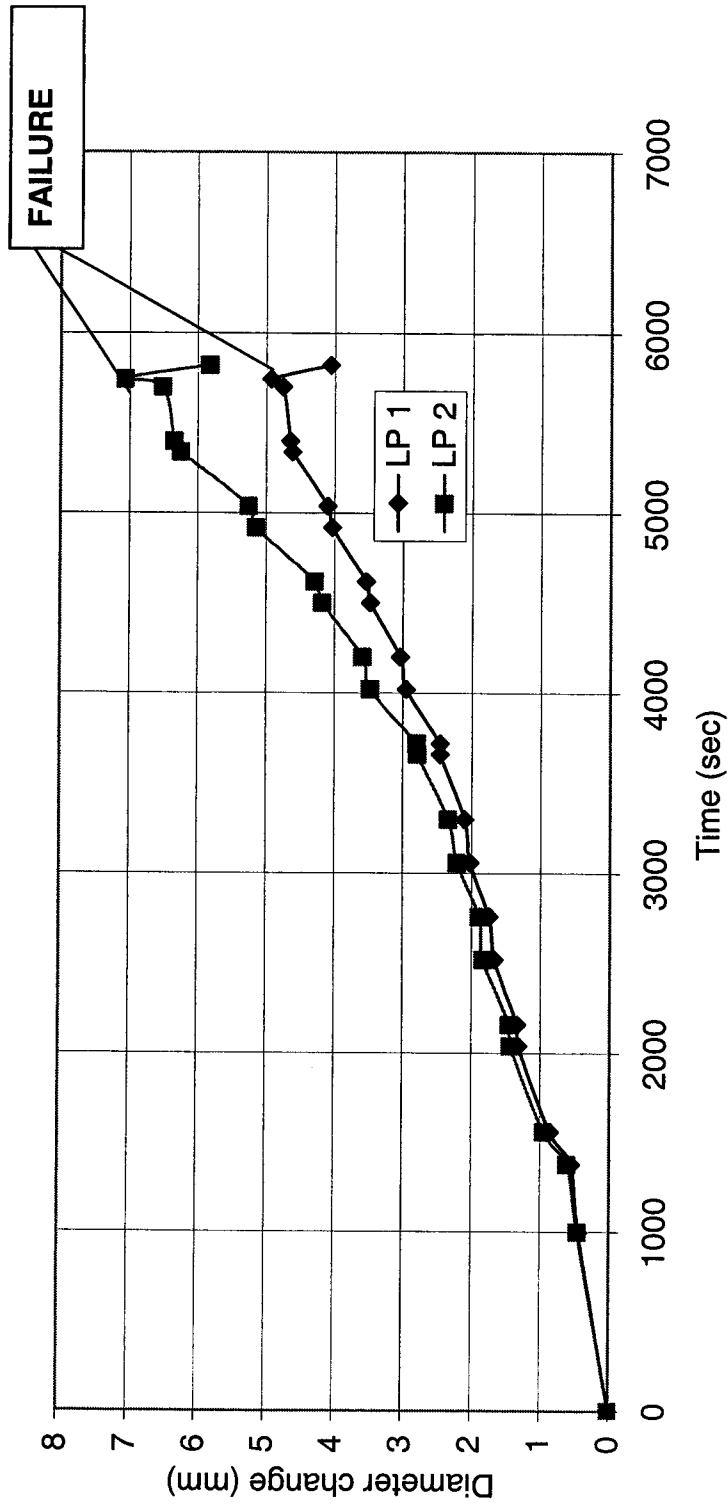


FIGURE 5.5 DIAMETER CHANGE VS. TIME FOR TEST T2 (DR 32.5 AND P'=300 kPa)

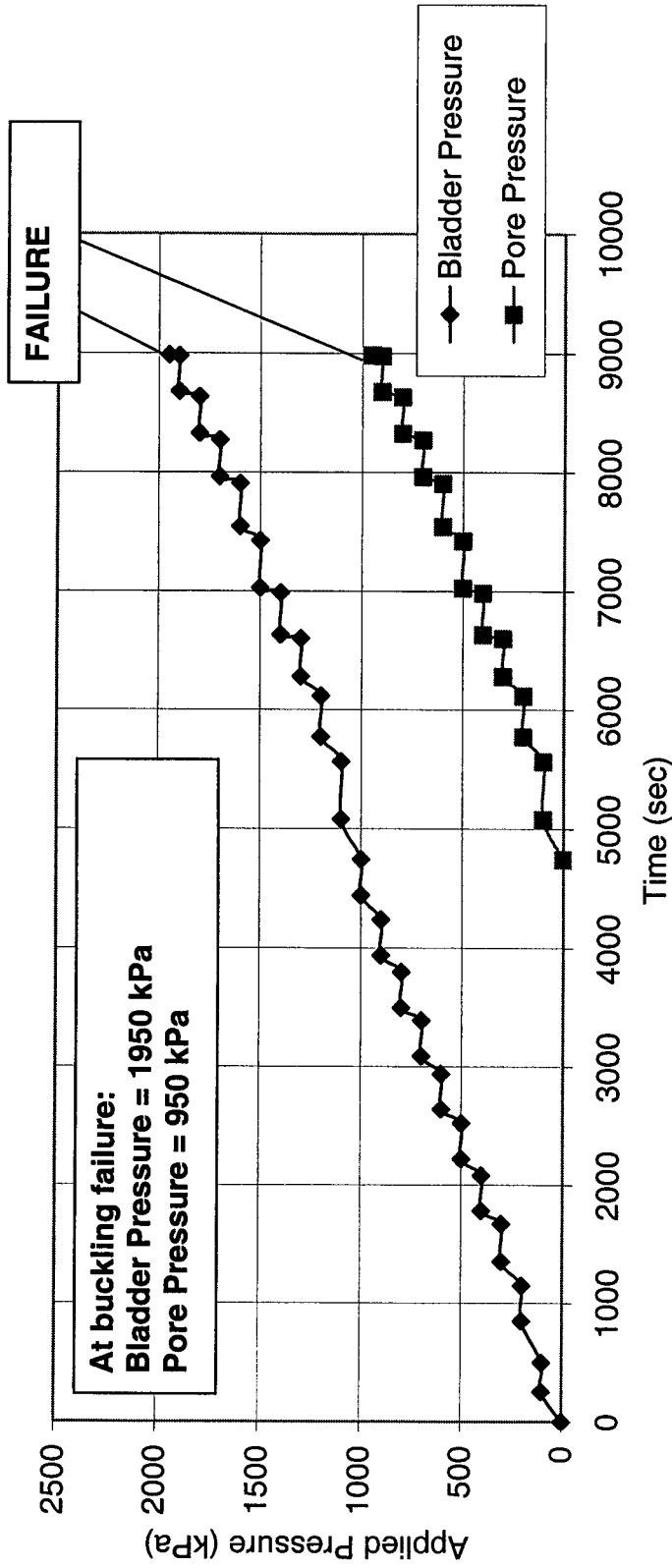


FIGURE 5.6 APPLIED BLADDER AND PORE PRESSURE VS. TIME FOR TEST T3 (32.5 AND P' = 1000 kPa)

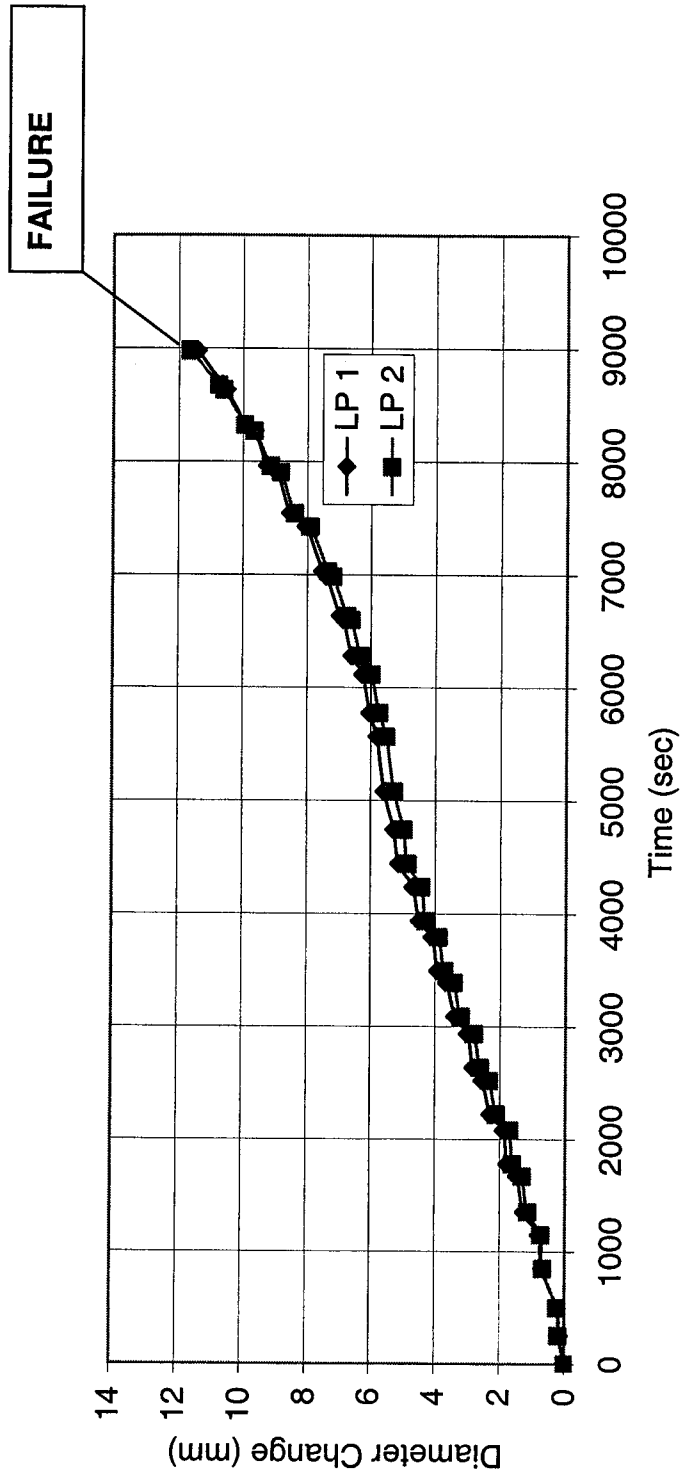


FIGURE 5.7 DIAMETER CHANGE VS. TIME FOR TEST T3 (DR 32.5 AND P'=1000 kPa)

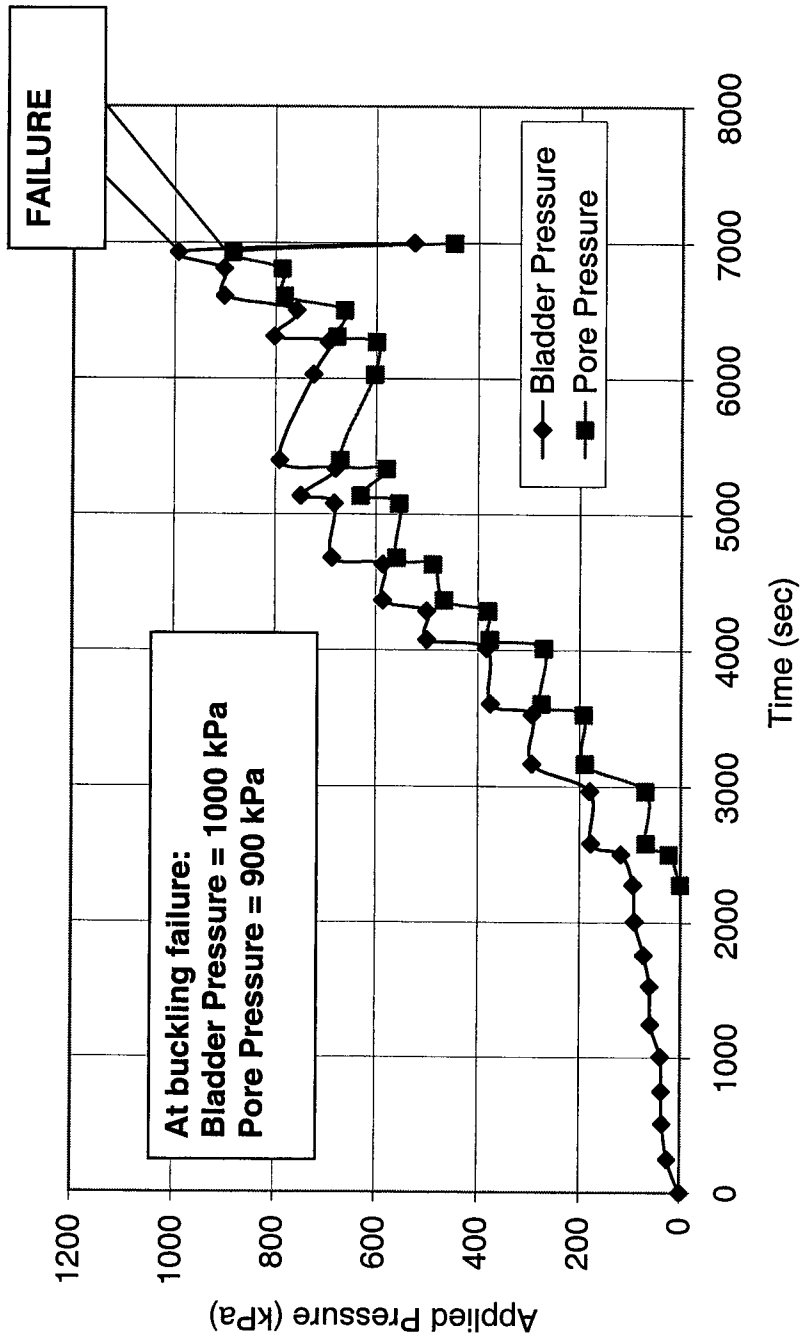


FIGURE 5.8 APPLIED BLADDER AND PORE PRESSURE VS. TIME FOR TEST T4 (DR 21 AND P'=100 kPa)

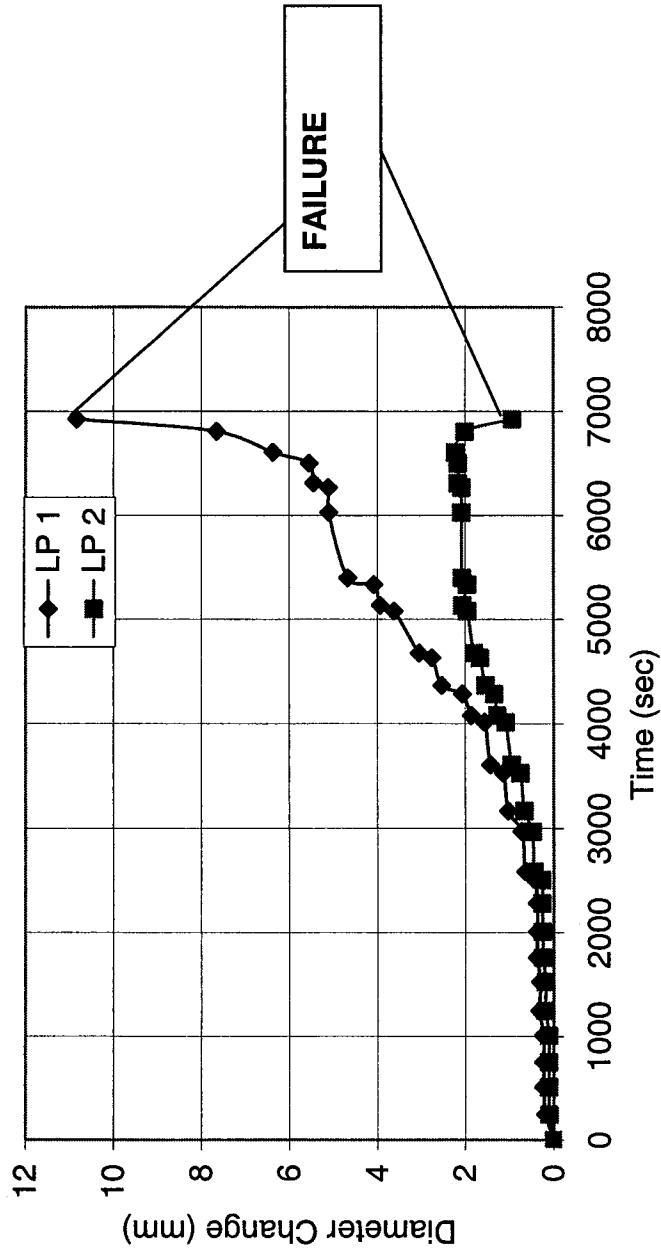


FIGURE 5.9 DIAMETER CHANGE VS. TIME FOR TEST T4 (DR 21 AND FOR $P' = 100$ kPa)

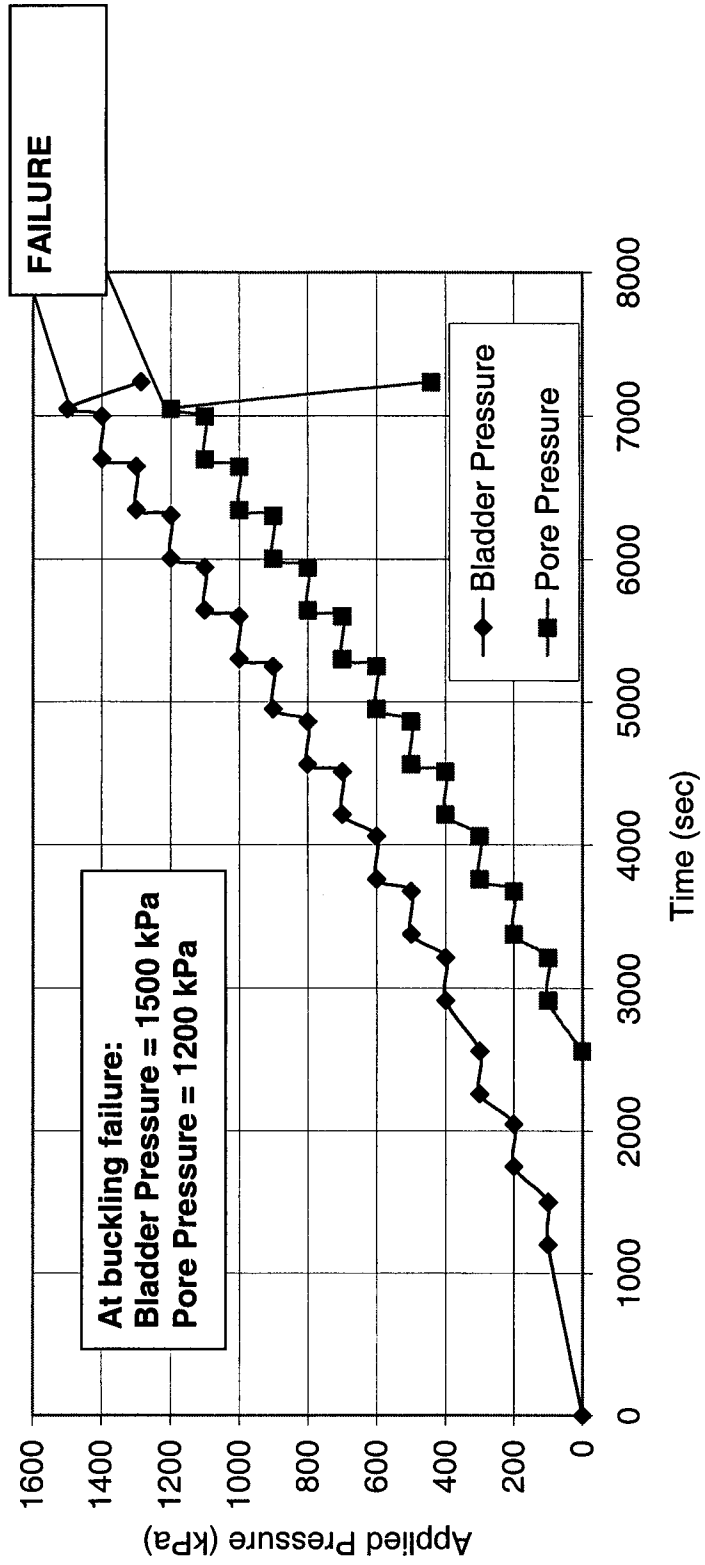


FIGURE 5.10 APPLIED BLADDER AND PORE PRESSURE VS. TIME FOR TEST T5 (DR 21 AND P'=300 kPa)

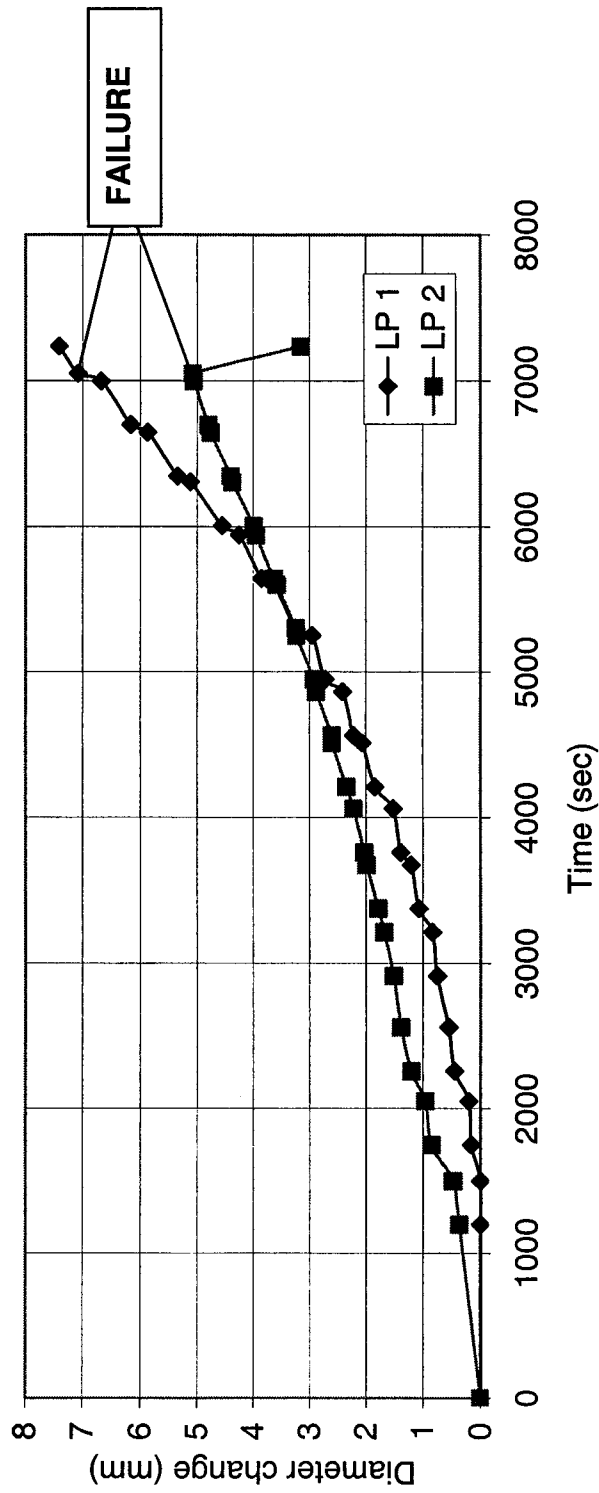


FIGURE 5.11 DIAMETER CHANGE VS. TIME FOR TEST T5 (DR 21 AND P'=300 kPa)

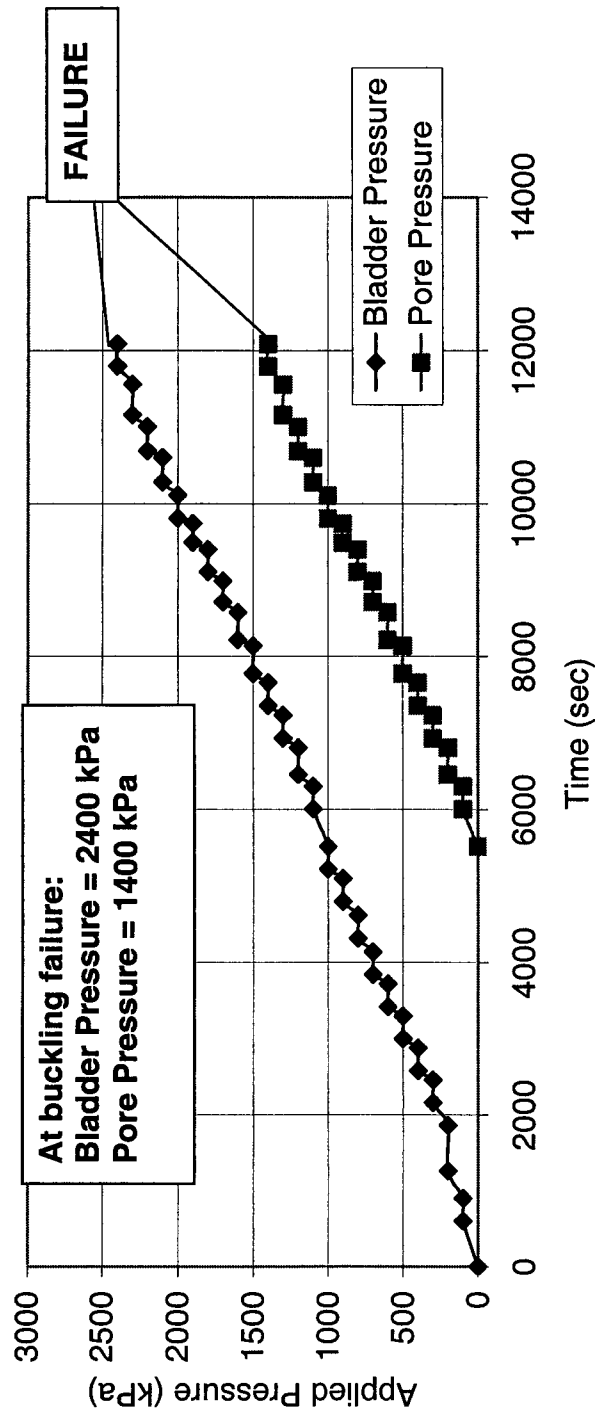


FIGURE 5.12 APPLIED BLADDER AND PORE PRESSURE VS. TIME FOR TEST T6 (DR 21 AND P' = 1000 kPa)

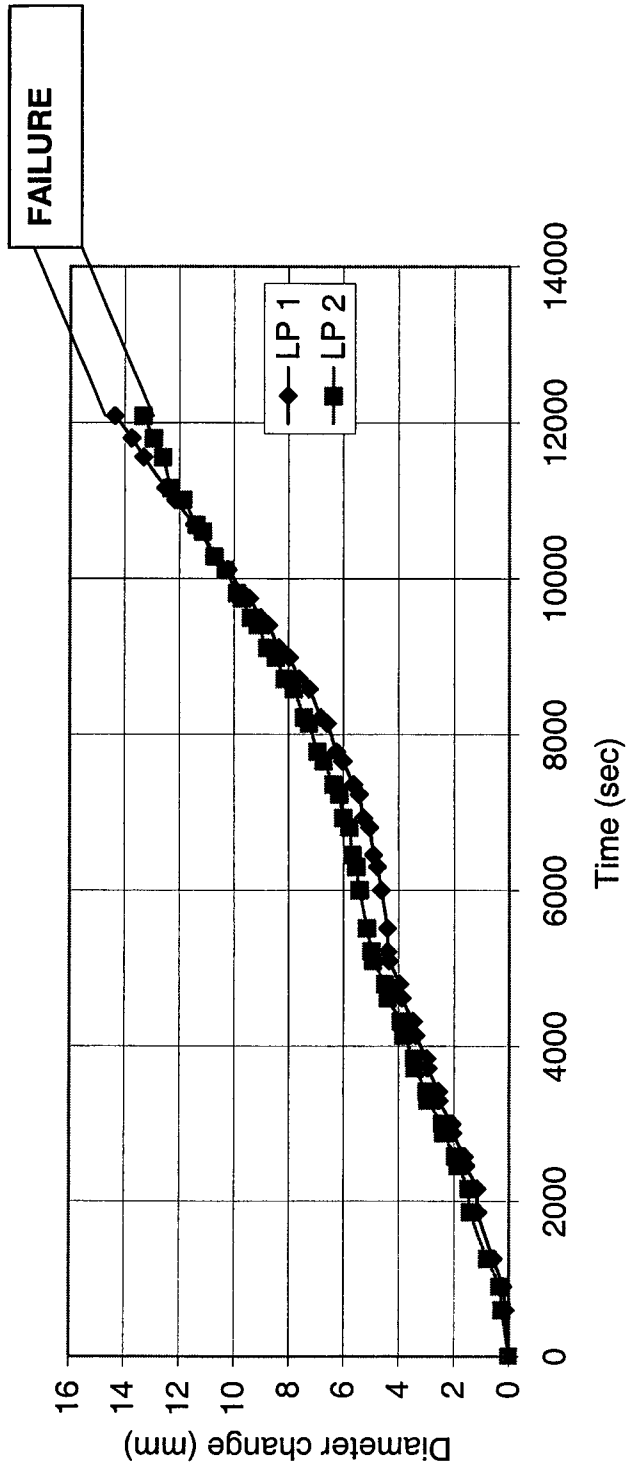
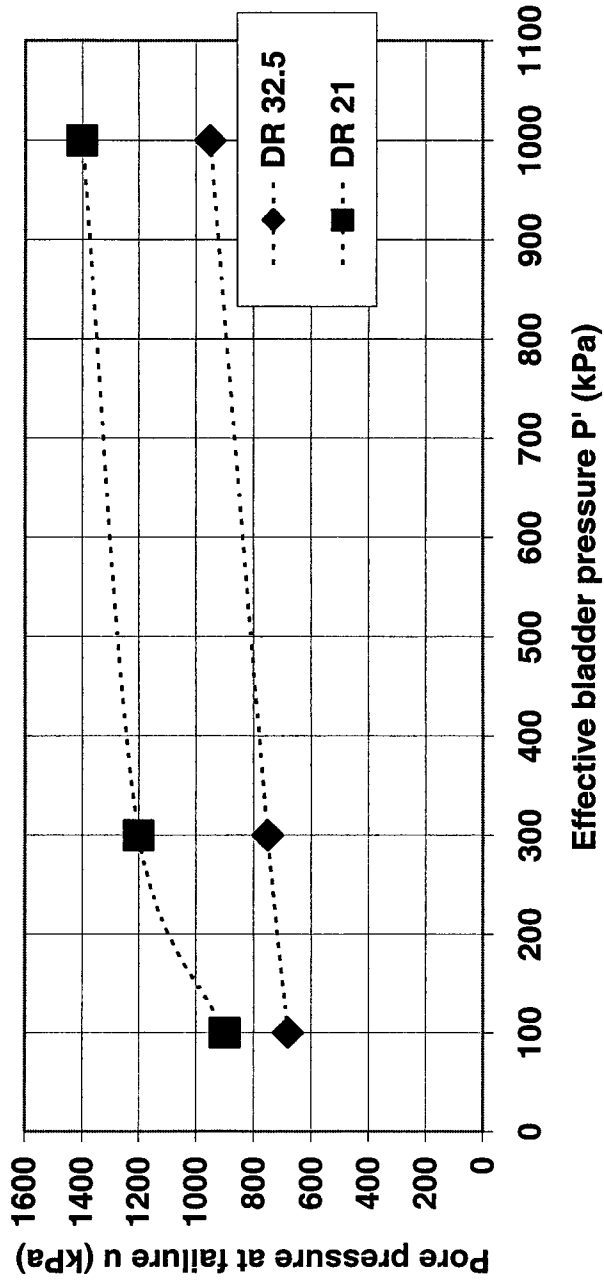


FIGURE 5.13 DIAMETER CHANGE VS. TIME FOR TEST T6 (DR 21 AND P'=1000 kPa)



**FIGURE 5.14 PORE PRESSURE AT FAILURE VS. EFFECTIVE STRESS SUSTAINED DURING EACH TEST
(FOR THE COMPLETE TEST PROGRAM)**

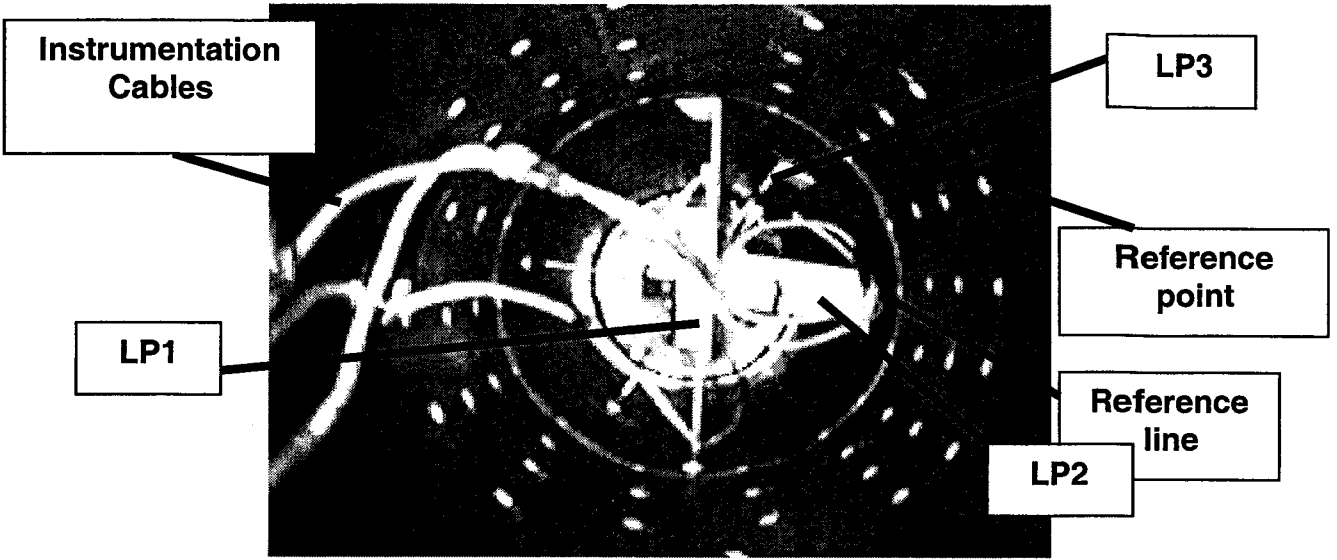


FIGURE 5.15 INFRARED CAMERA IMAGE FROM THE INSIDE OF THE PIPE PRIOR TO ONSET OF BUCKLING DURING TEST T1

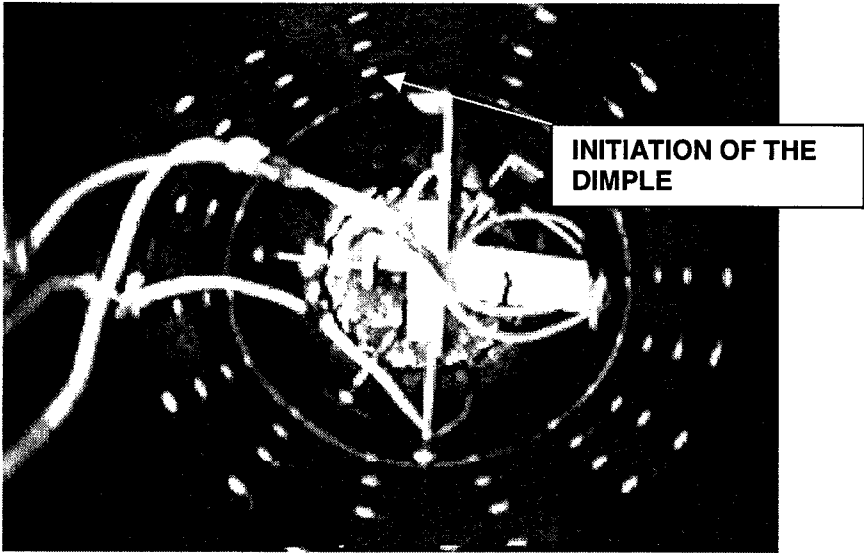


FIGURE 5.16 INITIATION OF THE DIMPLE AT t=2953 SECONDS DURING TEST T1

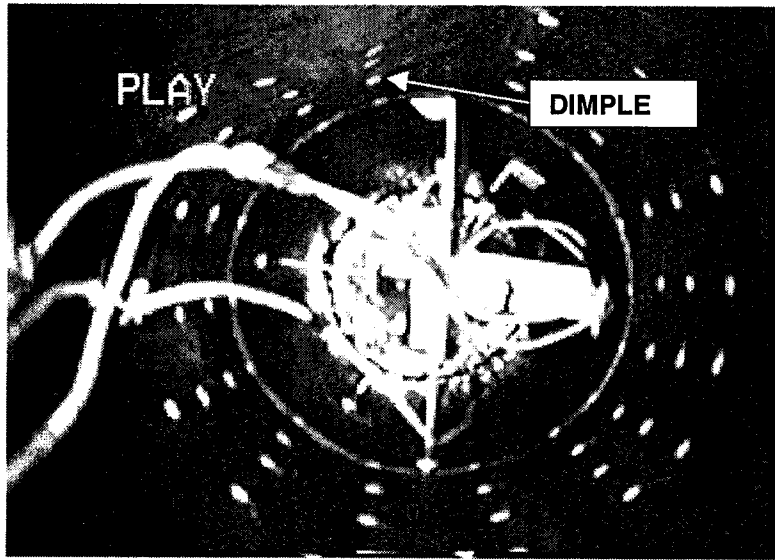


FIGURE 5.17 PROPAGATION OF THE DIMPLE AT $t=2954$ SECONDS DURING TEST T1

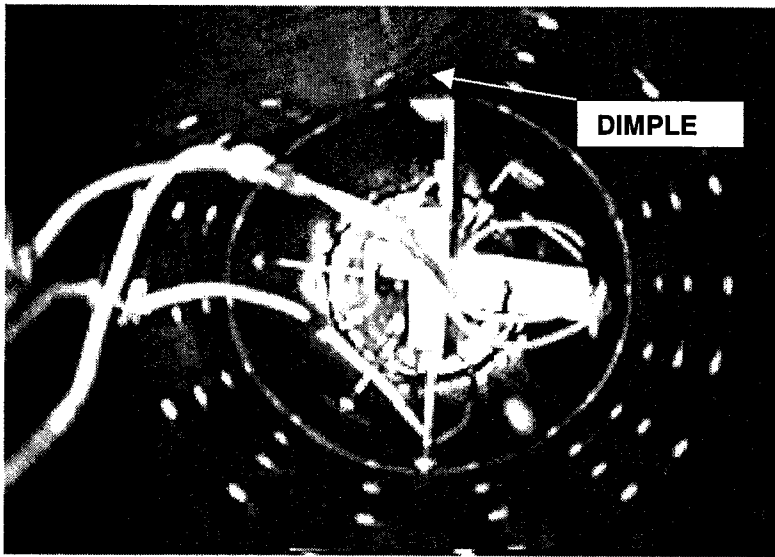


FIGURE 5.18 PROPAGATION OF THE DIMPLE AT $t=2955$ SECONDS DURING TEST T1

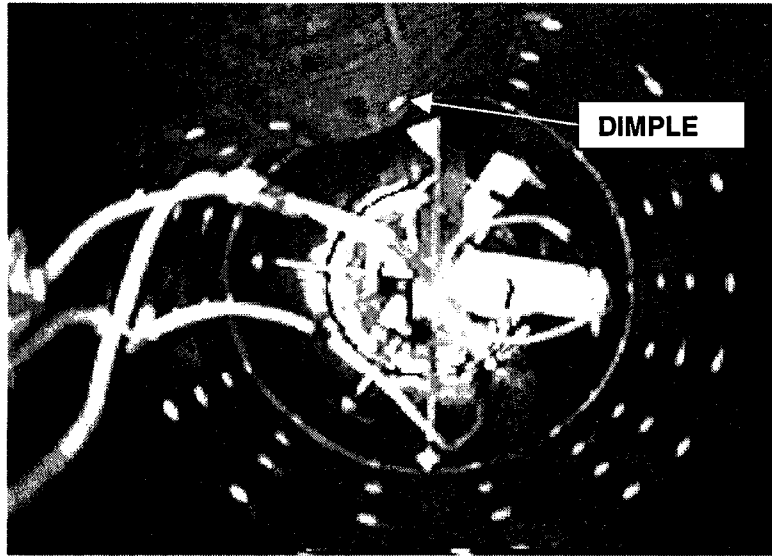


FIGURE 5.19 PROPAGATION OF THE DIMPLE AT $t=2957$ SECONDS DURING TEST T1

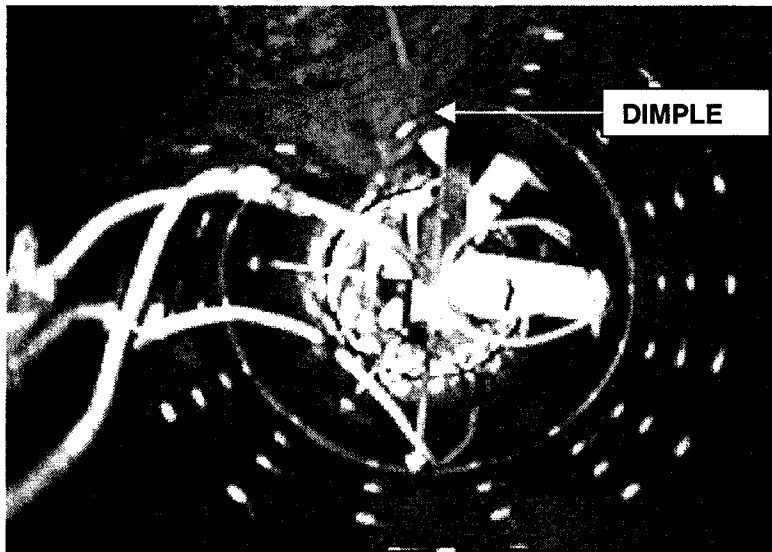


FIGURE 5.20 FINAL DEFORMED PROFILE OF PIPE SHOWING FULL DEVELOPMENT OF THE DIMPLE AT $t=2958$ SECONDS FOR TEST T1

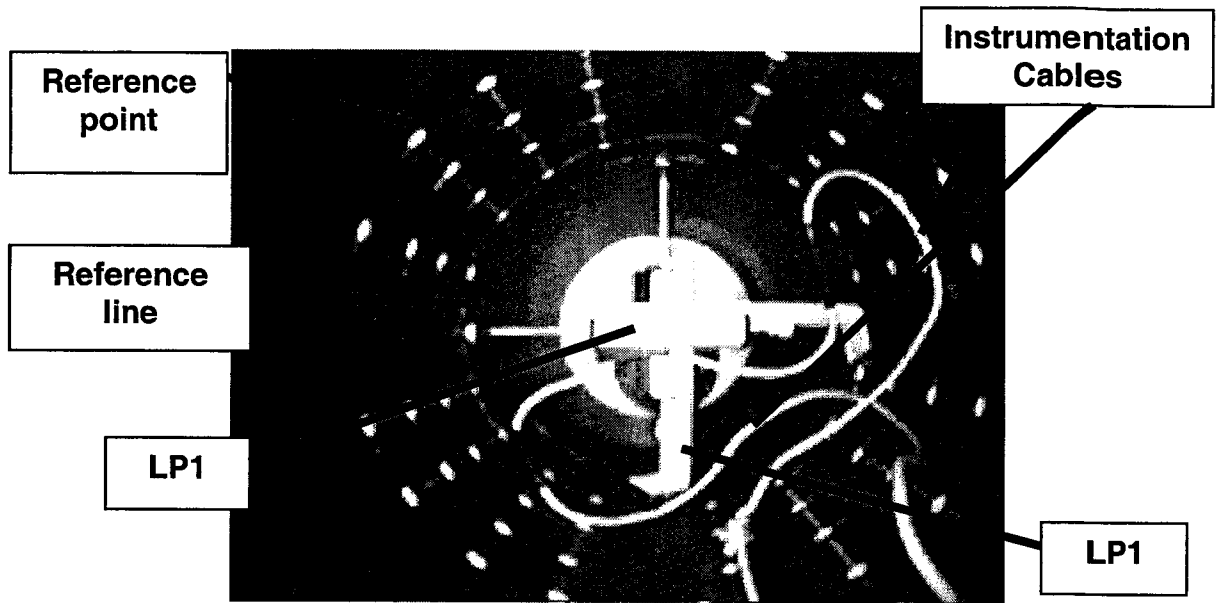


FIGURE 5.21 INFRARED CAMERA IMAGE FROM THE INSIDE OF THE PIPE PRIOR TO ONSET OF BUCKLING DURING TEST T2

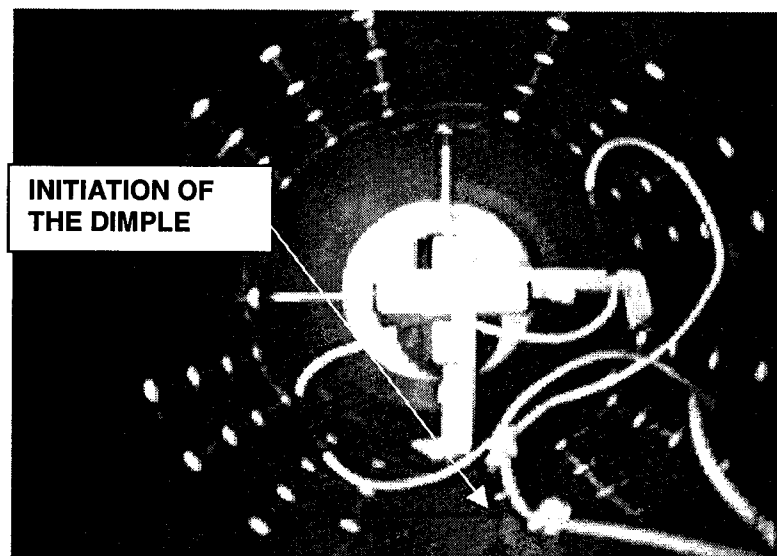


FIGURE 5.22 INITIATION OF DIMPLE AT $t=5717$ SECONDS DURING TEST T2

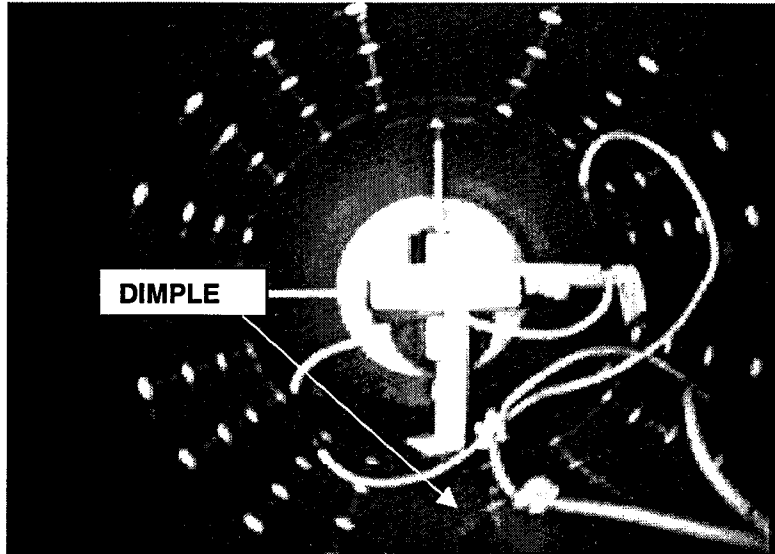


FIGURE 5.23 PROPAGATION OF THE DIMPLE AT $t=5718$ SECONDS DURING TEST T2

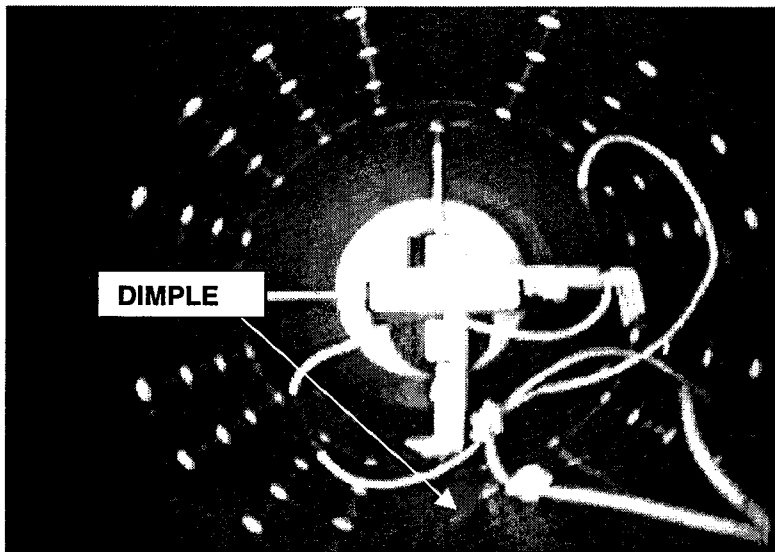


FIGURE 5.24 PROPAGATION OF THE DIMPLE AT $t=5719$ SECONDS DURING TEST T2

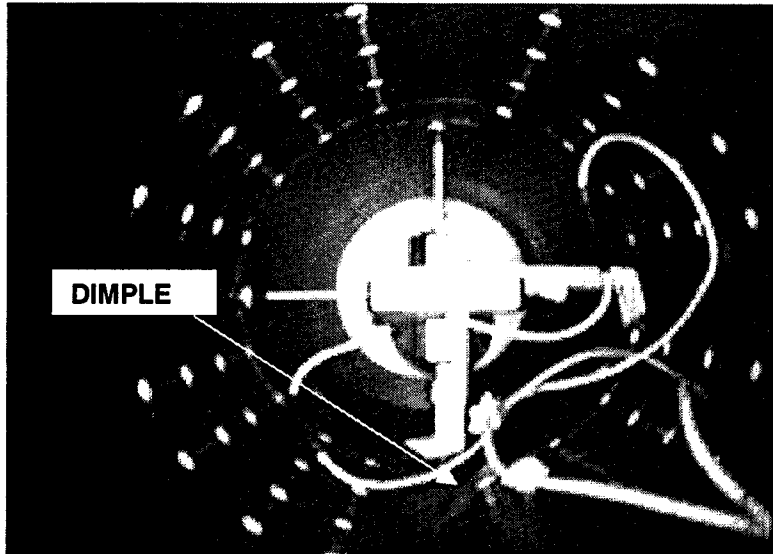


FIGURE 5.25 PROPAGATION OF THE DIMPLE AT $t=5720$ SECONDS DURING TEST T2

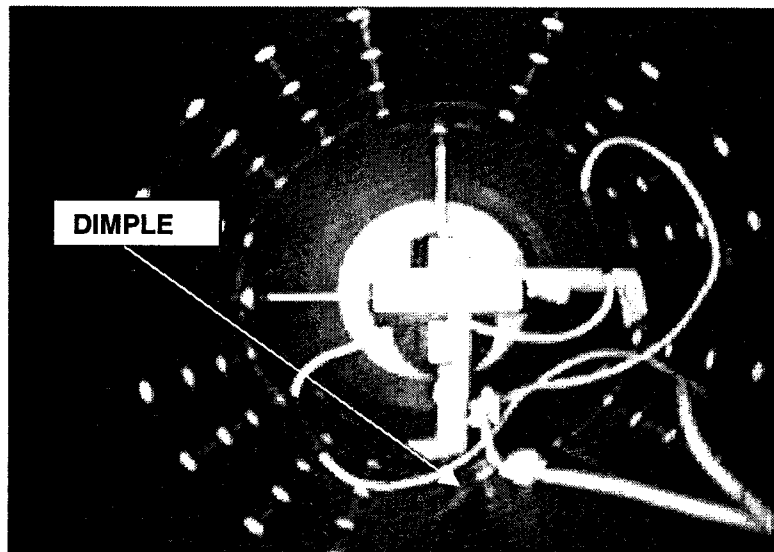


FIGURE 5.26 FINAL DEFORMED PROFILE OF PIPE SHOWING FULL DEVELOPMENT OF THE DIMPLE AT $t=5722$ SECONDS FOR TEST T2

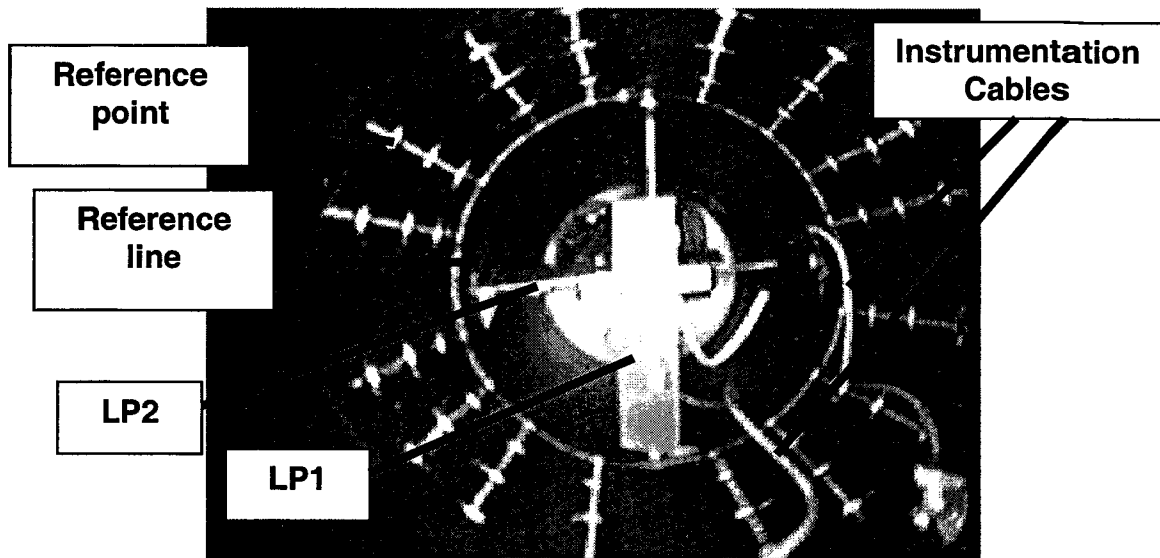


FIGURE 5.27 INFRARED CAMERA IMAGE FROM THE INSIDE OF THE PIPE PRIOR TO ONSET OF BUCKLING DURING TEST T3

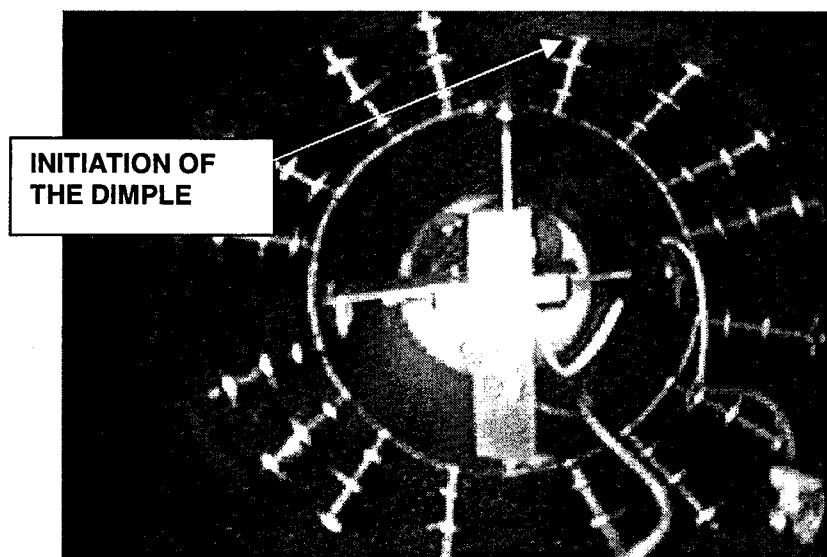


FIGURE 5.28 INITIATION OF THE DIMPLE AT $t=8996$ SECONDS DURING TEST T3

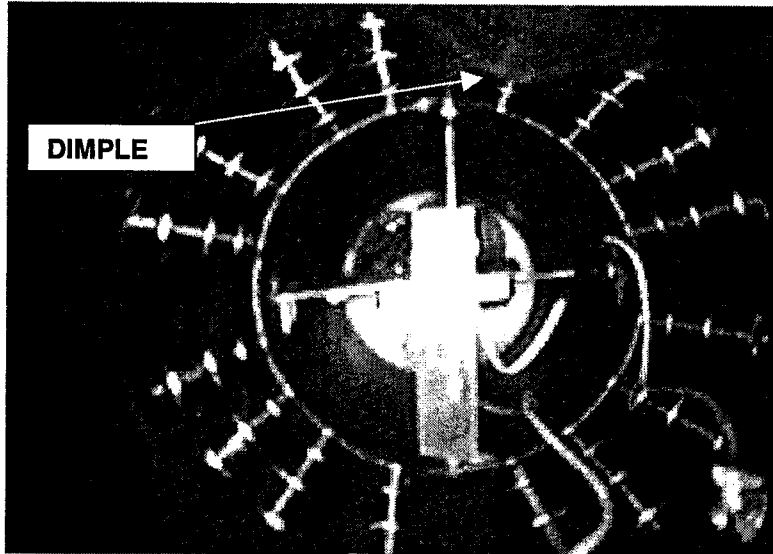


FIGURE 5.29 PROPAGATION OF THE DIMPLE AT $t = 8998$ SECONDS DURING TEST T3

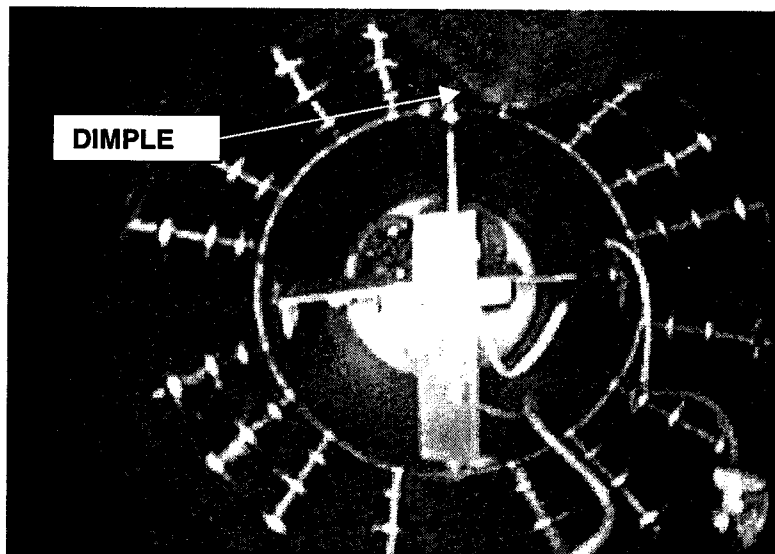


FIGURE 5.30 PROPAGATION OF THE DIMPLE AT $t = 9000$ SECONDS DURING TEST T3

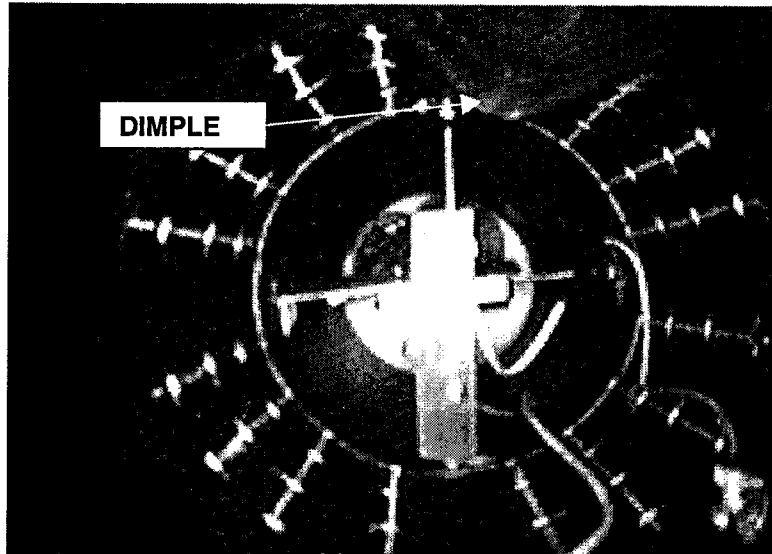


FIGURE 5.31 PROPAGATION OF THE DIMPLE AT $t = 9001$ SECONDS DURING TEST T3

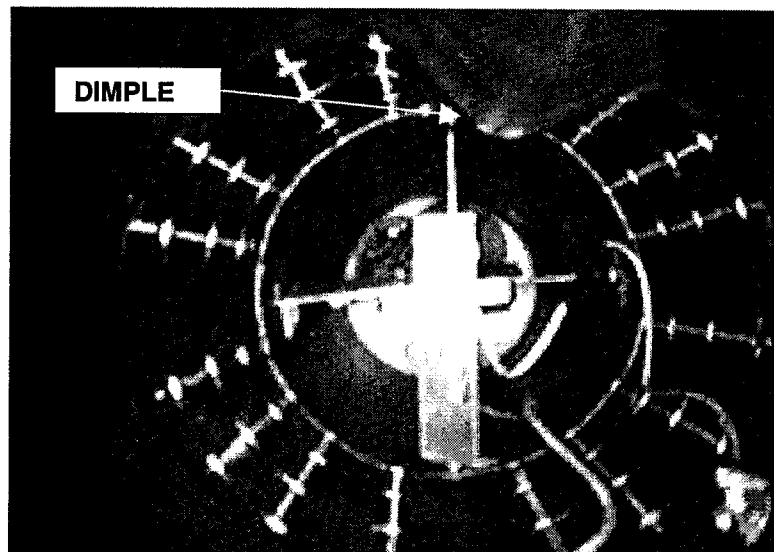


FIGURE 5.32 FINAL DEFORMED PROFILE OF PIPE SHOWING FULL DEVELOPMENT OF THE DIMPLE AT $t=9003$ SECONDS FOR TEST T3

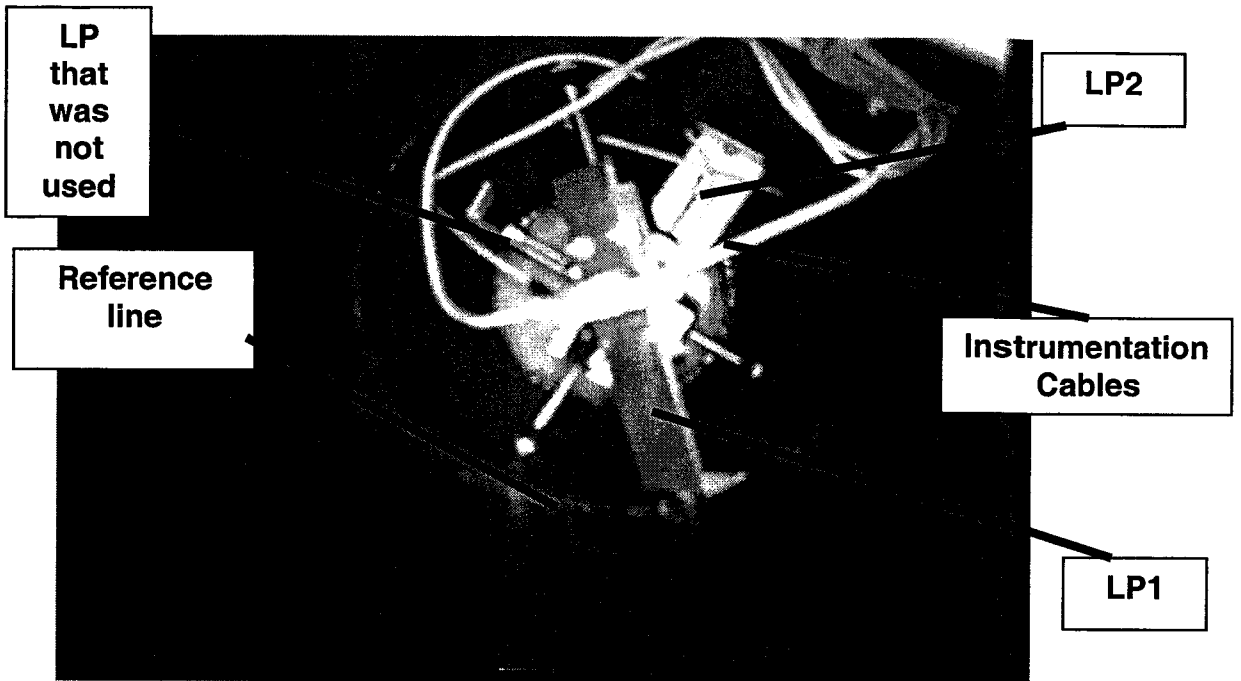


FIGURE 5.33 INFRARED CAMERA IMAGE FROM THE INSIDE OF THE PIPE PRIOR TO ONSET OF BUCKLING DURING TEST T4

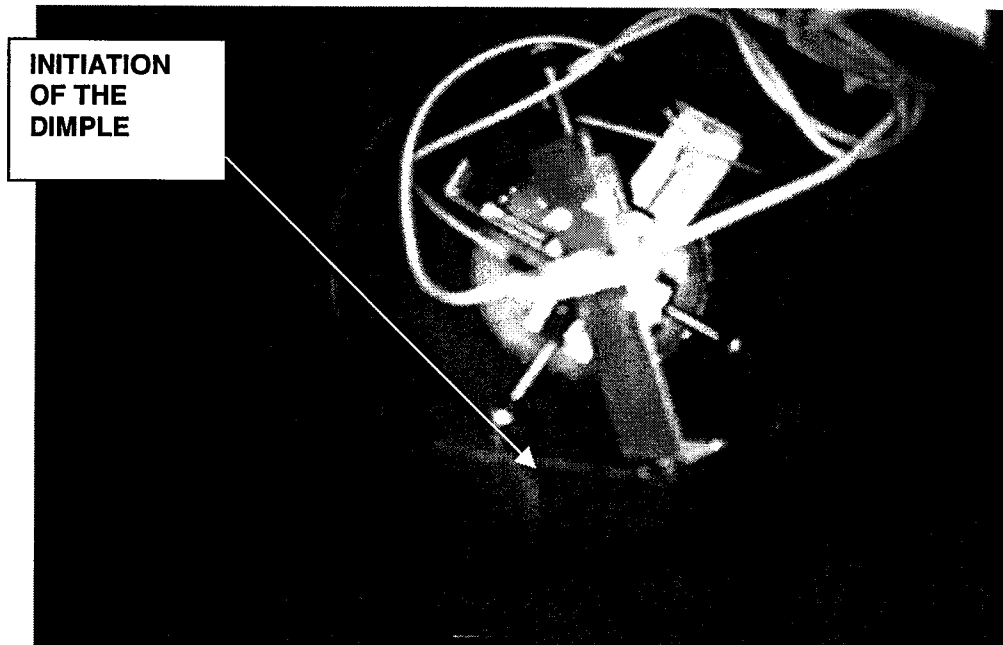


FIGURE 5.34 INITIATION OF THE DIMPLE AT t=6991 SECONDS DURING TEST T4

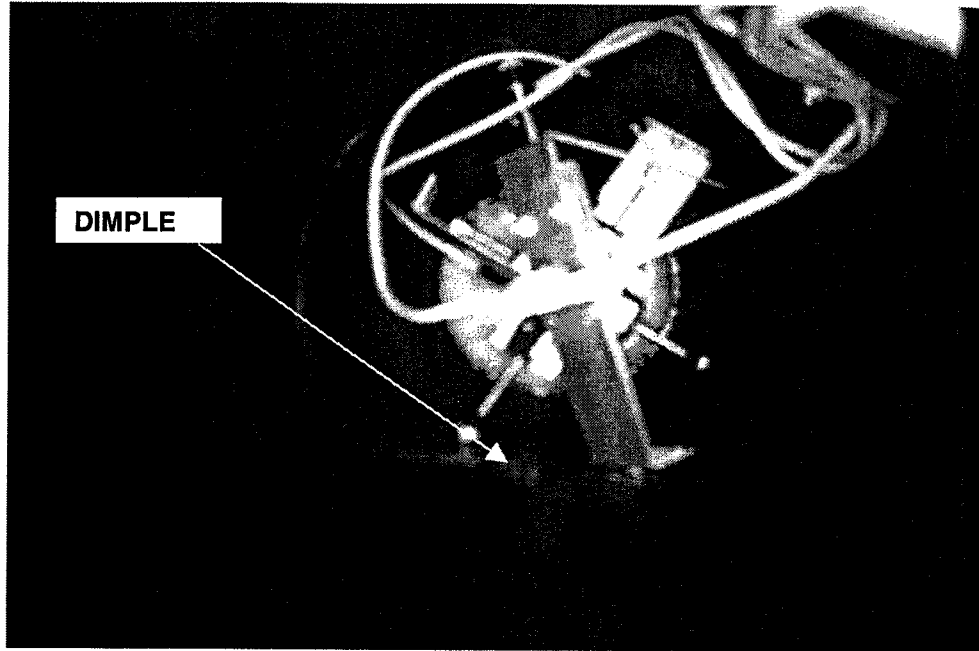


FIGURE 5.35 PROPAGATION OF THE DIMPLE AT $t = 6993$ SECONDS DURING TEST T4

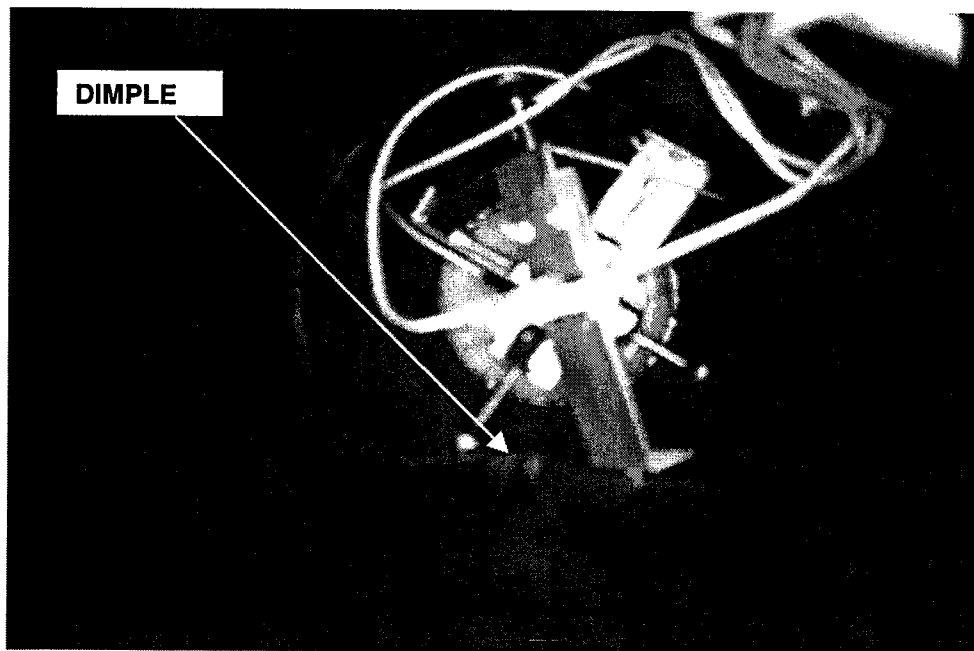


FIGURE 5.36 FINAL DEFORMED PROFILE OF PIPE SHOWING FULL DEVELOPMENT OF THE DIMPLE AT $t = 6995$ SECONDS FOR TEST T4

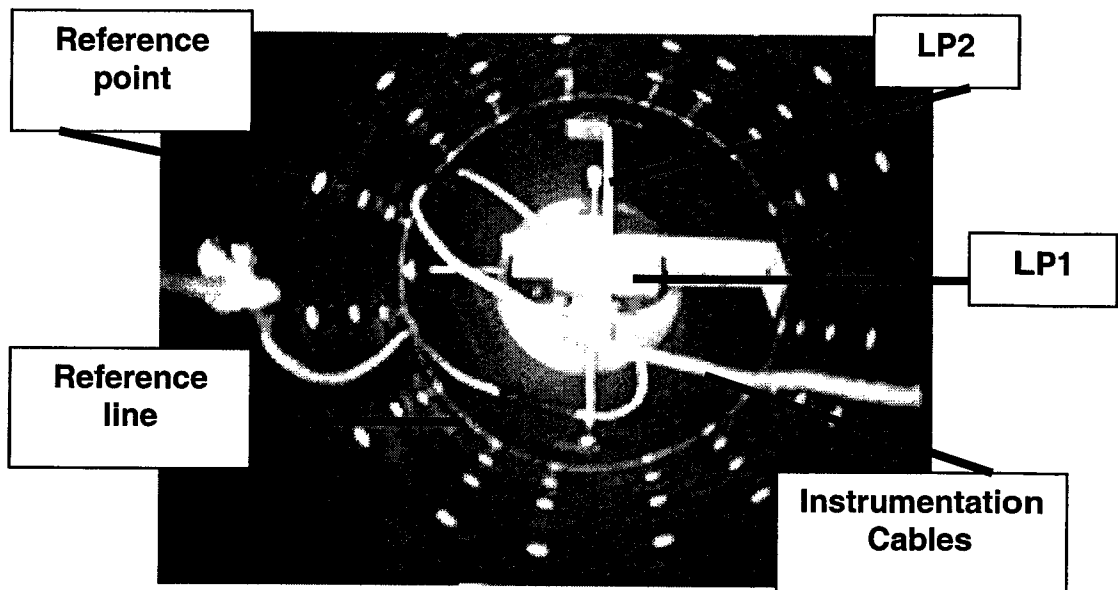


FIGURE 5.37 INFRARED CAMERA IMAGE FROM THE INSIDE OF THE PIPE PRIOR TO ONSET OF BUCKLING DURING TEST T5

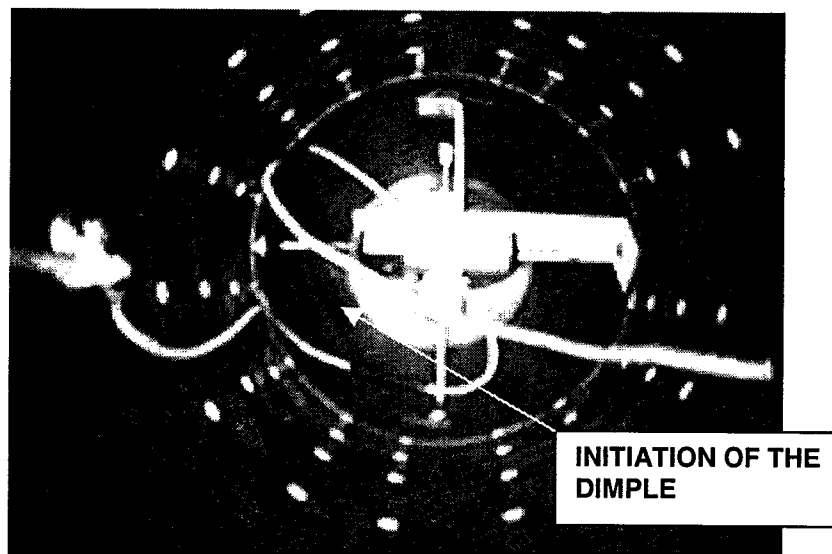


FIGURE 5.38 INITIATION OF THE DIMPLE AT $t=7021$ SECONDS DURING TEST T5

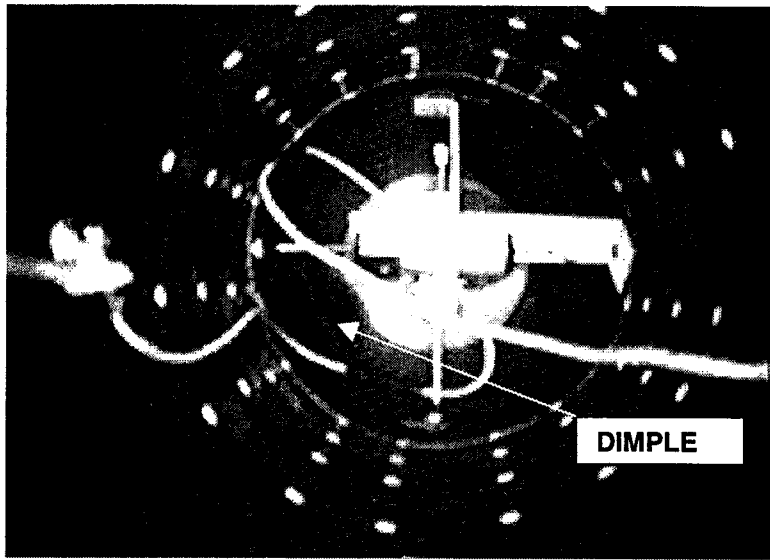


FIGURE 5.39 PROPAGATION OF THE DIMPLE AT $t = 7022$ SECONDS DURING TEST T5

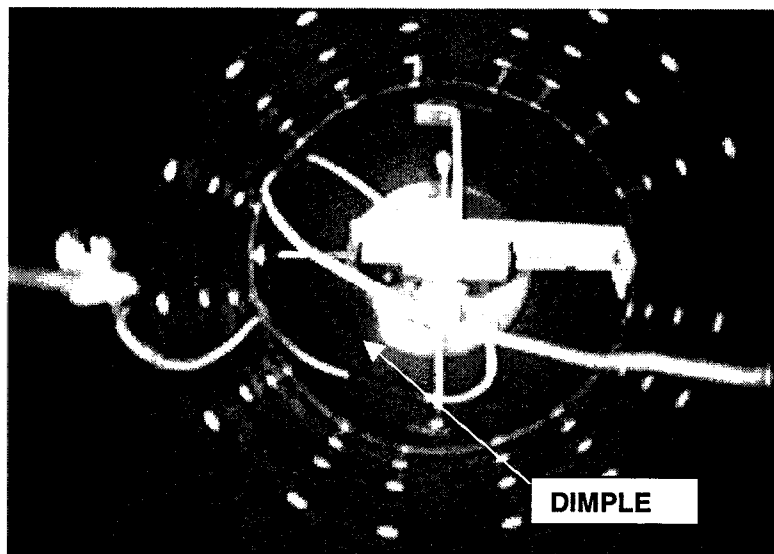


FIGURE 5.40 PROPAGATION OF THE DIMPLE AT $t = 7023$ SECONDS DURING TEST T5

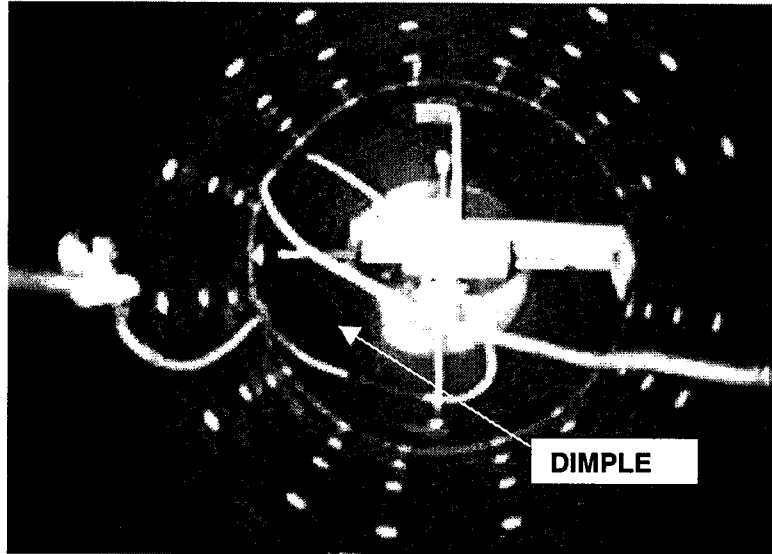


FIGURE 5.41 FINAL DEFORMED PROFILE OF PIPE SHOWING FULL DEVELOPMENT OF THE DIMPLE AT $t = 7025$ SECONDS FOR TEST T5

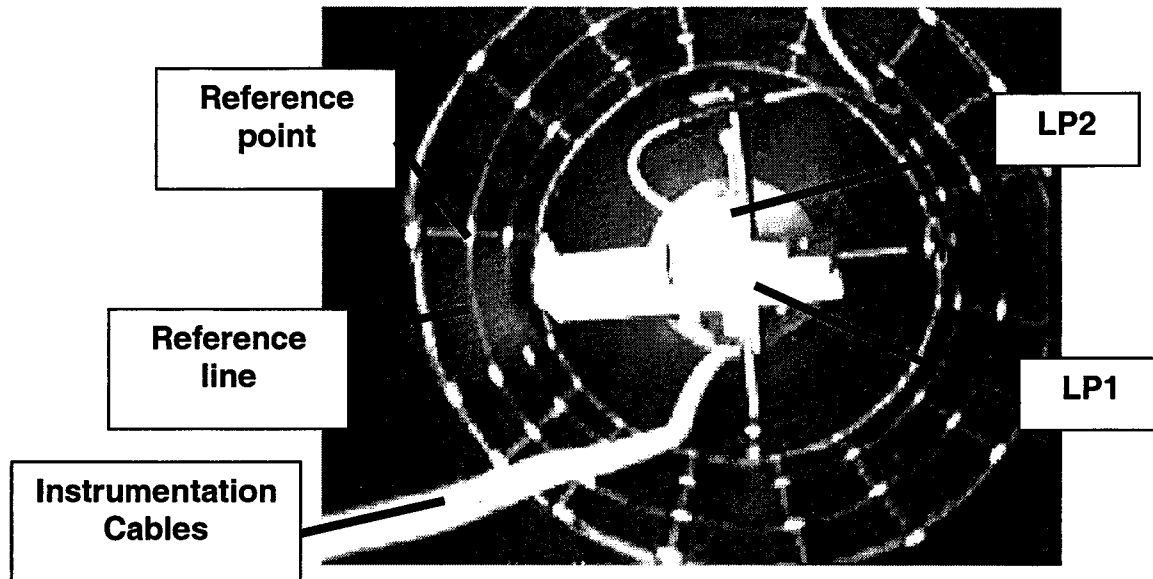


FIGURE 5.42 INFRARED CAMERA IMAGE FROM THE INSIDE OF THE PIPE PRIOR TO ONSET OF BUCKLING DURING TEST T6

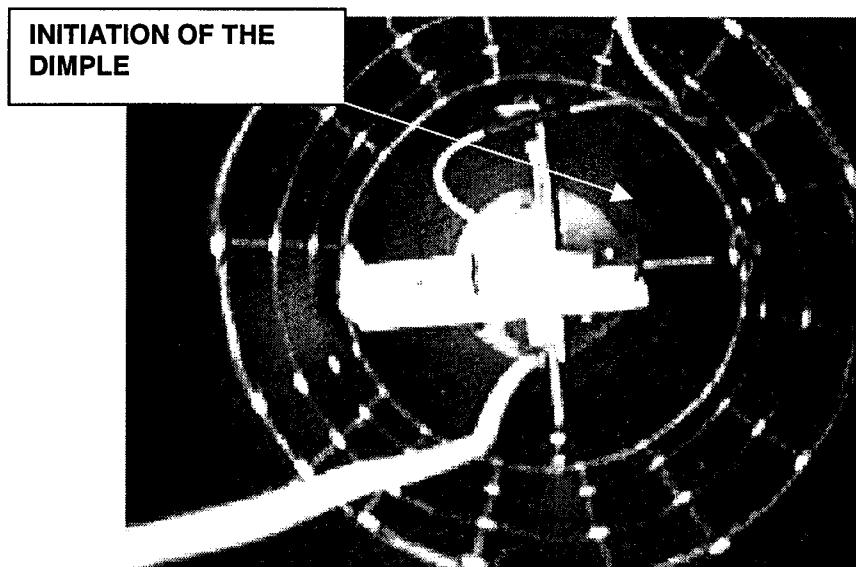


FIGURE 5.43 INITIATION OF THE DIMPLE AT t=12026 SECONDS DURING TEST T6

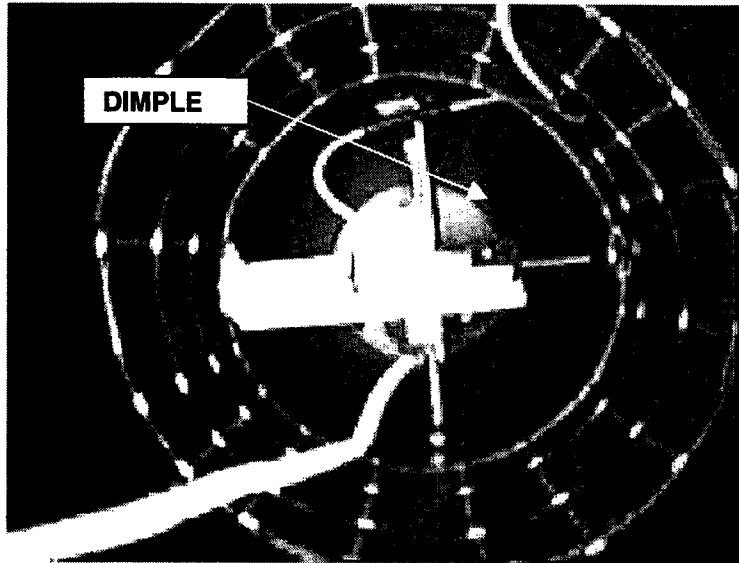


FIGURE 5.44 PROPAGATION OF THE DIMPLE AT $t = 12027$ SECONDS DURING TEST T6

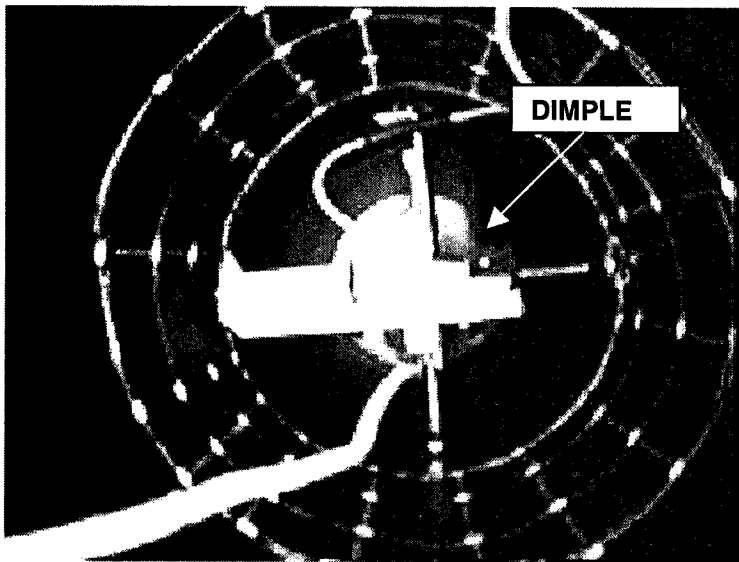


FIGURE 5.45 PROPAGATION OF THE DIMPLE AT $t = 12029$ SECONDS DURING TEST T6

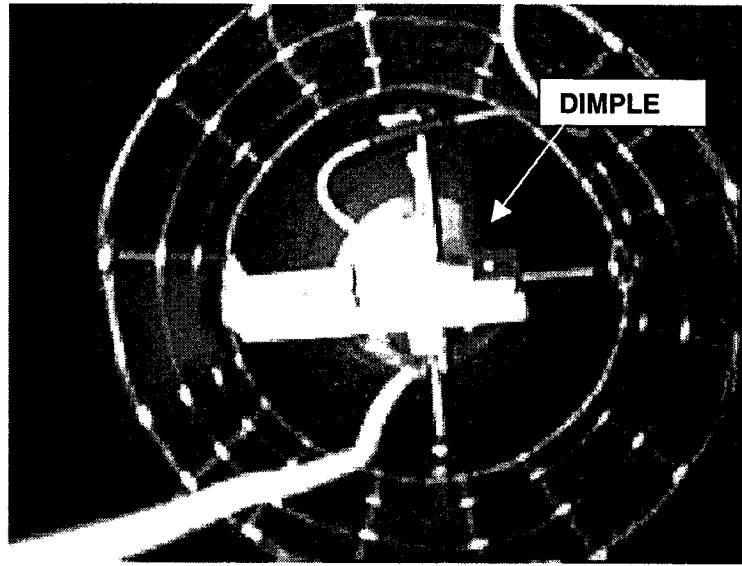
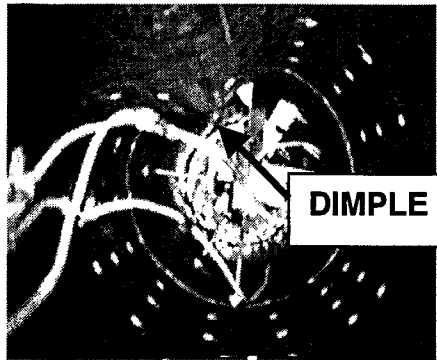
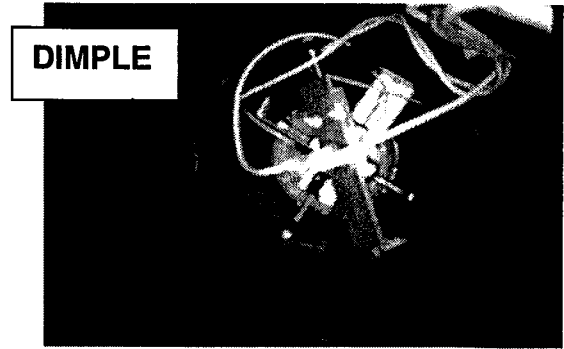


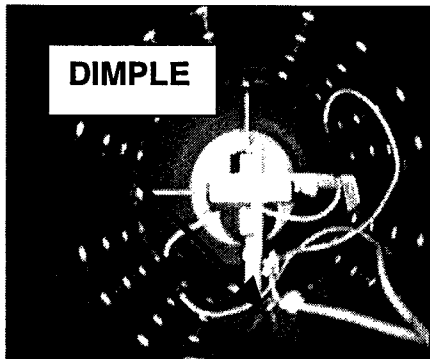
FIGURE 5.46 FINAL DEFORMED PROFILE OF PIPE SHOWING FULL DEVELOPMENT OF THE DIMPLE AT $t = 12031$ SECONDS FOR TEST T6



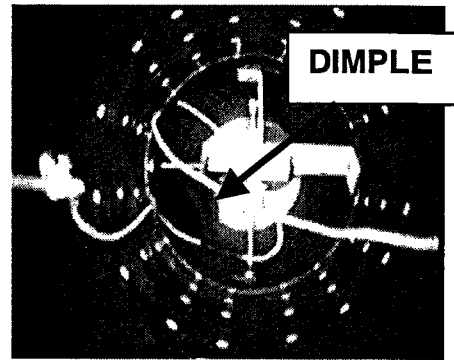
(a) TEST T1



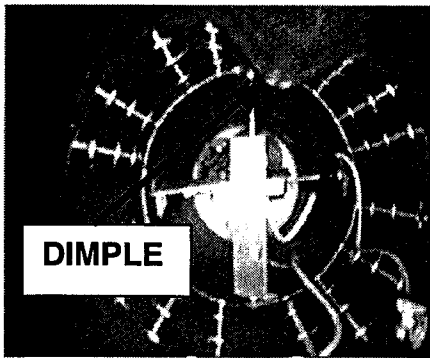
(d) TEST T4



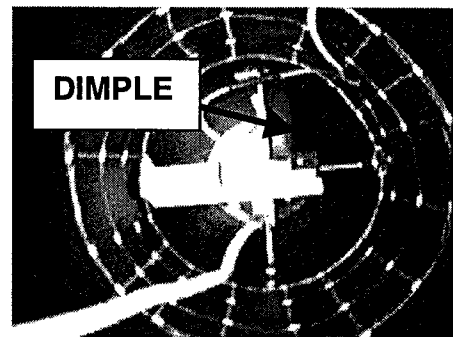
(b) TEST T2



(e) TEST T5

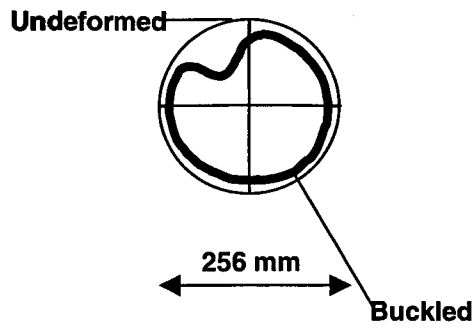


(c) TEST T3

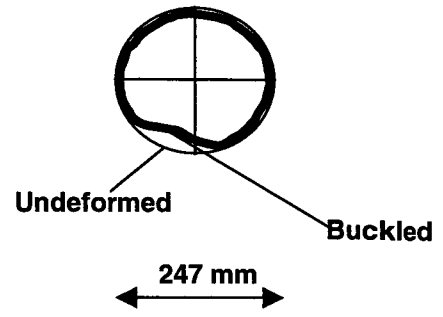


(f) TEST T6

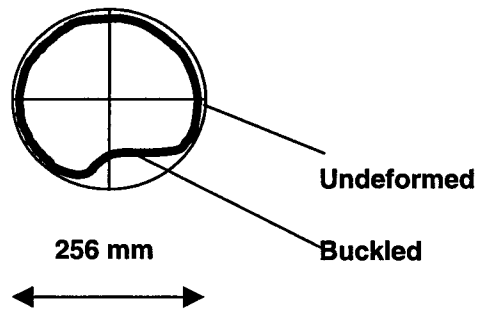
FIGURE 5.47 PHOTOS OF THE BUCKLED PIPES FOR ALL TESTS



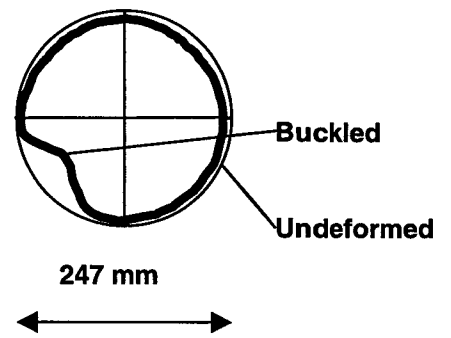
(a) TEST T1



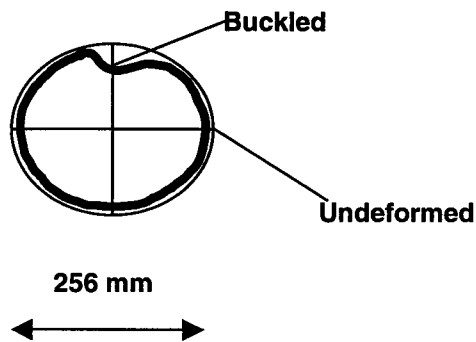
(d) TEST T4



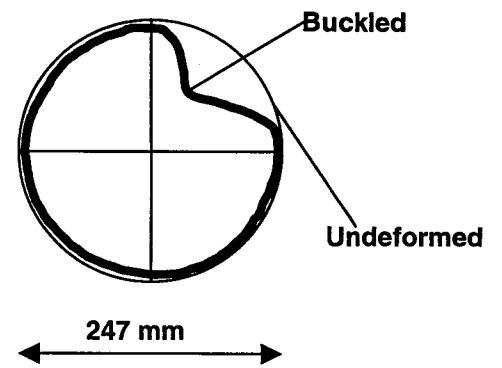
(b) TEST T2



(e) TEST T5



(c) TEST T3



(f) TEST T6

FIGURE 5.48 SKETCHES OF THE UNDEFORMED AND BUCKLED SHAPE OF THE PIPES

6. Discussion

6.1 Introduction

Chapter 5 presented the results of tests with controlled values of bladder pressure P and pore pressure u up to buckling failure. The diameter changes were measured and images of buckled shape were presented. The objective of this Chapter is to explain the conditions leading to buckling failure of the pipe under earth and fluid pressures.

In order to understand the pipe response up to buckling it is necessary to know the stresses that acted on the pipe, namely the effective contact pressure $P'c$ and pore pressure u . The magnitude of $P'c$ is unknown and it depends on the stiffness of the soil, the stiffness of the pipe and the applied stresses. In this Chapter the magnitude of $P'c$ is calculated from the measured diameter change, the applied pore pressure u and an estimated magnitude of pipe secant modulus E_p . The effective contact pressures during the experiments are then examined to clarify the buckling mechanisms under combined earth and fluid pressures.

6.2 Contact pressures

6.2.1 First stage of the tests: Application of bladder pressure with zero fluid pressure

During the first stage of the tests, the applied bladder pressures compressed the soil transmitting radial pressures to the pipe with zero pore pressures acting in the soil. As described in Section 3.2, the magnitude of the contact pressure acting on the pipe during this stage depends on the applied bladder pressure, the stiffness of the soil and the stiffness of the pipe. Because the pore pressures are kept equal to zero, the total contact pressure acting on the pipe P_c was equal to the effective contact pressure P'_c . The total contact pressure P_c can thus be calculated from the measured radial deflections during the tests.

It is important to know whether axial plane stress or plane strain conditions prevailed during this stage of the test in order to calculate the total contact pressures P_c . The application of bladder pressure with zero fluid pressure caused inward radial deflection and axial elongation of the pipe under axial plane stress conditions. The highest value of calculated pipe axial elongation for all the six tests was equal to 7 mm. This magnitude of axial elongation was possible due to: (a) compression of the sand placed between the end cap of the pipe and the lid (refer back to Figure 4.10(b) for details) and (b) the presence of an intentional 5 mm gap between the top of the sand layer and the lid. The gap was required to place the lid such that a proper seal

was attained for the bladder. Consequently, the pipe was under axial plane stress conditions during this stage of the tests.

The total contact pressure P_c acting on the pipe can be estimated from the measured radial deflections. As it is illustrated in Figure 6.1, under axial plane stress conditions ($\sigma_{zz} = 0$), the inward radial deflection of the pipe ω_r when subject to external radial pressure P_c is given by:

$$\omega_r = (P_c r_p^2) / (E_p t_p) \quad (\text{Eq.6.1})$$

Where: r_p is the pipe radius, E_p is the pipe modulus and t_p is the pipe thickness. Positive values of ω_r correspond to inward radial deflection of the pipe. The total contact pressure P_c can then be calculated from the measured deflections and the pipe properties using:

$$P_c = (E_p t_p \omega_r) / (r_p^2) \quad (\text{Eq.6.2})$$

6.2.2 Second stage of the tests: Simultaneous application of bladder and fluid pressure

During the second stage of the tests, not only the bladder pressure but also the pore pressure was increased, thereby introducing additional radial and axial compression to the pipe as it is shown in Figure 6.2. Here the total contact pressure acting on the pipe P_c was equal to sum of the effective contact pressure P'_c and the applied pore pressure u .

The radial deflection of the pipe ω_r during this stage consisted of:

$$\omega_r = \omega_{P'_c} + \omega_{ur} + \omega_{uz} \quad (\text{Eq. 6.3})$$

where: $\omega_{P'c}$ is the inward radial deflection due to the effective contact pressure $P'c$, ω_{ur} is the inward radial deflection due to the pore pressure u acting radially, and ω_{uz} is the outward radial deflection caused by the pore pressure u acting axially.

Since the applied pore pressure u is known the values of ω_{ur} and ω_{uz} can be calculated using the following equations:

$$\omega_{ur} = (u r_p^2) / (E_p t_p) \quad (\text{Eq. 6.4})$$

$$\omega_{uz} = - (u v_p r_p^2) / (2 t_p E_p) \quad (\text{Eq. 6.5})$$

Knowing the magnitude of ω_{ur} , ω_{uz} , and the measured value of ω_r during the tests, the radial deflection from $P'c$ can be found by:

$$\omega_{P'c} = \omega_r - \omega_{ur} - \omega_{uz} \quad (\text{Eq. 6.6})$$

The effective contact pressure $P'c$ can then be calculated from:

$$P'c = (E_p t_p \omega_{(P'c)}) / (r_p^2) \quad (\text{Eq.6.7})$$

The total contact pressure acting on the pipe is the sum of $P'c$ and u .

6.2.3 Pipe modulus

Values of pipe modulus E_p are required for the high-density polyethylene (HDPE) pipe to permit calculation of the contact pressures. HDPE exhibits a non-linear visco-plastic behavior. Zhang and Moore (1997a,b) performed a series of tension and compression tests with samples of HDPE revealing that the behavior of this material is highly non-linear and time dependent. However, the contact pressures can be calculated from the measured deflections provided that an appropriate secant modulus E_p is used.

The modulus E_p , together with Poisson's ratio ν_p (ν_p is equal to 0.46 for HDPE from Zhang and Moore, 1997a,b) relates the stresses and strains of the material. The circumferential strains can be calculated from the measured pipe deflections. The stresses caused by those strains can be calculated using the viscoplastic constitutive model of Zhang and Moore. The modulus can then be estimated from the known stresses and strains.

Hoop strains of the pipe ($\epsilon_{\theta\theta}$) were first calculated from the measured pipe deflections. Under radially symmetric conditions ($\delta\omega_r / \delta\theta = 0$), the circumferential strain is equal to the internal diameter change divided by the initial internal diameter:

$$\epsilon_{\theta\theta} = \Delta D_{pi} / D_{pi} \quad (\text{Eq. 6.8})$$

where:

$\epsilon_{\theta\theta}$ is the circumferential strain at the internal surface of the pipe,

ΔD_{pi} is the internal pipe diameter change, and

D_{pi} is the initial internal pipe diameter.

An HDPE square block of unit dimensions was then modeled using the finite element program WANFE® (Moore 1996) as illustrated in Figure 6.3 (a). The block represents a small portion of the pipe in the z - θ plane. Figure 6.3 (b) shows the relative location and orientation of the block. The plane AB-CD is part of the internal pipe wall. Segments AD and DC were modeled as smooth rigid boundaries therefore restrained in the z and θ direction

respectively. The segments AB and BC are free to deform in the θ and z directions respectively.

For each test, the maximum value of circumferential strain $\epsilon_{\theta\theta}$ (prior to buckling) was imposed to the boundary AB of the HDPE block at the correspondent average strain rate of the test. Table 6.1 summarizes the maximum circumferential strains, duration and strain rate for each test. The lowest strain rate was 4.1×10^{-6} %/sec and the highest was 6.3×10^{-6} %/sec. The average value was 4.95×10^{-6} %/sec.

The circumferential and axial stresses $\sigma_{\theta\theta}$ and σ_{zz} were then calculated from the prescribed strains using the visco-plastic of Zhang and Moore (1997a,b). From the prescribed strains and calculated stresses, the secant modulus E_p was estimated for different magnitudes of $\sigma_{\theta\theta}$ and σ_{zz} level using:

$$E_p = (\sigma_{\theta\theta} - \nu_p \sigma_{zz}) / \epsilon_{\theta\theta} \quad \text{(Eq. 6.9)}$$

The calculated secant modulus E_p was equal to the total stress divided by the total strain. The stresses $\sigma_{\theta\theta}$ and σ_{zz} were calculated assuming axial plane stress $\sigma_{zz} = 0$. Interestingly, the same values of E_p were calculated for axial plane strain conditions. Thus the axial end conditions do not influence the material response of the HDPE.

For each test, the variation of E_p with time was calculated. Figure 6.4 is a plot of the calculated pipe modulus E_p versus time. Very similar results were obtained for each test and this is the reason of why the same pressure interval was used for each test. It can be appreciated in Figure 6.4 an abrupt

decrease of the modulus from 1440 MPa to 600 MPa, which occurs for every test, in the first 500 seconds. For test T6, E_p dropped to 200 MPa in only 12000 seconds (200 minutes).

6.3 Interpretation of soil-structure interaction

6.3.1 Calculated contact pressures

Values of the total contact pressure P_c , the effective contact pressure P'_c and the pore pressure u acting on the pipe can be calculated using Equations 6.2, 6.4, 6.5, 6.6 and 6.7 to understand the conditions leading to buckling of the pipe under fluid and earth pressures.

Figures 6.5 to Figure 6.9 are plots of total contact pressure P_c , effective contact pressure P'_c and pore pressure u in order to show the load path of these pressure components and their influence on the pipe buckling phenomena for tests T1, T2, T3, T5 and T6 respectively. These plots also include the load path of the applied effective pressure P' (bladder pressure minus the pore pressure) versus time in order to illustrate the arching phenomena in the soil.

In test T4 conducted with a DR 21 pipe with an effective pressure P' equal to 100 kPa, two measurements of deflection were made. One of them showed an extremely high value of deflection and the other a very low magnitude of this parameter and due to this inconsistency the contact

pressures for this test were not calculated. Possible explanations for the inconsistent deflection measurements from this test were given in Chapter 5.

6.3.2 Typical results

Similar trends of the pipe contact pressures P_c , effective contact pressures P'_c and pore pressure u , were found for all of the tests. Therefore one set of results shown in Figure 6.9, for the test T6 with a DR 21 pipe and an applied effective stress P' equal to 1000 kPa, will be used to describe the pressures acting on the pipe up to buckling.

6.3.2.1 First stage of the test

Figure 6.9 shows for Test T6 that during the first stage of the test from 0 to 5000 seconds the effective bladder pressure P' was raised to a maximum value of 1000 kPa while the pore pressure u was kept equal to zero.

The effective contact pressure P'_c that reached the pipe is a fraction of the effective bladder pressure P' . The arching factor A' is equal to the load that reached the pipe P'_c divided by the effective bladder pressure P' . In the interval of 0 to 5000 seconds, the arching factor A' decreased as P' increased. This occurred because the soil became stiffer as the magnitude of P' increased therefore the soil attracted a higher proportion of the load from the bladder than that transmitted to the pipe. At time 5000 seconds the contact pressure P'_c was equal to 500 kPa and the effective bladder pressure P' was equal to 1000 kPa therefore the arching factor A' was equal to 0.5.

Table 6.2 shows, for each test (T1, T2, T3, T5 and T6), the effective bladder pressure P' , the duration of the first stage of the test, the effective contact pressure P'_c and the arching factor A' . The arching factor decreased as P' increased. For example, for tests T1, T2 and T3, performed with P' equal to 100 kPa, 300 kPa and 1000 kPa respectively and values of arching factor A' of 1.0, 0.6 and 0.4 were obtained at the end of the first stage. Again as the magnitude of applied effective bladder pressures P' increases, the arching factor A' decreases because of increasing soil stiffness.

It was also expected that the arching factor increased for lower values of pipe DR. A lower DR value (i.e. thicker pipe) results in a stiffer pipe, therefore the pipes will attract more load. This trend can be observed when the arching factors A' for test T3 and T6 are compared (Table 6.2). Both test were performed with a $P' = 1000$ kPa and correspondent arching factors A' of 0.4 and 0.5 were obtained for tests T3 and T6. Test T6 was performed with a stiffer pipe (DR 21) than the pipe used for test T3 (DR 32.5) therefore the arching factor A' was higher for test T6. However when the arching factors A' for tests T2 and T5 are compared the opposite is observed. Both tests were performed with tests with a $P' = 300$ kPa and values of arching factor A' of 0.6 and 0.26 were obtained respectively for tests T2 and T5. Test T2 was performed with a DR 32.5 pipe therefore it should attract less load than the DR 21 pipe used in test T5. There is no apparent reason for this opposite trend in arching factor A' for tests T2 and T5.

6.3.2.2 Second stage of the test

For test T6 (Figure 6.9) the second stage started at approximately 5500 seconds. During this stage both bladder pressure P and pore pressures u were raised simultaneously keeping the difference between both parameters constant. Therefore the value of effective bladder pressure P' was kept constant during the entire second stage of the test.

Between 5500 and 10000 seconds the effective contact pressure P'_c decreased even though the applied effective pressure P' remained constant. This occurred because the pore pressure u caused additional compression of the pipe in the radial direction leading to a further redistribution of stresses. Arching or redistribution of stresses is dependent on the relative deformations of the pipe and the disk of soil that the pipe replaces. The higher the deformation of the pipe relative to the disk of soil, the less magnitude of load will reach the pipe.

The observed decrease in P'_c is explained in reference to Figure 6.10. A hypothetical situation is illustrated in Figure 6.10 (a) (showing soil only) in which the disk of soil would have deformed in the radial direction under the effective bladder pressure P' that was raised during the first stage and kept constant during the second stage of the test. Even if the pore pressures were increased, the deflection of the soil would not have increased provided that P' remained constant. The deformation of the disk of soil should have been

constant throughout the second stage of the test because P' was kept constant.

Throughout the second stage of test T6, the effective bladder pressure P' was kept constant and the pore pressure u was raised inducing additional radial deformations on the pipe as it is illustrated in Figure 6.10 (b). Therefore, under the applied loads the pipe deformed more than the disk of soil resulting in a decrease of P'_c between 5500 and 10000 seconds.

Beyond 10000 seconds the effective contact pressure P'_c was reduced to zero for the same reasons described above. Therefore the total contact pressure P_c was equal to the pore pressure u , i.e. only fluid loads were acting on the pipe up to buckling. Buckling failure occurred at total contact pressure P_c of 1400 kPa. Therefore fluid pressures caused buckling with soil support around the pipe.

The effect of the pore pressures u on the effective contact pressure P'_c confirms the possible explanation of the three distinct slopes that can be appreciated in the deflections plot for test T6 (Figure 5.13). When the pore pressure u started to be increased the slope became less steep indicating a reduction of P'_c . Then when P'_c decreased to zero, only fluid loads acted on the pipe, which was reflected on a steeper slope of the deformation plot.

6.4 Buckling capacity

Currently there is no available solution for pipe buckling under earth and fluid pressure. The tests provided visual observations of single-wave mode of

buckling and trends of effective contact pressure P'_c and pore pressure u . Although the development of a new solution for pipe buckling under earth and fluid pressure is beyond the scope of this thesis, the results from this thesis will be useful in the complete development of a new solution.

A transition of the nature of loads acting on the pipe was observed throughout the tests. In the first stage, only earth loads acted on the pipe. Then, during the second stage, earth and fluid loads acted on the pipe and finally at buckling, only fluid loads acted on the pipe.

Table 6.3 presents the pore pressure at failure for each test and the buckling predictions by Levy (1884). The solution by Levy assumes that fluid loads act on the pipe with no soil support while in the tests buckling occurred due to fluid loads with soil support around the pipe. The solution by Levy predicts a very low buckling capacity in comparison to the test results revealing the additional stability provided by the presence of soil around the pipe. The buckling capacity was increased between 15 to 55 times due to the presence of soil.

It is interesting to see how the capacity beyond $P'_c=0$ compares with the solutions of Cheney (1971) and Glock (1977). Table 6.3 also summarizes the pore pressure at failure and the pore pressure when P'_c is reduced to zero for each test. The difference between the two previous values denoted here as Δu refers to the capacity of the pipe to resist u once P'_c goes to zero. The pipe modulus E_p at failure, which is required to calculate the critical buckling pressures using the equations of Cheney, Glock and Levy, is also

given in Table 6.3 for each test. The additional buckling capacity after P'_c drops to zero is between the predictions given by the equations of Cheney and Glock. The predictions by Cheney overestimate the capacity in the range of 21% to 67% while the predictions by Glock underestimate the capacity in the range of 48% to 66%.

Cheney and Glock equations are single-wave solutions applicable to liners or pipes inside rigid hosts. Both solutions assume that the host resists all outward movement of the pipe while there is no resistance to inward movement. In other words, those solutions assume that the cavity is infinitely rigid. The difference between the solution by Glock and that by Cheney is that the former assumes that the host or cavity does not follow any inward deformation of the pipe while the latter assumes that the cavity moves inward along with the pipe therefore Cheney's prediction of buckling capacity is higher by a factor of 2.5.

None of the tests completely satisfies all the assumptions of the solutions by Cheney and Glock. The soil does follow the pipe up to the point of buckling therefore Cheney's condition of a moving cavity is correct for the specific circumstances of the test but the soil is not infinitely rigid therefore some outward deformation of the pipe is allowed to occur. Figure 6.11 illustrates this explanation.

Although it is interesting the comparability between these solutions and the capacity of the pipe to resist u once P'_c goes to zero, further research is needed to investigate their applicability. It is also important to take into

account that during the tests the radial end constraints of the pipe might have influenced the buckling capacity to an unknown extent. Therefore general conclusions should not be extracted from comparisons between the test results and known buckling solutions.

6.5 Summary

For purposes of analysis every test was divided in two stages. The first stage, which consisted of the application of ground loads with zero pore pressure, caused radial compression of the pipes under conditions of axial plane stress. The calculated effective contact pressure P'_c was compared with the effective bladder pressure P' allowing for observations regarding the arching phenomena to be made for this stage. In general it was found that as P' increased the pipe received less load as a result of the increasing soil stiffness.

The second stage of the tests consisted of the application of ground and fluid loads. The effective contact pressure P'_c caused radial compression of the pipe but the pore pressure u caused radial and axial compression of the pipe. The resulting outward radial deflection of the pipe had to be taken into account to calculate the contact pressures during this stage.

The calculation of the contact pressures from the measured pipe deformations needed to take into account the highly non-linear and time dependent behavior of high-density polyethylene (HDPE). A stress-strain

analysis of the HDPE was made in the finite element program WANFE® (Moore 1996) taking into account the strain rates used for the tests.

The calculation of the contact pressures revealed a decrease of the effective contact pressure P'_c to zero as a result of the increase in pore pressure u . Buckling occurred with only fluid pressures acting on the pipe. A comparison between the fluid pressures at buckling and the buckling predictions by the solution of Levy revealed that the presence of soil increased the buckling capacity between 15 and 55 times. The solution by Glock (1977) underestimates the capacity of the pipe beyond $P'_c = 0$. On the other hand, the solution by Cheney (1971) overestimates the capacity. These solutions are not applicable for the case of pipe buckling under fluid loads with soil support but may be used to bound the buckling capacity.

TEST	PIPE STRAIN %	TIME (sec)	STRAIN RATE
T1	1.44	3000	4.94×10^{-6}
T2	2.76	6000	4.6×10^{-6}
T3	4.46	9000	4.96×10^{-6}
T4	4.39	7000	6.3×10^{-6}
T5	2.86	7000	4.1×10^{-6}
T6	5.81	12000	4.84×10^{-6}

TABLE 6.1 MAXIMUM PIPE STRAIN, TEST DURATION AND STRAIN RATE FOR EACH TEST.

Test	DR	P' (kPa)	End of first stage (sec)	P'c at end of first stage (kPa)	A' at the end of the first stage
T1	32.5	100	600	100	1.0
T2	32.5	300	2100	180	0.6
T3	32.5	1000	4500	400	0.4
T5	21	300	2200	78	0.26
T6	21	1000	5100	500	0.5

TABLE 6.2 PIPE DR (DIAMETER TO THICKNESS RATIO), EFFECTIVE BLADDER PRESSURE P' AT WHICH EVERY TEST WAS CONDUCTED, INSTANT WHEN THE FIRST STAGE ENDED, EFFECTIVE CONTACT PRESSURE P'c AT THE END OF THE FIRST STAGE, ARCHING FACTOR A' AT THE END OF THE FIRST STAGE

TEST	Pore Pressure ($p_{c=0}$) [kPa]	Pore Pressure ($p_{c=0}$) [kPa]	Pore Pressure ($p_{c=0}$) - Pore Pressure ($p_{c=0}$) [kPa]	E_p ($p_{c=0}$) (MPa)	Cheney solution [kPa]	Glock solution [kPa]	Levy solution (kPa)
T1	680	300	380	420	636	252	31
T2	750	400	350	316	470	191	23
T3	950	700	250	229	343	137	17
T5	1200	300	900	278	1088	434	76
T6	1400	1000	400	168	658	263	46

TABLE 6.3 PORE PRESSURE AT BUCKLING, PORE PRESSURE WHEN $p_{c=0}$ DROPS TO ZERO, DIFFERENCE BETWEEN THE PORE PRESSURE AT BUCKLING AND THE PORE PRESSURE WHEN $p_{c=0}$ DROPS TO ZERO, PIPE MODULUS AT BUCKLING, BUCKLING PREDICTIONS BY CHENEY, GLOCK AND LEVY.

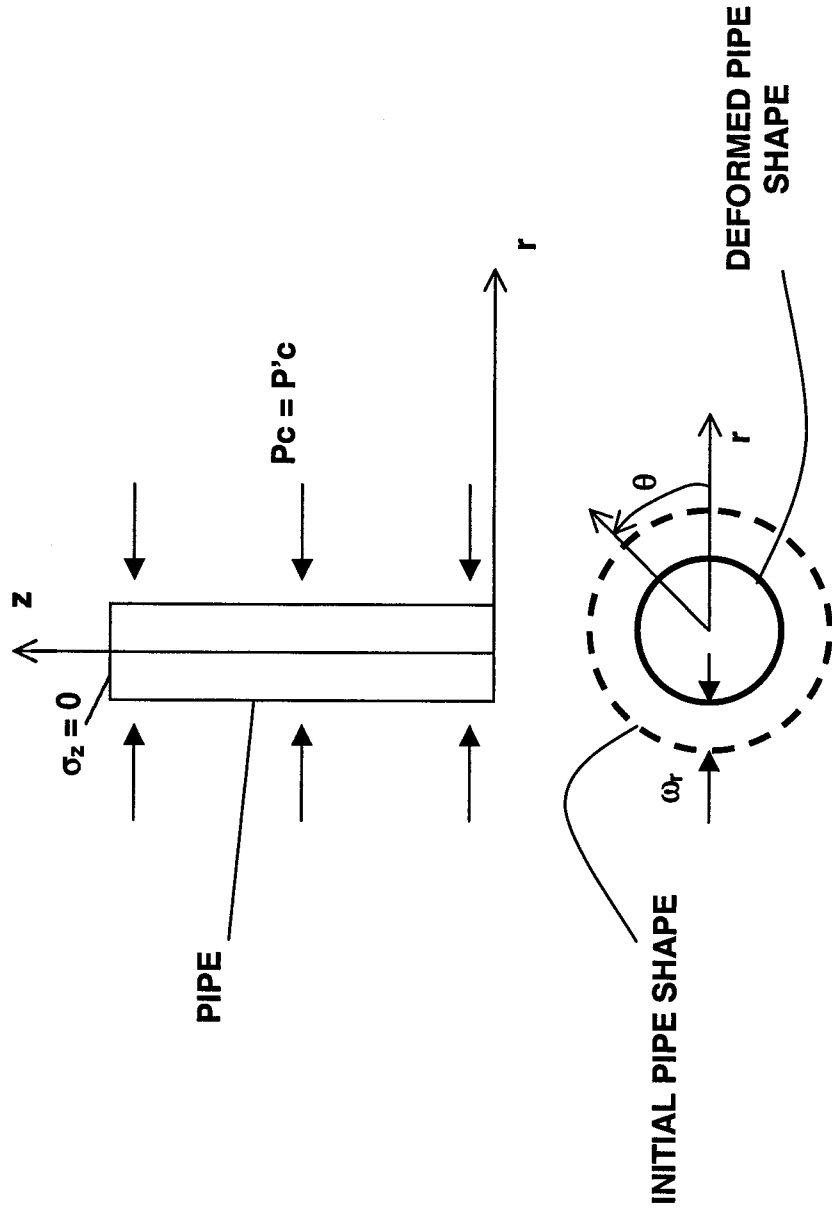


FIGURE 6.1 ILLUSTRATION OF THE FIRST STAGE OF THE TESTS SHOWING INWARD RADIAL DEFORMATIONS RESULTING FROM A PIPE UNDER RADIAL EFFECTIVE CONTACT STRESSES $P'c$ AND ZERO AXIAL STRESSES σ_z

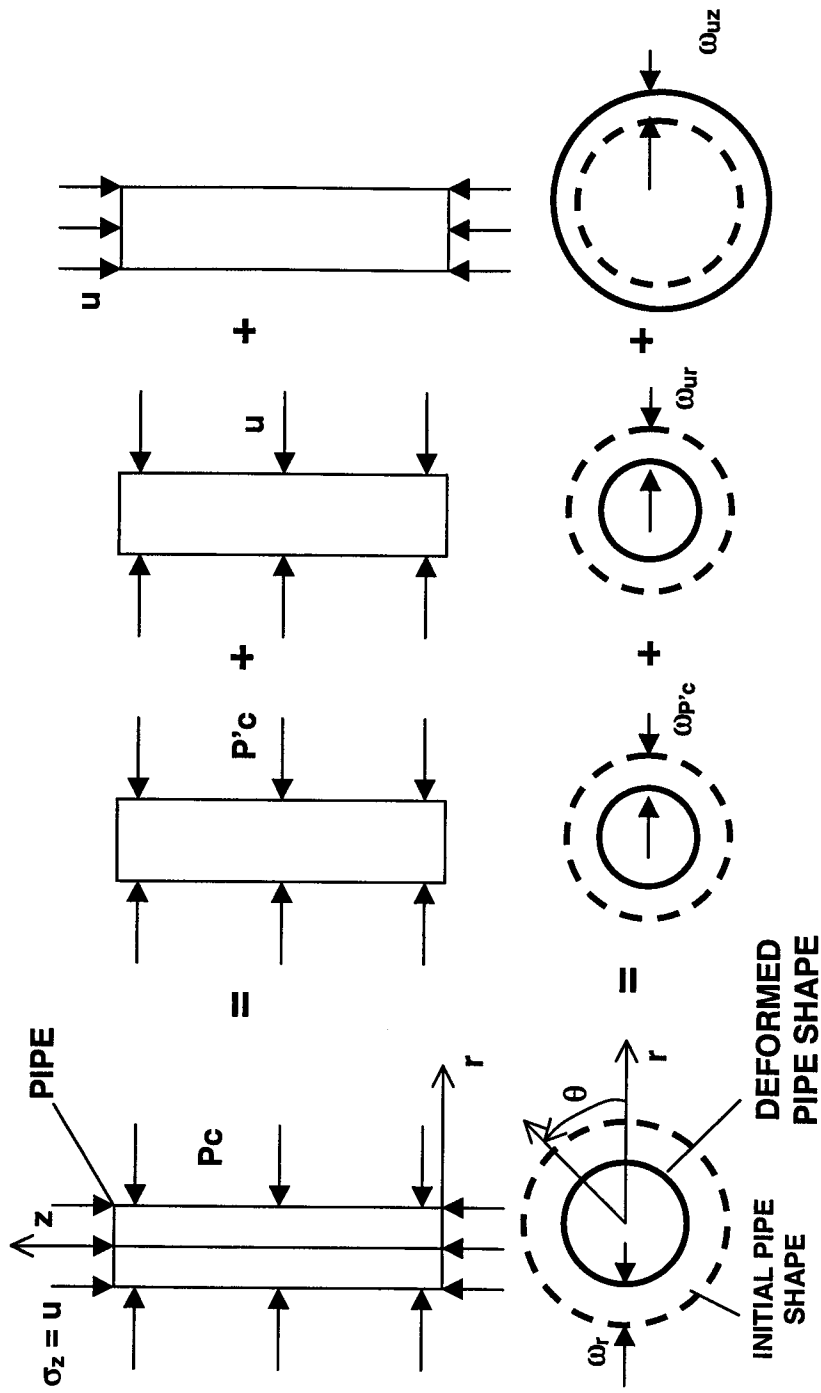
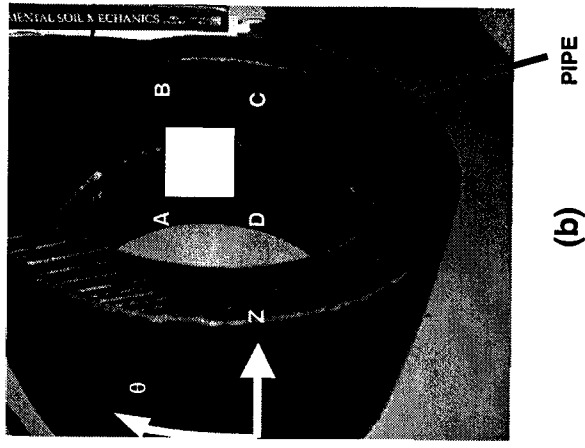
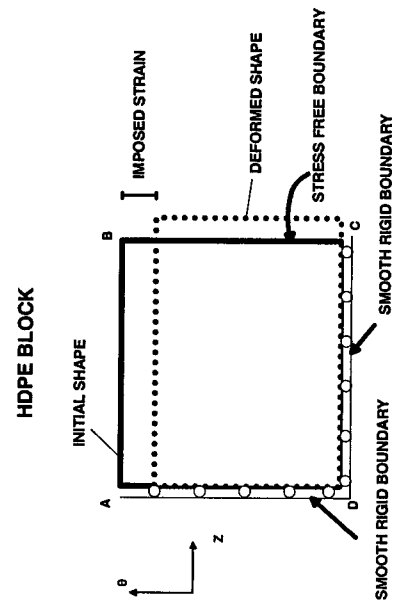


FIGURE 6.2 SECOND STAGE OF THE TEST SHOWING THE RADIAL CONTACT PRESSURE $P'c$ AND AXIAL PORE PRESSURE u ACTING ON THE PIPE RESULTING IN A NET INWARD RADIAL DEFORMATION. THE RADIAL EFFECTIVE CONTACT PRESSURE $P'c$ AND THE RADIAL PORE PRESSURE u PRODUCE INWARD RADIAL DEFORMATIONS WHILE THE PORE PRESSURE u ACTING AXIALLY PRODUCES OUTWARD RADIAL DEFORMATIONS



(b) PIPE



(a)

**FIGURE 6.3 (a) SQUARE HDPE BLOCK OF UNIT DIMENSIONS MODELLED TO CALCULATE STRESSES
(b) LOCATION AND ORIENTATION OF THE BLOCK IN THE PIPE**

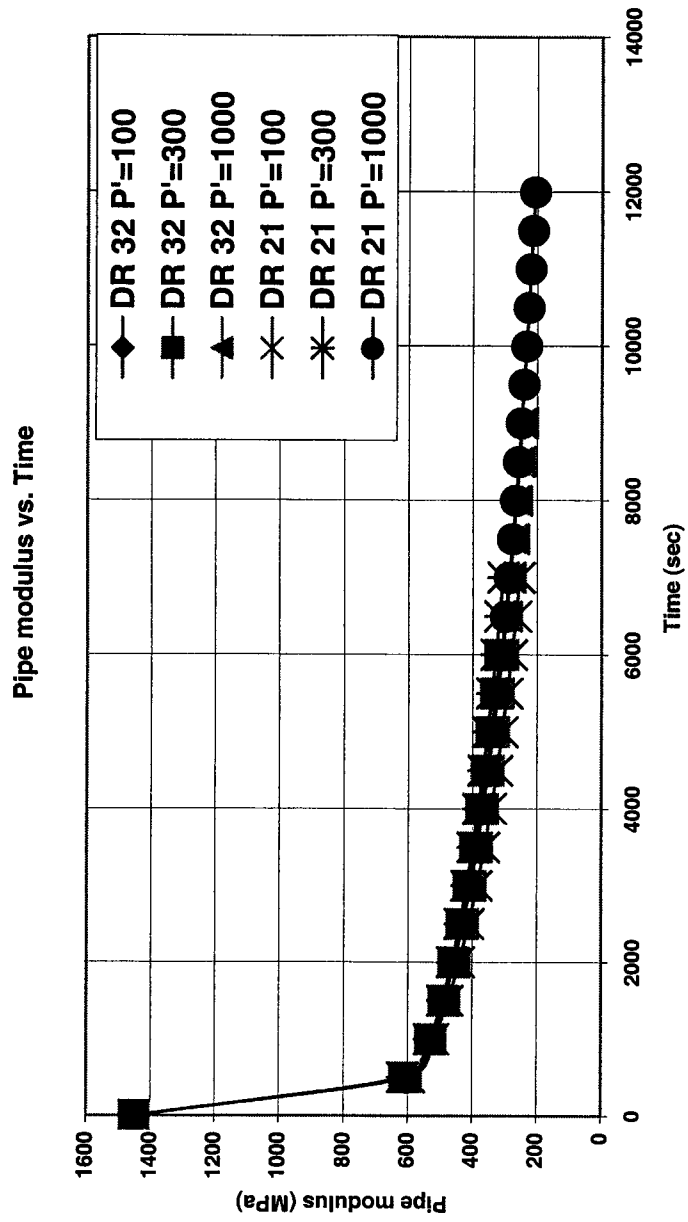


FIGURE 6.4 CALCULATED PIPE MODULUS E_p VERSUS TIME FOR THE SIX TESTS

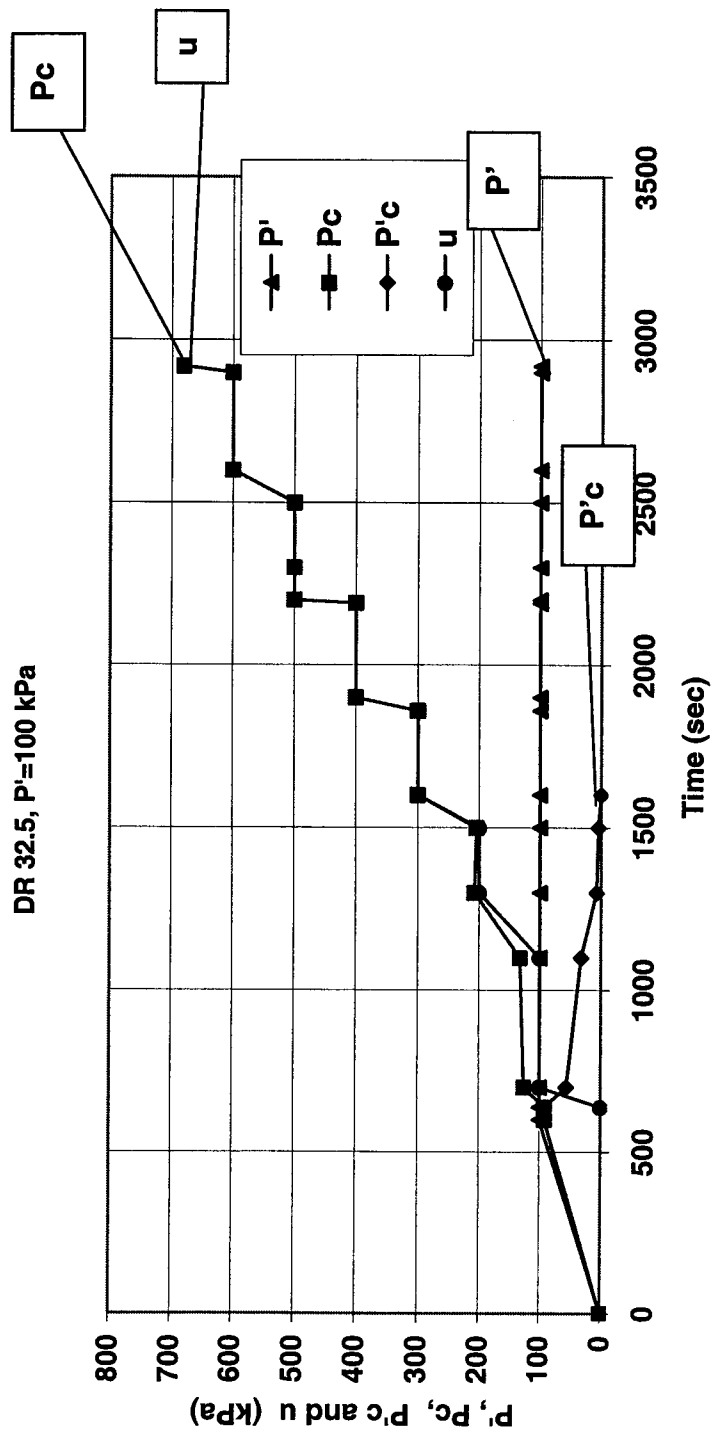


FIGURE 6.5 LOAD PATH OF THE EFFECTIVE BLADDER PRESSURE P' , THE TOTAL CONTACT PRESSURE P_c , THE EFFECTIVE CONTACT PRESSURE P'_c AND THE PORE PRESSURE u FOR TEST T1.

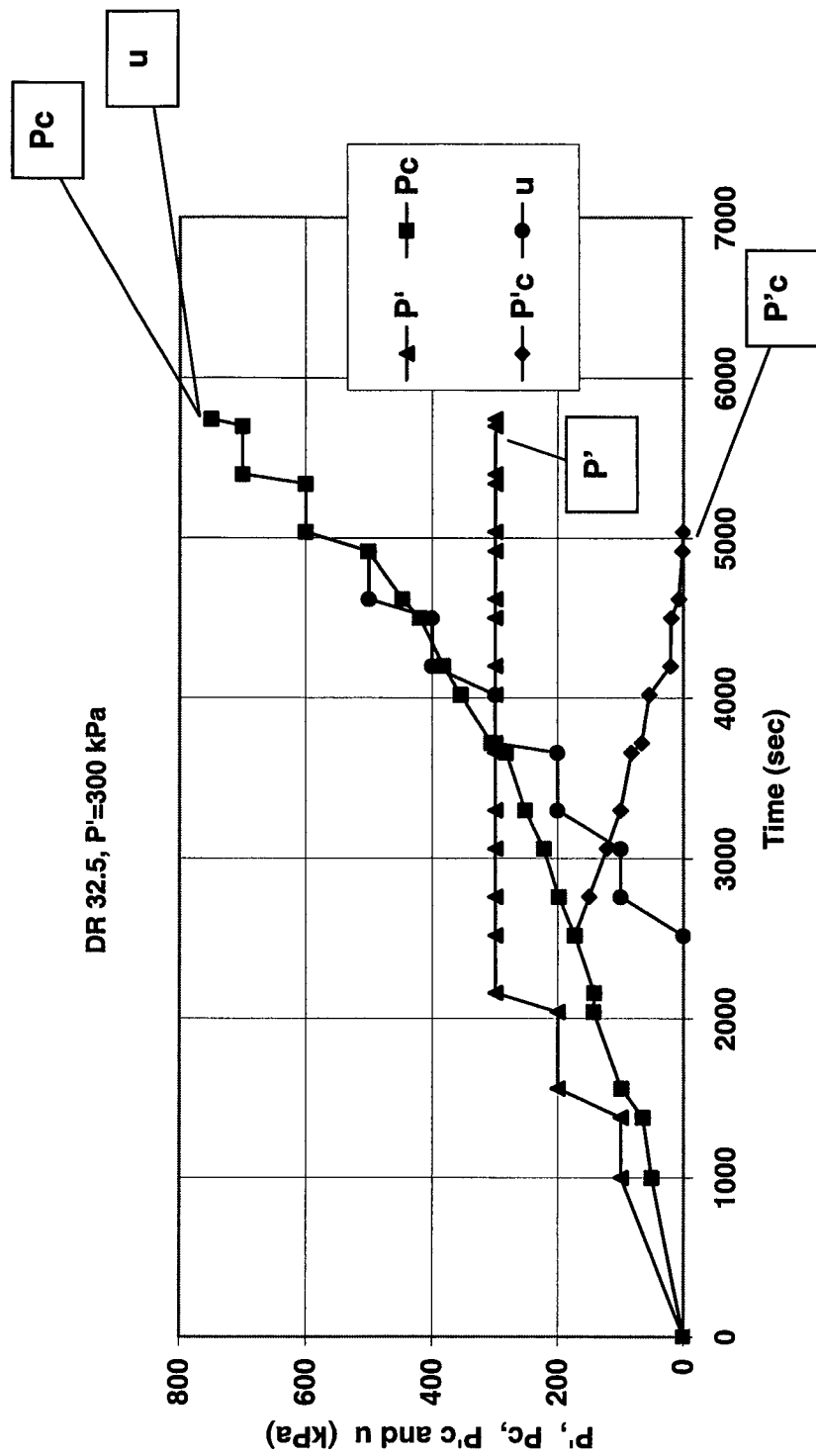


FIGURE 6.6 LOAD PATH OF THE EFFECTIVE BLADDER PRESSURE P', THE TOTAL CONTACT PRESSURE Pc, THE EFFECTIVE CONTACT PRESSURE P'c AND THE PORE PRESSURE u FOR TEST T2

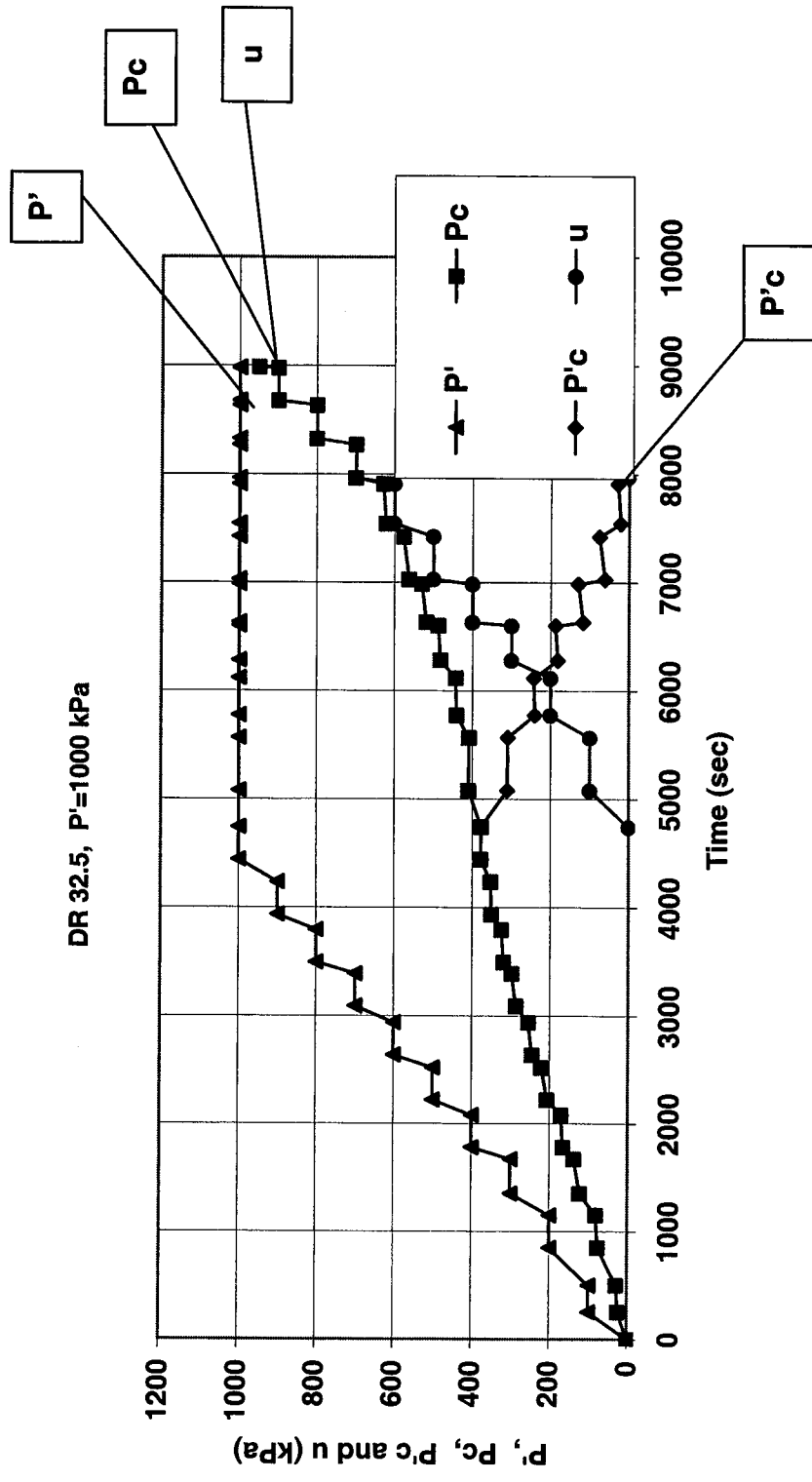


FIGURE 6.7 LOAD PATH OF THE EFFECTIVE BLADDER PRESSURE P' , THE TOTAL CONTACT PRESSURE P_c , THE EFFECTIVE CONTACT PRESSURE P'_c , AND THE PORE PRESSURE u FOR TEST T3

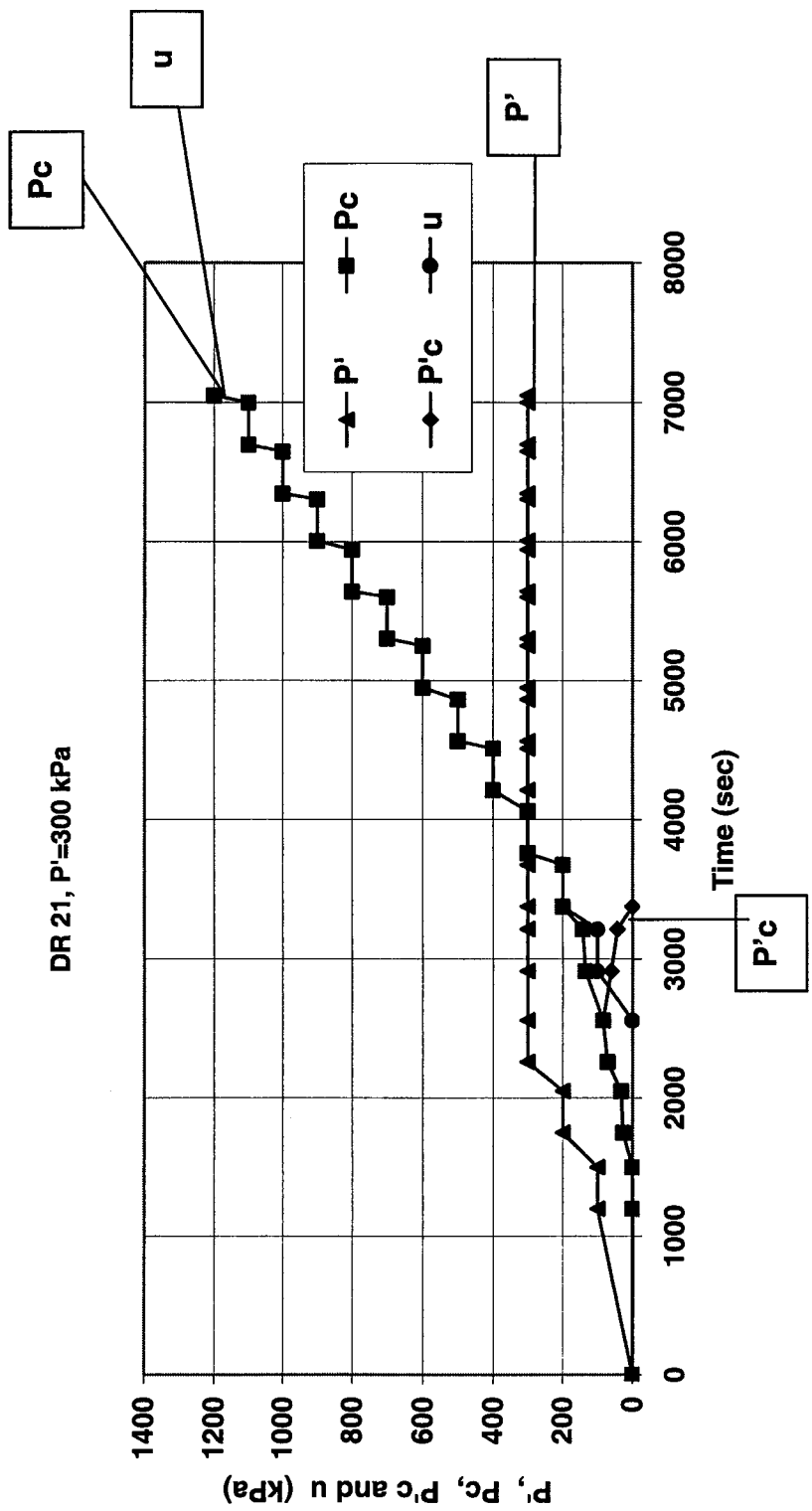


FIGURE 6.8 LOAD PATH OF THE EFFECTIVE BLADDER PRESSURE P' , THE TOTAL CONTACT PRESSURE P_c , THE EFFECTIVE CONTACT PRESSURE P'_c , AND THE PORE PRESSURE u FOR TEST T5

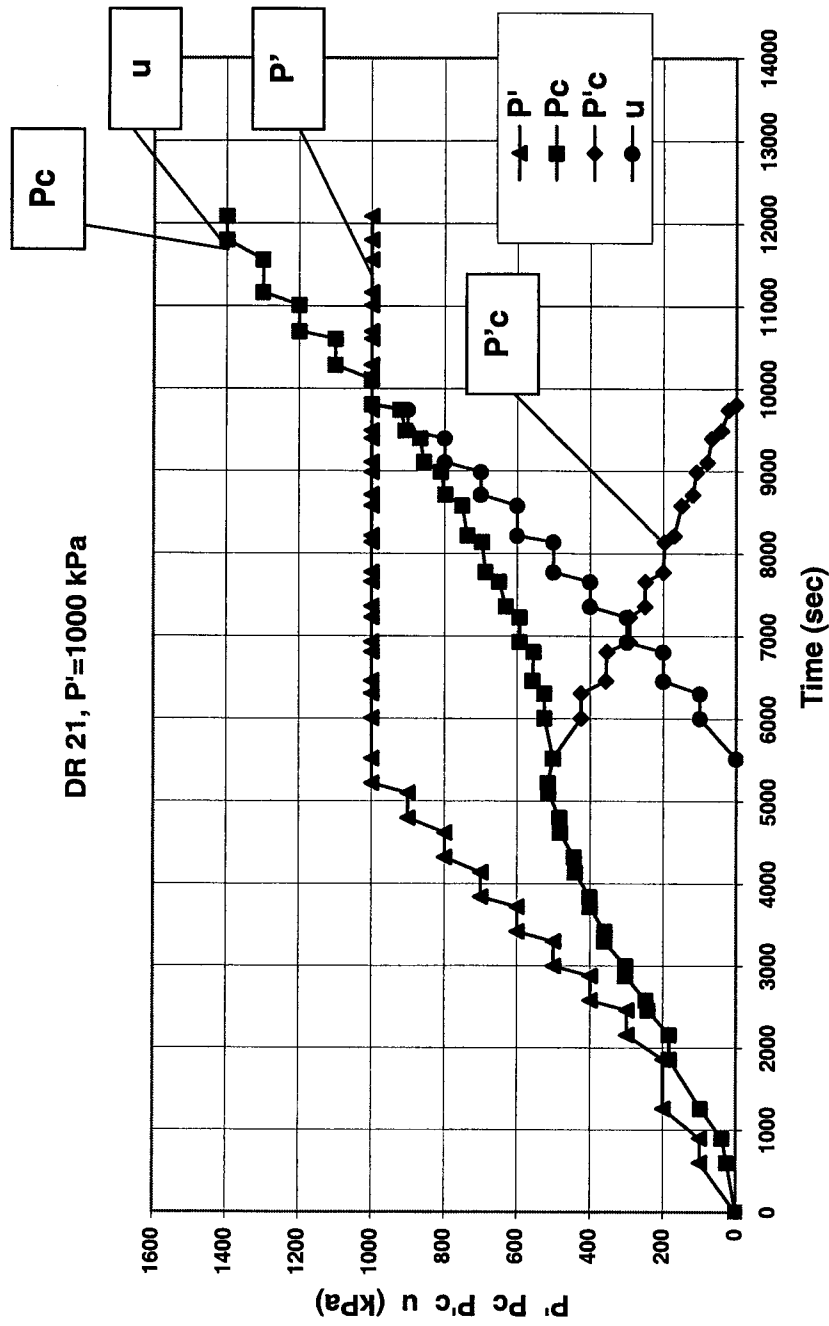


FIGURE 6.9 LOAD PATH OF THE EFFECTIVE BLADDER PRESSURE P' , THE TOTAL CONTACT PRESSURE P_c , THE EFFECTIVE CONTACT PRESSURE P'_c , AND THE PORE PRESSURE u FOR TEST T6

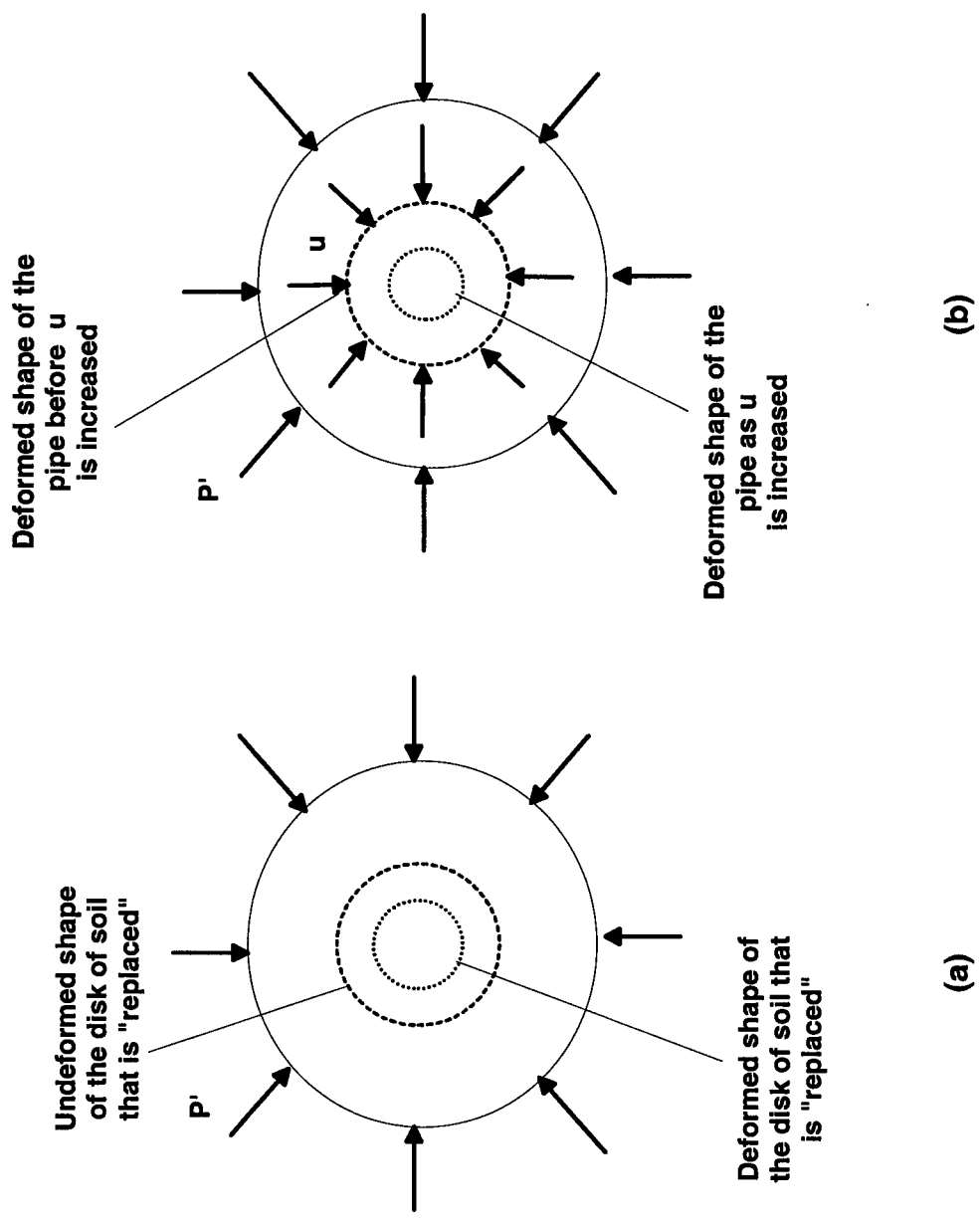


FIGURE 6.10 (a) DEFORMATION OF THE HYPOTHETICAL DISK OF SOIL UNDER THE LOAD P' , (b) DEFORMATION OF THE PIPE UNDER AN INCREASING PORE PRESSURE u

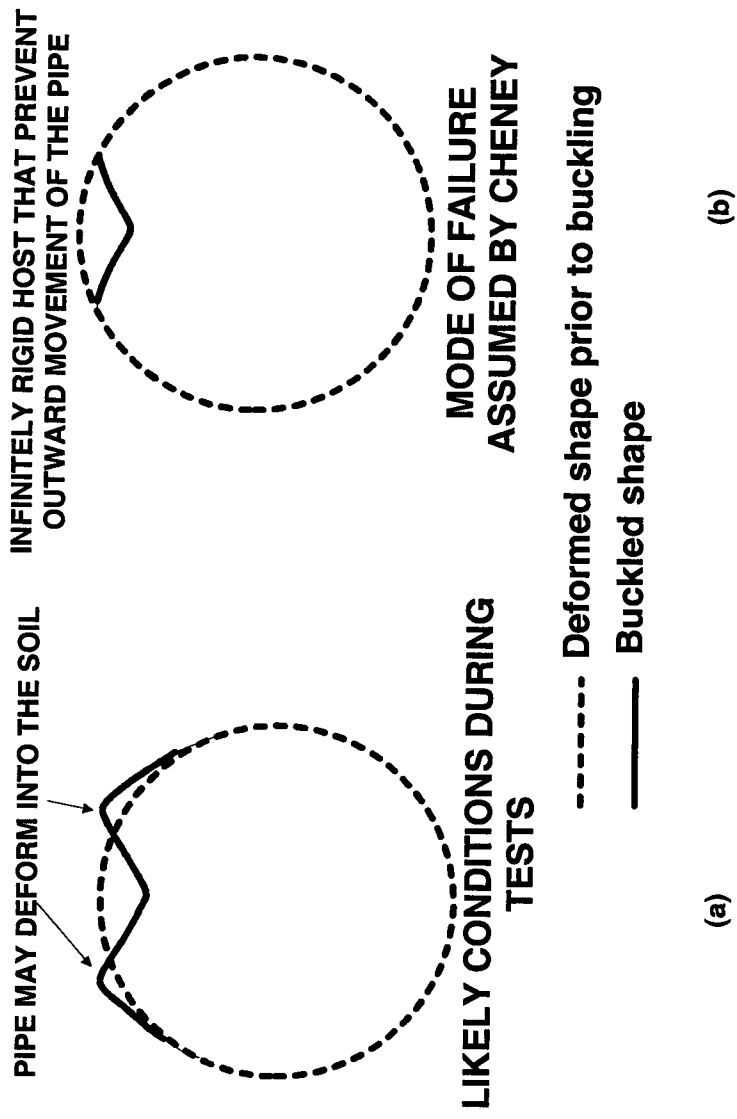


FIGURE 6.11 ILLUSTRATION SHOWING THE DIFFERENCE BETWEEN (a) THE ACTUAL CONDITIONS OF THE TESTS AND (b) THE ASSUMPTIONS MADE BY CHENEY

7. Conclusions

7.1 Introduction

Chapter 6 presented the analysis of the experimental data, in particular focusing on the effect of the pore pressures on the soil-structure interaction and thereby the pressures acting on the pipe during the tests. In general it was found that the fluid pressures decreased the ground loads that acted on the pipe leading to a single-wave buckling failure.

These results represent an experimental contribution for the problem of pipe buckling under ground and fluid loads. The measured buckling capacity of the pipes is directly applicable only for the specific conditions of the tests (constrained radial end conditions, $L/D = 3$ and uncompacted gravel backfill). However it is believed that the observation of the decrease of the effective contact pressure P'_c as the pore pressure u increased would control the soil-structure interaction and the buckling failure even if the end conditions mentioned above are different.

In this Chapter, Section 7.2 summarizes the major conclusions and Section 7.3 give recommendations for future research.

7.2 Summary of major conclusions

The major findings of this research are:

1. As a result of arching, only a fraction of the applied effective bladder pressure P' reached the pipe during the first stage of loading with zero

pore pressure. In tests T2, T3, and T6 it was evident that as P' increased during the first stage, the fraction of pressure that reached the pipe P'_c decreased. This indicated that the gravel became stiffer therefore transmitting a lower fraction of the loads to the pipe. On the other hand, the stiffer the pipe the more load it will attract as it can be appreciated by comparing the values of arching factor A' of 0.4 and 0.5 for tests T3 and T6, which were conducted with pipes DR 32.5 and DR 21 respectively.

2. As it was expected, the thicker pipes had a higher resistance against buckling. The fluid pressures at buckling for the DR 21 pipes were larger than for the DR 32.5 pipes as shown in Figure 5.14.
3. Only one dimple was observed during buckling failure of every test showing a single-wave mode of buckling. This indicated that buckling occurred mostly due to fluid pressures rather than effective stresses.
4. The sequence of images of buckling failure revealed that the formation of the dimple occurred relatively fast (between 4 and 8 seconds from the undeformed to the final shape of the dimple). Therefore little or no warning of buckling instability could be observed in the field.
5. For the specific boundary conditions implemented, the dimple formation during buckling failure occurred at different heights and radial orientations of the pipe. No correlation was found between the location of the dimple and the variables effective bladder pressure P' and DR of the pipe suggesting that the implemented boundary conditions may not strongly influence the results.

6. More abrupt curvatures of the dimples were observed for higher magnitudes of effective bladder pressure P' applied for a test. This occurred because higher pore pressures u were needed to produce buckling failure resulting in more abrupt curvatures of the dimples.
7. In every test, when the pore pressure u was increased during the second stage of testing, the effective contact pressure P'_c decreased to zero as a result of arching. The deformations induced on the pipe by the pore pressure u led to a redistribution of the effective stresses between the soil and the pipe that resulted in a decrease of the P'_c .
8. The presence of three distinct slopes in the deformation plots of tests T3 and T6 revealed the influence of the pore pressure u in the soil-structure interaction. When the pore pressures u was raised the slope of the deformation plot became less steep. Then, when the effective contact pressure P'_c decreased to zero and only fluid loads acted on the pipe the slope of the deformation plot became steeper.
9. As a result of the decrease of the effective contact pressure P'_c to zero only fluid loads acted on the pipe during buckling. This is consistent with the observed single-wave type of failure, which is related to buckling under high fluid pressures and low effective stresses.
10. The pore pressure u at buckling failure is proportional to the applied effective bladder pressure P' . This occurred because the magnitude of the effective contact pressure P'_c at the end of the first stage of the test is proportional to the effective bladder pressure P' . Therefore a higher pore

pressure u is needed to make P'_c decrease to zero and in every test buckling occurred when only fluid loads were acting on the pipe.

11. The capacity of the pipe beyond $P'_c = 0$ was compared with the solutions of Cheney (1971) and Glock (1977). The solution of Cheney overestimate the buckling the capacity in the rage of 21% to 67% while the predictions by Glock underestimate the capacity in the range of 48% to 66%. Further research is needed to investigate their applicability to the specific conditions of the tests.

7.3 Implications in the design of HDPE manholes

The conclusions obtained from the tests have implications in the design of manholes under ground and fluid loads provided that the load sequence (increase of effective stress P' followed by the pore pressure u) is similar. In the tests, the buckling failures occurred when only fluid pressures were acting on the pipes. Therefore keeping the effective contact pressures P'_c above zero would provide some stabilizing effect against buckling failure due to the presence of effective stresses in the soil located in the vicinity of the pipe. It is recommended that, under ground and fluid loads, a manhole should be designed to limit the radial deflections under the eventual pore pressures u that could act directly on it.

7.4 Recommendations for future research

1. It would be desirable to develop end seals for the pipes that do not constrain the radial deformations while effectively sealing at pressures higher than 1000 kPa. Being able to bond the seal material (rubber) with the polyethylene pipe may be a key aspect in the successful development of these seals. An efficient bonding of rubber materials to HDPE has not been developed to date.
2. If seals cannot be developed, tests with very long pipes (large L/D) should be performed in order to diminish the possible effect of the radial end constraints on the buckling capacity of the pipe. Testing larger pipe samples would require a larger test cell and bladder. Some difficulties associated with testing pipes with larger L/D ratios are the installation of instruments (reaching the center section of the pipe is more difficult) and the backfilling process complicates due to the increase in height from which the soil has to be dropped.
3. It would be interesting to observe the effects of a different load path on the soil-structure interaction of pipes under ground and fluid loads. Further testing could be made with increasing effective bladder pressure P' as the pore pressure u is increased rather than a constant P' while the pore pressure u is increased.
4. The influence of different soil-densities on the soil-structure interaction needs to be investigated. Therefore experiments with backfills at different compaction levels should be performed. It could be speculated that a

stiffer backfill might result in lower values of $P'c$ at the end of the first stage (because a lesser fraction of the bladder pressure reaches the pipe) possibly leading to lower pore pressures u at buckling. Only test data would provide reliable observations of the effect of using a stiffer soil.

LIST OF REFERENCES

Allgood, J.R., and Ciani, J.B., 1968, "*The Influence of Soil Modulus on the Behavior of Cylinders in Sand.*", Highway Res. Rec. No. 249, pp. 1-13.

ASTM C127-88 *Standard Test Method for Specific Gravity and Absorption of Coarse Aggregate*, American Society for Testing and Materials, West Conshohocken, PA.

ASTM D422-63 *Standard Test Method for Particle-Size Analysis of Soils*, American Society for Testing and Materials, West Conshohocken, PA.

ASTM D2487-93 *Standard Classification of Soils for Engineering Purposes (Unified Soil Classification System)*, American Society for Testing and Materials, West Conshohocken, PA.

ASTM D3350-96 *Standard Specification for Polyethylene Plastics Pipe and Fittings Materials*, American Society for Testing and Materials, West Conshohocken, PA.

ASTM D4253-93 *Standard Test Methods for Maximum Index Density and Unit Weight of Soils Using a Vibratory Table*, American Society for Testing and Materials, West Conshohocken, PA.

ASTM D4254-91 *Minimum Index Density and Unit Weight of Soils and Calculation of Relative Density*, American Society for Testing and Materials, West Conshohocken, PA.

ASTM F714-97 *Standard Specification for Polyethylene (PE) Plastic Pipe (SDR-PR) Based on Outside Diameter*, American Society for Testing and Materials, West Conshohocken, PA.

ASTM F1759-97 *Standard Practice for Design of High-Density Polyethylene (HDPE) Manholes for Subsurface Applications*, American Society for Testing and Materials, West Conshohocken, PA.

Boot, J.C., and Welch, A.J., 1996, "*Creep Buckling of Thin-walled Polymeric Pipe Linings Subject to External Groundwater Pressure.*", *Thin-Walled Structures* 24, pp. 191-210.

Cheney, J. A., 1971, "*Pressure Buckling of Ring Encased in a Cavity.*", J. Engrg. Mech., ASCE, 97(2), pp. 333-342.

Cheney, J. A., 1976, "*Buckling of Thin-walled Cylindrical Shells in Soil.*", Suppl. Rep. 204, Transp. and Road Res. Lab., Dept. of the Environment, Crawthorne.

Crabb, G.I., and Carder, D.R., 1985, "*Loading Tests on Buried Flexible Pipes to Validate a New Design Model.*", Res. Rep. 28, Transp. and Road Res. Lab., Dept. of the Environment, Crawthorne.

Falter, B., 1980, "*Grenzlasten Von Einseitig elastisch Gebetteten Kreiszyklindrischen Konstruktionen.*" ("Critical Loads for Circular Cylindrical Structural with One-sided Elastic Support"), Bauingenieur 55(10), pp. 381-390.

Forrestal, M. J., and Herrmann, G., 1965, "*Buckling of a Long Cylindrical Shell Surrounded by an Elastic Medium.*", Int. J. Solids Struct. 1, pp. 297-310.

Gartung, E., Pruhs, H., and Hoch, A., 1989, "*Design of Vertical Shafts in Landfills.*", Proceedings Sardinia 89, Second International Landfill Symposium, C.XI-1 to C.XI-7.

Gartung, E., Pruhs, H., and Nowack, F., 1993, "*Measurements on Vertical Shafts in Landfills.*", Proceedings Sardinia 89, Second International Landfill Symposium, C.XI-1 to C.XI-7.

Glock, D., 1977, "*Post-Critical Behavior of a Rigidly Encased Circular Pipe Subject to External Water Pressure and Temperature Rise.*", Der Stahlbau, 46(7), pp. 212-217, (in German).

Gumbel, J.E., 1983, "*Analysis and Design of Buried Flexible Pipes.*", Thesis presented to the University of Surrey, Surrey, United Kingdom, in partial fulfillment of the requirements for the degree of Doctor of Philosophy.

Hain, H., 1970, "*Stabilitat Von Im Boden Eingebetteten Tunnelrorhen Mit Kreisformigen Querschnitt.*", ("Stability of Soil-surrounded Tunnel Rings of Circular Cross-section"), Strasse Brucke Tunnel 22(6), pp. 154-159; 22(8), pp. 206-208.

Hall, D., and Zhu, M., 2000, "*Recent Findings & Ongoing Liner Buckling Research at the Trenchless Technology Center.*", Proc. North American NO-DIG 2000 Conference, Anaheim, California, April 9-12, 2000, pp. 77-84.

Hoeg, K., 1968, "*Stresses Against Underground Cylinders.*", J. of Soil Mech., ASCE, 94(4), pp. 833-858.

Jenkins, C.F., and Kroll, A.E., 1981, "*External Hydrostatic Loading of Polyethylene Pipe.*", Proc. International Conf. Underground Plastic Pipe, New Orleans, Louisiana, March 30-April 1, 1981, pp. 527–541.

Kloppel, K., and Glock, D., 1970, "*Theoretische Und Experimentelle Untersuchungen zu den Traglastproblem Biegeweichen, in die erde Eingebetter Rohre.*", Publication No. 10, Inst. fur Statik und Stahlbau der Technischen Hochschule Darmstadt, Germany.

Levy, M., 1884, "*Memoire sur un Noveau cas Integrale du Probleme de L'elastique et l'une de ses Applications.*", Journal de Math, Pure et Appl., Vol. 7, No. 3, p.5.

Luscher, U., 1966, "*Buckling of Soil-Surrounded Tubes.*", J. Soil Mech. Found., ASCE, 92(6), pp. 211-228.

Meyerhof, G.G., and Baikie, L.D., 1963, "*Strength of Steel Culvert Sheets Bearing Against Compacted Backfill.*", Highw. Res. Rec. No. 30, Highway Res. Board, Washington, D.C., pp. 1-14.

Moore, I.D., 1989, "*Elastic Buckling of Buried Flexible Tubes – A Review of Theory and Experiment.*", J. of Geotechnical Eng., ASCE, Vol. 115(3), pp. 340-358.

Moore, I.D., "WANFE", University of Western Ontario, 1996.

Moore, I.D., 1998, "*Tests for Pipe Liner Stability: What We Can and Cannot Learn.*", Proc. North American NO-DIG '98 Conference, Albuquerque, New Mexico, April 5-8, 1998, pp. 444-457.

Moore, I.D., Haggag, A., and Selig, E.T., 1994, "*Buckling Strength of Flexible Cylinders with Non-uniform Elastic Support.*", Int. Journ. of Solid Structures, Vol. 31(22), pp. 3041-3058.

Selig, E.T., 1990, "*Soil Properties for Plastic Pipe Installations.*", Buried Plastic Pipe Technology, ASTM STP 1093, pp. 141-158.

Sonntag, G., 1966a, "*Die Stabilität Dünnwandiger Rohre im Kohäsionslosen Kontinuum.*", ("The Stability of Thin-walled Tubes in Cohesion-free Continuum"), *Felsmechanik und Ingenieurgeologie* 4(3), pp. 242-267.

Sonntag, G., 1966b, "*Stabilität des Elastisch Gebetteten Rohrs Unter Aussendruck.*", ("Stability of Elastically Embedded Pipe Under External Pressure"), *Forsch. Ing.Wes.* 32(6), pp. 89 - 93.

Szpak, E., 1981, "*Polyethylene Pipe Subjected to External Pressure.*", *Proc. International Conf. Underground Plastic Pipe*, New Orleans, Louisiana, March 30-April 1, 1981, pp. 373–384.

Zhang, C., and Moore, I.D., 1997a, "*Nonlinear Mechanical Response of High Density Polyethylene. Part I: Experimental Investigation and Model Evaluation.*", *Polymer Eng. and Science*, Vol. 37 (2), pp. 404-413.

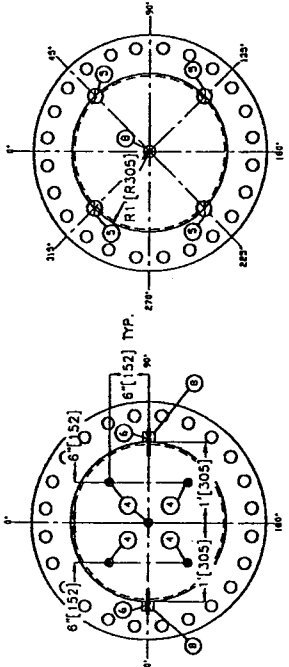
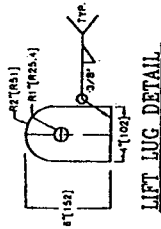
Zhang, C., and Moore, I.D., 1997b, "*Nonlinear Mechanical Response of High Density Polyethylene. Part II: Uniaxial Constitutive Modeling.*", *Polymer Eng. and Science*, Vol. 37 (2), pp. 414-420.

Appendix A

C1
 WPT WP-SWAW-13
 REV. 1

A BILL OF MATERIALS

ITEM QTY	SIZE	UNIT	DESCRIPTION	MAT. REF. NO.	QTY
1	PIPE 24 (10)	SEC STD X 3-3	24 (10) LG	SA-102-B	102052
2	FLANGES 24 (10)	5057	RF BD	SA-102-B	102072
3	BOLTS 24 (10)	5057	RF BD	SA-102-B	102110
4	WASHERS 24 (10)	5057	RF BD	SA-102-B	102110
5	1/4" DIA. LOCK WASHERS 24 (10)	5057	RF BD	SA-102-B	102110
6	1/2" DIA. LOCK WASHERS 24 (10)	5057	RF BD	SA-102-B	102110
7	1/2" DIA. LOCK WASHERS 24 (10)	5057	RF BD	SA-102-B	102110
8	1/2" DIA. LOCK WASHERS 24 (10)	5057	RF BD	SA-102-B	102110
9	1/2" DIA. LOCK WASHERS 24 (10)	5057	RF BD	SA-102-B	102110
10	1/2" DIA. LOCK WASHERS 24 (10)	5057	RF BD	SA-102-B	102110
11	1/2" DIA. LOCK WASHERS 24 (10)	5057	RF BD	SA-102-B	102110
12	1/2" DIA. LOCK WASHERS 24 (10)	5057	RF BD	SA-102-B	102110
13	1/2" DIA. LOCK WASHERS 24 (10)	5057	RF BD	SA-102-B	102110
14	1/2" DIA. LOCK WASHERS 24 (10)	5057	RF BD	SA-102-B	102110
15	1/2" DIA. LOCK WASHERS 24 (10)	5057	RF BD	SA-102-B	102110
16	1/2" DIA. LOCK WASHERS 24 (10)	5057	RF BD	SA-102-B	102110
17	1/2" DIA. LOCK WASHERS 24 (10)	5057	RF BD	SA-102-B	102110
18	1/2" DIA. LOCK WASHERS 24 (10)	5057	RF BD	SA-102-B	102110
19	1/2" DIA. LOCK WASHERS 24 (10)	5057	RF BD	SA-102-B	102110
20	1/2" DIA. LOCK WASHERS 24 (10)	5057	RF BD	SA-102-B	102110
21	1/2" DIA. LOCK WASHERS 24 (10)	5057	RF BD	SA-102-B	102110
22	1/2" DIA. LOCK WASHERS 24 (10)	5057	RF BD	SA-102-B	102110
23	1/2" DIA. LOCK WASHERS 24 (10)	5057	RF BD	SA-102-B	102110
24	1/2" DIA. LOCK WASHERS 24 (10)	5057	RF BD	SA-102-B	102110
25	1/2" DIA. LOCK WASHERS 24 (10)	5057	RF BD	SA-102-B	102110
26	1/2" DIA. LOCK WASHERS 24 (10)	5057	RF BD	SA-102-B	102110
27	1/2" DIA. LOCK WASHERS 24 (10)	5057	RF BD	SA-102-B	102110
28	1/2" DIA. LOCK WASHERS 24 (10)	5057	RF BD	SA-102-B	102110
29	1/2" DIA. LOCK WASHERS 24 (10)	5057	RF BD	SA-102-B	102110
30	1/2" DIA. LOCK WASHERS 24 (10)	5057	RF BD	SA-102-B	102110
31	1/2" DIA. LOCK WASHERS 24 (10)	5057	RF BD	SA-102-B	102110
32	1/2" DIA. LOCK WASHERS 24 (10)	5057	RF BD	SA-102-B	102110
33	1/2" DIA. LOCK WASHERS 24 (10)	5057	RF BD	SA-102-B	102110
34	1/2" DIA. LOCK WASHERS 24 (10)	5057	RF BD	SA-102-B	102110
35	1/2" DIA. LOCK WASHERS 24 (10)	5057	RF BD	SA-102-B	102110
36	1/2" DIA. LOCK WASHERS 24 (10)	5057	RF BD	SA-102-B	102110
37	1/2" DIA. LOCK WASHERS 24 (10)	5057	RF BD	SA-102-B	102110
38	1/2" DIA. LOCK WASHERS 24 (10)	5057	RF BD	SA-102-B	102110
39	1/2" DIA. LOCK WASHERS 24 (10)	5057	RF BD	SA-102-B	102110
40	1/2" DIA. LOCK WASHERS 24 (10)	5057	RF BD	SA-102-B	102110
41	1/2" DIA. LOCK WASHERS 24 (10)	5057	RF BD	SA-102-B	102110
42	1/2" DIA. LOCK WASHERS 24 (10)	5057	RF BD	SA-102-B	102110
43	1/2" DIA. LOCK WASHERS 24 (10)	5057	RF BD	SA-102-B	102110
44	1/2" DIA. LOCK WASHERS 24 (10)	5057	RF BD	SA-102-B	102110
45	1/2" DIA. LOCK WASHERS 24 (10)	5057	RF BD	SA-102-B	102110
46	1/2" DIA. LOCK WASHERS 24 (10)	5057	RF BD	SA-102-B	102110
47	1/2" DIA. LOCK WASHERS 24 (10)	5057	RF BD	SA-102-B	102110
48	1/2" DIA. LOCK WASHERS 24 (10)	5057	RF BD	SA-102-B	102110
49	1/2" DIA. LOCK WASHERS 24 (10)	5057	RF BD	SA-102-B	102110
50	1/2" DIA. LOCK WASHERS 24 (10)	5057	RF BD	SA-102-B	102110
51	1/2" DIA. LOCK WASHERS 24 (10)	5057	RF BD	SA-102-B	102110
52	1/2" DIA. LOCK WASHERS 24 (10)	5057	RF BD	SA-102-B	102110
53	1/2" DIA. LOCK WASHERS 24 (10)	5057	RF BD	SA-102-B	102110
54	1/2" DIA. LOCK WASHERS 24 (10)	5057	RF BD	SA-102-B	102110
55	1/2" DIA. LOCK WASHERS 24 (10)	5057	RF BD	SA-102-B	102110
56	1/2" DIA. LOCK WASHERS 24 (10)	5057	RF BD	SA-102-B	102110
57	1/2" DIA. LOCK WASHERS 24 (10)	5057	RF BD	SA-102-B	102110
58	1/2" DIA. LOCK WASHERS 24 (10)	5057	RF BD	SA-102-B	102110
59	1/2" DIA. LOCK WASHERS 24 (10)	5057	RF BD	SA-102-B	102110
60	1/2" DIA. LOCK WASHERS 24 (10)	5057	RF BD	SA-102-B	102110
61	1/2" DIA. LOCK WASHERS 24 (10)	5057	RF BD	SA-102-B	102110
62	1/2" DIA. LOCK WASHERS 24 (10)	5057	RF BD	SA-102-B	102110
63	1/2" DIA. LOCK WASHERS 24 (10)	5057	RF BD	SA-102-B	102110
64	1/2" DIA. LOCK WASHERS 24 (10)	5057	RF BD	SA-102-B	102110
65	1/2" DIA. LOCK WASHERS 24 (10)	5057	RF BD	SA-102-B	102110
66	1/2" DIA. LOCK WASHERS 24 (10)	5057	RF BD	SA-102-B	102110
67	1/2" DIA. LOCK WASHERS 24 (10)	5057	RF BD	SA-102-B	102110
68	1/2" DIA. LOCK WASHERS 24 (10)	5057	RF BD	SA-102-B	102110
69	1/2" DIA. LOCK WASHERS 24 (10)	5057	RF BD	SA-102-B	102110
70	1/2" DIA. LOCK WASHERS 24 (10)	5057	RF BD	SA-102-B	102110
71	1/2" DIA. LOCK WASHERS 24 (10)	5057	RF BD	SA-102-B	102110
72	1/2" DIA. LOCK WASHERS 24 (10)	5057	RF BD	SA-102-B	102110
73	1/2" DIA. LOCK WASHERS 24 (10)	5057	RF BD	SA-102-B	102110
74	1/2" DIA. LOCK WASHERS 24 (10)	5057	RF BD	SA-102-B	102110
75	1/2" DIA. LOCK WASHERS 24 (10)	5057	RF BD	SA-102-B	102110
76	1/2" DIA. LOCK WASHERS 24 (10)	5057	RF BD	SA-102-B	102110
77	1/2" DIA. LOCK WASHERS 24 (10)	5057	RF BD	SA-102-B	102110
78	1/2" DIA. LOCK WASHERS 24 (10)	5057	RF BD	SA-102-B	102110
79	1/2" DIA. LOCK WASHERS 24 (10)	5057	RF BD	SA-102-B	102110
80	1/2" DIA. LOCK WASHERS 24 (10)	5057	RF BD	SA-102-B	102110
81	1/2" DIA. LOCK WASHERS 24 (10)	5057	RF BD	SA-102-B	102110
82	1/2" DIA. LOCK WASHERS 24 (10)	5057	RF BD	SA-102-B	102110
83	1/2" DIA. LOCK WASHERS 24 (10)	5057	RF BD	SA-102-B	102110
84	1/2" DIA. LOCK WASHERS 24 (10)	5057	RF BD	SA-102-B	102110
85	1/2" DIA. LOCK WASHERS 24 (10)	5057	RF BD	SA-102-B	102110
86	1/2" DIA. LOCK WASHERS 24 (10)	5057	RF BD	SA-102-B	102110
87	1/2" DIA. LOCK WASHERS 24 (10)	5057	RF BD	SA-102-B	102110
88	1/2" DIA. LOCK WASHERS 24 (10)	5057	RF BD	SA-102-B	102110
89	1/2" DIA. LOCK WASHERS 24 (10)	5057	RF BD	SA-102-B	102110
90	1/2" DIA. LOCK WASHERS 24 (10)	5057	RF BD	SA-102-B	102110
91	1/2" DIA. LOCK WASHERS 24 (10)	5057	RF BD	SA-102-B	102110
92	1/2" DIA. LOCK WASHERS 24 (10)	5057	RF BD	SA-102-B	102110
93	1/2" DIA. LOCK WASHERS 24 (10)	5057	RF BD	SA-102-B	102110
94	1/2" DIA. LOCK WASHERS 24 (10)	5057	RF BD	SA-102-B	102110
95	1/2" DIA. LOCK WASHERS 24 (10)	5057	RF BD	SA-102-B	102110
96	1/2" DIA. LOCK WASHERS 24 (10)	5057	RF BD	SA-102-B	102110
97	1/2" DIA. LOCK WASHERS 24 (10)	5057	RF BD	SA-102-B	102110
98	1/2" DIA. LOCK WASHERS 24 (10)	5057	RF BD	SA-102-B	102110
99	1/2" DIA. LOCK WASHERS 24 (10)	5057	RF BD	SA-102-B	102110
100	1/2" DIA. LOCK WASHERS 24 (10)	5057	RF BD	SA-102-B	102110



ORIENTATION VIEW "A-A"

ORIENTATION VIEW "B-B"

ELEVATION VIEW

AS-BUILT
 DATE: 12/14/09
 SIGN: [Signature]

AS BUILT FOR S/N 7489Y

ALBERTA CUSTOM PIPE BENDING & MFG. LTD
 PHONE: (403) 448-4824 FAX: (403) 448-4823
 72 AVENUE, CALGARY, ALBERTA T2C 1P1 CANADA

U O F A

CUSTOMER	ALBERTA CUSTOM PIPE BENDING & MFG. LTD
ORDER NO.	2000-72-B
DATE	12/14/09
REV	2
DESCRIPTION	24 NPS TEST CELLS TYPE 2
QTY	1
UNIT	EA

DESIGN DATA

DESIGN PRESSURE	450 PSI (3103 kPa) @ 180°F (82°C) A
M.O.M.T.	2,207 (L-3/FC) @ 450 PSI (3103 kPa)
X-RAY	NONE STRESS RELIEF: NONE
HYDRO TEST PRESSURE	675 PSI (4655 kPa) WEIGHT EMPTY: 2804 LBS (1273 kg)
WEIGHT FULL OF WATER	3345 LBS (1513 kg) VOLUME: 8.7 FT ³ (0.27 m ³)
ALL BOLT HOLES TO STRADDLE CENTRE LINES UNLESS OTHERWISE NOTED.	

- ### NOTES
- CHART RECORD HYDROTEST AT 675 PSI (4655 kPa) FOR MIN 1 HOUR.
 - INSIDE CORNERS OF 24\"/>